Title

Advancing Dark Energy Studies with DESI: Innovations in Instrumentation and Lyman-alpha Forest Cosmology

Author

Bault, Abigail

Publication Date

2024

UNIVERSITY OF CALIFORNIA,
IRVINE

Advancing Dark Energy Studies with DESI: Innovations in Instrumentation and Lyman-alpha Forest Cosmology

DISSERTATION

submitted in partial satisfaction of the requirements
for the degree of

DOCTOR OF PHILOSOPHY

in Physics

by

Abigail Rose Bault

Dissertation Committee:
Chancellor's Professor David Kirkby, Chair
Assistant Professor Steph Sallum
Professor Manoj Kaplinghat

2024

DEDICATION

To my mom, for instilling in me a love of learning and for showing me that anything can be accomplished with a little effort and determination.

TABLE OF CONTENTS

LIST OF FIGURES

Page

LIST OF TABLES

ACKNOWLEDGMENTS

Firstly, thank you to my family for supporting me and helping me through the incredibly stressful times during the past 6 years. Especially thank you to my mom, who put up with (sometimes daily) phone calls just so I could talk through my thoughts when I was stuck on a problem. Your support has been invaluable throughout this process.

To my friends back in Michigan, thank you for always making time to see me when I'm in town for a visit. To Ashley, for always being ready to go to a last minute hockey game or have a relaxing night in building a puzzle. And to Dan (and Erin) for allowing me to invade your home for an evening or two to catch up on all our lives.

To the friends I've made in Irvine, thank you for filling my time here with wonderful memories. I know our friendships will transcend grad school and UCI. To Astrid, Jessica, and Genevieve, for pulling me into your friend group and guiding me through my first year as a graduate student. Also to Astrid, for always being ready to play Zelda, even though we were on our own switches. To Ceci, for showing me that there might be a crazier cat lady than myself and for all of our hangouts both past and future. To Matt and Dylan, for the shenanigans during group meeting days that made being in the office all day bearable.

Finally, thank you to David for being such an incredible advisor these past 6 years. Thank you for giving me the freedom to explore my interests while also guiding me toward projects that you knew would fit my interests. Your support and kindness while dealing with my endless questions (and still somehow always allowing me to find the answer for myself!) really built up my confidence both as a physicist and as a researcher.

I would like to thank the DOE for funding this work from grant DE-SC0009920.

Chapter 4 is the version of the article before peer review or editing, as submitted by an author to the Journal of Cosmology and Astroparticle Physics (JCAP) in [11]. IOP Publishing Ltd is not responsible for any errors or omissions in this version of the manuscript or any version derived from it. The Version of Record is available online at JCAP. The coauthors listed in this publication are David Kirkby, Julien Guy, Allyson Brodzeller, and other DESI Collaboration members. David Kirkby directed and supervised research which forms the basis for the dissertation.

VITA

Abigail Rose Bault

EDUCATION

Doctor of Philosophy in Physics **2024**
University of California, Irvine *Irvine, CA*

Master of Science in Physics **2020**
University of California, Irvine *Irvine, CA*

Bachelor of Science in Physics **2018**
Wayne State University *Detroit, MI*

RESEARCH EXPERIENCE

Graduate Research Assistant **2019–2024**
University of California, Irvine *Irvine, California*

DOE Office of Science Graduate Student Research Fellow **2022**
Lawrence Berkeley National Laboratory *Berkeley, CA*

SURF Student **Summer 2017**
University of Pittsburgh *Pittsburgh, PA*

TEACHING EXPERIENCE

Teaching Assistant **2018–2019**
University of California, Irvine *Irvine, CA*

REFEREED JOURNAL PUBLICATIONS

Impact of Systematic Redshift Errors on the Cross-correlation of the Lyman-α Forest with Quasars at Small Scales Using DESI Early Data Journal of Cosmology and Astrophysics	**2024**
DESI 2024 III: Baryon Acoustic Oscillations from Galaxies and Quasars Journal of Cosmology and Astrophysics	**2024**
DESI 2024 IV: Baryon Acoustic Oscillations from the Lyman Alpha Forest Journal of Cosmology and Astrophysics	**2024**
DESI 2024 VI: Cosmological Constraints from the Measurements of Baryon Acoustic Oscillations Journal of Cosmology and Astrophysics	**2024**
Broad Absorption Line Quasars in the Dark Energy Spectroscopic Instrument Early Data Release Monthly Notices of the Royal Astronomical Society	**2023**
3D Correlations in the Lyman-alpha Forest from Early DESI Data Journal of Cosmology and Astrophysics	**2023**
Synthetic Spectra for Lyman-α Forest Analysis in the Dark Energy Spectroscopic Instrument Journal of Cosmology and Astrophysics	**2023**
Performance of the Quasar Spectral Templates for the Dark Energy Spectroscopic Instrument Astronomical Journal	**2023**
The Early Data Release of the Dark Energy Spectroscopic Instrument Astronomical Journal	**2023**
Validation of the Scientific Program for the Dark Energy Spectroscopic Instrument Astronomical Journal	**2023**
Improved Tomographic Binning of 3x2pt Lens Samples: Neural Network Classifiers and Optimal Bin Assignments Astrophysical Journal	**2023**

Overview of the Instrumentation for the Dark Energy Spectroscopic Instrument **2022**
Astronomical Journal

The LSST-DESC 3x2pt Tomography Optimization Challenge **2021**
Open Journal of Astrophysics

ABSTRACT OF THE DISSERTATION

Advancing Dark Energy Studies with DESI: Innovations in Instrumentation and Lyman-alpha Forest Cosmology

By

Abigail Rose Bault

Doctor of Philosophy in Physics

University of California, Irvine, 2024

Chancellor's Professor David Kirkby, Chair

One of the most compelling challenges in cosmology is understanding the nature of dark energy and how it affects the expansion of the universe. The Dark Energy Spectroscopic Instrument (DESI) is attempting to improve our understanding by using baryon acoustic oscillations (BAO) to study the expansion history of the universe. In Chapter 1 I provide a brief introduction to the expansion history of the universe as well as the probes of large scale structure. In Chapter 2 I provide an in depth description of the DESI instrument, focal plane, and main survey. This thesis consists of two main projects focused on improving the DESI focal plane and analyses using quasars and the Lyman-α forest.

The first project, discussed in Chapter 3, focuses on improvements to the DESI focal plane. The focal plane uses 5,000 robotic fiber positioners, approximately 12% of which are unusable due to poor performance. Roughly half display linear phi behavior. This number is increasing at a rate of approximately 1 new positioner per week. If enough positioners become unusable, the main survey (and potential future DESI-ext and DESI-2 surveys) may not be able to finish on time. Many different mitigation strategies were studied, but I found that the best performance came by increasing the motor speed and by applying a scale factor correction. Each move also follows a new move strategy consisting of a back and forth move. Move tests

were performed on the DESI focal plane in 2023 and in March and July of 2024. The July tests showed that 228 positioners could be recovered and returned to night operations. This is roughly 72% of the linear phi positioners.

The second project, discussed in Chapter 4, focuses on how quasar redshift errors impact the correlation functions used in the Lyman-α forest analyses. We measure systematic quasar redshift errors as an offset in the Lyman-α forest-quasar cross-correlation. Using data from the DESI Early Data Release (EDR) I found evidence for a redshift-dependent bias causing quasar redshifts to be underestimated with increasing redshift. This bias stems from the improper modeling of the Lyman-α optical depth in the high redshift quasar templates used for redshift estimation. New templates were derived for the year 1 quasar sample. The analysis was repeated and I found that the bias resolved and is now consistent with zero. The new templates were used to provide redshifts for the DESI Year 1 quasar sample and will be used for future data releases as well.

Chapter 1

Introduction

1.1 The Universe is Expanding

1.1.1 The Standard Model of Cosmology

We have known for about a century that the universe is expanding. Hubble first discovered this in 1929 when he used Cepheid variable stars to measure the distances to roughly 20 galaxies (see fig 1.1) [65]. This is contradictory to Einstein's theory of general relativity, published in 1915, in which he assumed a static universe and utilized a cosmological constant, Λ to balance his field equations:

$$G_{\mu\nu} + \Lambda g_{\mu\nu} = \frac{8\pi G}{c^4} T_{\mu\nu}. \tag{1.1}$$

After Hubble's discovery of the expanding universe, support for Einstein's cosmological constant dwindled. However, in the late 1990's observations of supernovae provided evidence for both an expanding universe and a cosmological constant [83, 90]. These results were the first to confirm that the expansion of the universe is indeed accelerating and that the simplest dark energy is model can explain the acceleration. This established a new standard model of cosmology, called ΛCDM.

In this ΛCDM model, the universe is flat, is composed of approximately 70% dark energy (Λ), 25% cold dark matter (CDM), 5% normal matter, or baryonic matter, and follows the laws of Einstein's general relativity under the Friedmann-Lemaître-Robertson-Walker (FLRW) metric. The ΛCDM model has been studied in depth for many years, with high precision measurements arising from studies of baryon acoustic oscillations (BAO) with galaxies and high redshift quasars [4, 5, 43] and from studies of temperature anisotropies in the CMB [62, 85]. In fact, Planck 2018 [85] results give $H_0 = 67.36 \pm 0.54$ km s^{-1} Mpc^{-1}, $\Omega_m = 0.315 \pm 0.007$, and $\Omega_\Lambda = 0.684 \pm 0.007$. This is consistent with the recent results from DESI ($H_0 = 68.52 \pm 0.62$ km s^{-1} Mpc^{-1} and $\Omega_m = 0.295 \pm 0.015$) [33] though there is still a $> 3\sigma$ tension with the supernova measurements. Though studies are ongoing, many questions still remain as to the exact nature of dark energy and the evolution of large scale structure in the universe.

1.1.2 Measuring the Expansion of the Universe

A consequence of an expanding universe means that distances between objects in the early universe were smaller than they are today. We describe this expansion by introducing a dimensionless scale factor, $a(t)$, such that at earlier times it was smaller than it is today and the present day value $a(t_0) = 1$.

As the universe expands, light emitted from objects stretches proportionally to the scale factor. This means that the observed wavelength is larger than the emitted wavelength of the light. We describe this stretching as the redshift, z, which is defined as

$$1 + z \equiv \frac{\lambda_{\text{obs}}}{\lambda_{\text{emit}}} = \frac{a_{\text{obs}}}{a_{\text{emit}}} = \frac{a(t_0)}{a(t)} = \frac{1}{a(t)}. \tag{1.2}$$

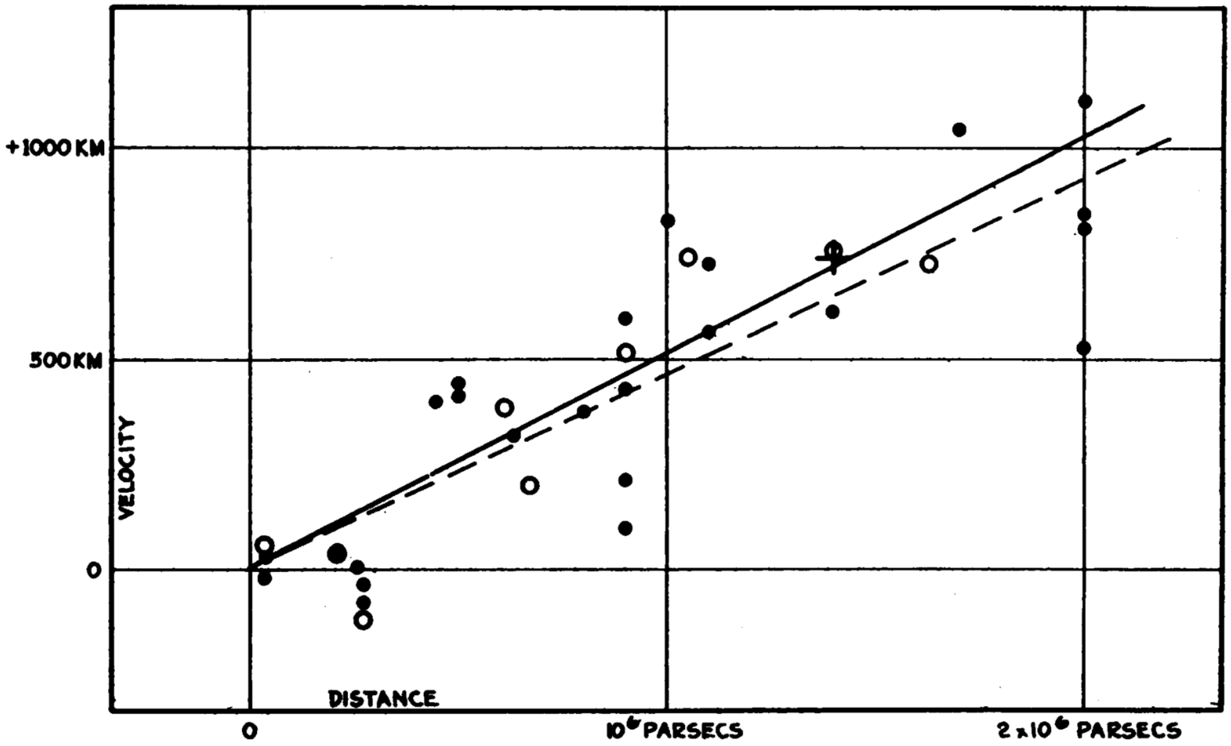

Figure 1.1: A figure from Hubble's 1929 paper [65] showing the radial velocities (Y-axis) in km (should be in km s^{-1}) vs the measured distance (X-axis) in parsecs for the extragalactic nebulae studied by Hubble. The solid points and line represent the solution using individual nebulae, while the open points and dashed line combine nebulae into groups. The cross is the mean velocity and distance corresponding to the nebulae whose distances could not be estimated individually.

The dependence on the scale factor with time varies according to the energy density in the universe. To understand this relationship, we define the Hubble rate, $H(t)$, as

$$H(t) \equiv \frac{1}{a}\frac{da}{dt}. \tag{1.3}$$

The value of the Hubble rate today is known as Hubble's constant, with $H_0 \equiv H(t_0)$. The Hubble constant is parameterized by a dimensionless quantity h such that, $H_0 \equiv 100h$ km s^{-1} Mpc^{-1}. When Hubble measured distances to the extragalactic nebulae shown in figure 1.1 he used a linear relation, now known as Hubble's law, relating the redshift to the distance:

$$z = \frac{H_0}{c}r, \tag{1.4}$$

where H_0 is the Hubble constant, c is the speed of light, and r is the distance to the nebulae. To obtain the velocities from figure 1.1, we assume the redshifts are Doppler shifts. Then, Hubble's law is $v = H_0 r$, where v is the radial velocity of the nebula.

Attempts to accurately measure the Hubble constant have been ongoing for decades [26, 53, 95]. Different techniques to measure the Hubble constant using data from either the early universe or late universe have led to what is known as the Hubble tension. Measurements from CMB and early universe data give values for H_0 around 67-68 km s^{-1} Mpc^{-1} [5, 85], while distance-ladder measurements from supernovae or cephieds (late universe) give values of H_0 around 73-74 km s^{-1} Mpc^{-1} [84, 89, 91, 92]. The most recent constraints for H_0 come from the DESI survey [33], which combines measurements from large scale structure analyses with constraints on the sound horizon to find $H_0 = 68.52 \pm 0.62$ km s^{-1} Mpc^{-1}. As shown in figure 1.2, this result is still in tension with the latest value from SH0ES ($H_0 = 73.04 \pm 1.04$ km s^{-1} Mpc^{-1} [92]) at the 3.7σ level.

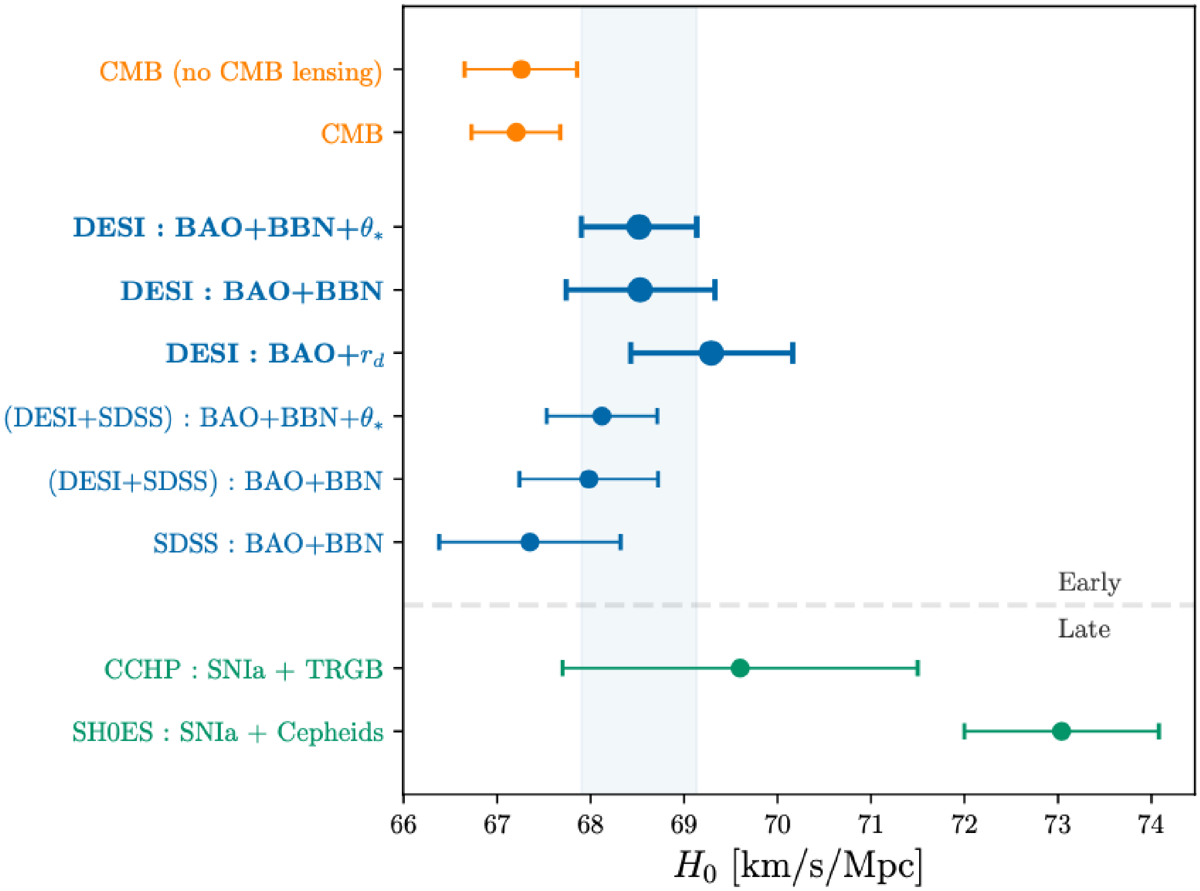

Figure 1.2: The latest results from DESI showing the value of H_0 and the continuing Hubble tension. The orange points show the results from CMB measurements with Planck and ACT. The bold blue points show the values from DESI. The thin blue points show the values from DESI combined with data from SDSS. The green points show the values from supernova measurements with either Cepheids or Tip of the Red Giant Branch (TRGB) stars. Figure from [33].

In order to obtain accurate measurements on the Hubble constant we must accurately obtain distances to objects. As the universe expands according to the scale factor, so too does the physical distance between objects. However, the comoving distance between two objects is referenced to t_0 and remains constant with the Universe's expansion in the absence of peculiar velocities. The comoving distance, D_C is related to the Hubble rate by

$$D_C(z) = D_H \int_0^z dz' \frac{H_0}{H(z')}, \tag{1.5}$$

where D_H is the Hubble distance and is equal to c/H_0. D_C is the comoving distance parallel to the line-of-sight. For a flat universe, the transverse comoving distance (perpendicular to the line-of-sight), D_M, is equal to D_C. Other distances are the angular diameter distance, D_A, and the luminosity distance, D_L:

$$\begin{aligned} D_A &= a(t)D_C = \frac{D_C}{1+z}, \\ D_L &= \frac{D_C}{a(t)} = D_C(1+z), \end{aligned} \tag{1.6}$$

where $a(t)$ is the scale factor at time t and z is the corresponding redshift. More detailed calculations of these distances can be found in [40, 63].

The rate of the Universe's expansion is directly tied to its composition. For a general, multi-component universe, we use the Friedmann equation

$$\frac{H(t)^2}{H_0^2} = \frac{\varepsilon(t)}{\varepsilon_{c,0}} + \frac{1-\Omega_0}{a(t)^2}, \tag{1.7}$$

where H is the Hubble rate, $\varepsilon(t)$ is the total energy density in the universe, and $\varepsilon_{c,0}$ is the critical density, often denoted ρ_{crit}. The right hand term of equation 1.7 describes the curvature of the universe, with $\Omega_k = 1 - \Omega_0$. The energy density of each species, Ω_x is calculated as the ratio of the present day energy density, ε_x, and the critical density

$$\Omega_x = \frac{\varepsilon_x}{\rho_{\text{crit}}}. \tag{1.8}$$

The current Benchmark Model for a flat ΛCDM universe includes matter, Ω_m, (both baryonic and dark matter) and dark energy, Ω_Λ. The Friedmann equation that describes the evolution of the scale factor in this universe is then

$$\frac{H(a)^2}{H_0^2} = \frac{\Omega_m}{a^3} + \frac{\Omega_r}{a^4} + \Omega_\Lambda. \tag{1.9}$$

Figure 1.3 shows the energy densities for matter, radiation (including neutrinos), and dark energy as a function of scale factor. The flat ΛCDM model has no curvature, i.e, $\Omega_k \equiv 1 - \Omega_0 = 1 - \Omega_m - \Omega_r - \Omega_\Lambda = 0$. A universe with curvature would have $\Omega_k < 0$ for a closed universe or $\Omega_k > 0$ for an open universe.

For a time-independent model, the energy density ε_x for a species in the universe will be

$$\frac{\varepsilon_x}{\varepsilon_{x,0}} = a^{-3(1+w_x)} = (1+z)^{3(1+w_x)}, \tag{1.10}$$

where $w_x \equiv P_x/\varepsilon_x$ is the equation of state parameter and is the ratio of a component's pressure to its energy density. For dark energy (cosmological constant), $w = -1$ and $\varepsilon_\Lambda = \varepsilon_{\Lambda,0}$, while for radiation $w = \frac{1}{3}$ and $\varepsilon_r = \varepsilon_{r,0}a^{-4}$, and for non-relativistic matter $w = 0$ and $\varepsilon_m = \varepsilon_{m,0}a^{-3}$. Equation 1.10 assumes that w_x is time-independent, however this does not have to be true. For a time-dependent (i.e, scale factor dependent) w_x, equation 1.10 turns into:

$$\varepsilon_x(a) = \varepsilon_{x,0} \exp\left[-3\int_1^a \frac{da'}{a'}[1 + w_x(a')]\right]. \tag{1.11}$$

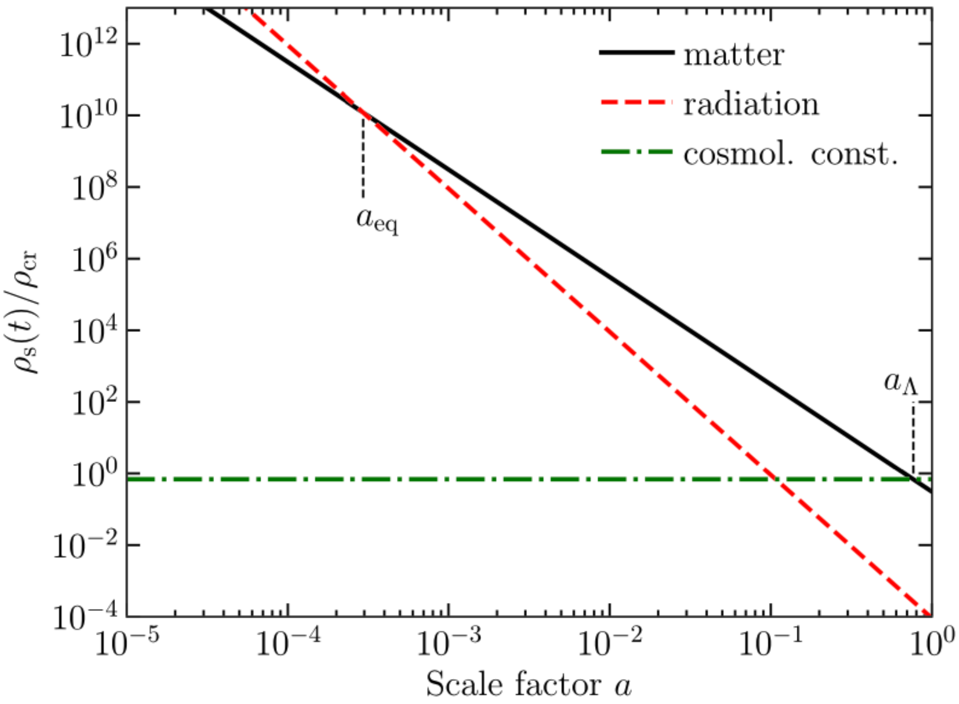

Figure 1.3: Energy density as a function of scale factor for matter (solid black line), radiation (dashed red line), and dark energy (dot-dashed green line). Where the matter and radiation lines cross, a_{eq}, is known as matter-radiation equality, which is when the universe transitioned from radiation to matter dominated. Similarly, where the matter and dark energy lines cross, a_Λ, is where the universe transitioned from matter to dark energy dominated. Figure from [39].

For the time-independent solution equation 1.11 simplifies to equation 1.10. If we adopt $w(z) = w_0 + w_1 z$ for dark energy then $\varepsilon_\Lambda(a) = \varepsilon_{\Lambda,0}(1+z)^{3(1+w_0-w_1)}e^{3w_1 z}$. However this form is unstable for redshifts $z > 1$. Instead, it is more common to parameterize the equation of state with

$$w(a) = w_0 + w_a(1-a), \tag{1.12}$$

as this form correctly models behavior at low and high redshifts. The exponential in equation 1.11 then gives $\varepsilon_\Lambda(a) = \varepsilon_{\Lambda,0}a^{-3(1+w_0+w_a)}e^{-3w_a(1-a)}$. Here w_0 is the value of the equation of state at the current time and w_a controls the amount of time variation. Models that favor dark energy as a cosmological constant (i.e, not time-varying) will have $w_a = 0$, and ΛCDM has $w_0 = -1$ and $w_a = 0$.

The most recent constraints on w_0 and w_a come from DESI [33]. DESI alone does not have enough power to break the degeneracy between the two parameters w_0 and w_a so the results are cut off by the priors used. However, they find $w_0 = 0.55^{+0.55}_{-0.21}$ and $w_a < -1.32$ when using only DESI BAO results. Figure 1.4 shows the constraints on w_0 and w_a for DESI BAO combined with other datasets. Each combination favors $w_0 > -1$ and $w_a < 0$, and are in tension with ΛCDM at the $2.5 - 4\sigma$ level [33]. DESI alone does not give a preference for an evolving dark energy model ($w_0 w_a$CDM in [33]) compared to ΛCDM, however, when combined with CMB and SNIa data there is a preference at the $2.5 - 4\sigma$ level for $w_0 w_a$CDM compared to ΛCDM. These results come from only one year of the DESI survey. Tighter constraints are expected from future DESI data releases.

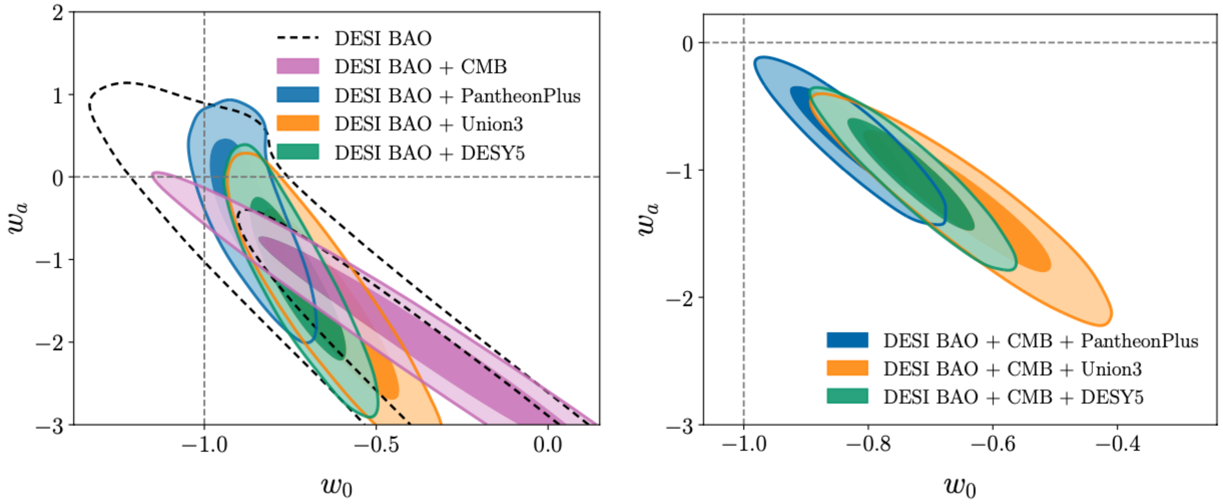

Figure 1.4: Constraints from DESI on w_0 and w_a using DESI BAO results combined with CMB data and multiple SNIa datasets. Each combination favors $w_0 > -1$ and $w_a < 0$. Figure from [33].

1.2 Probes of Large Scale Structure

The largest ever 3D map of the universe is currently being made by DESI. A slice of the cosmic web and large scale structure in the first year of DESI data is shown in figure 1.5, where each tracer's (galaxy, quasar, etc.) redshift is plotted and shown in a different shade of blue. The underlying large-scale structure of matter is clearly seen in the zoomed in portion of the map, with many filaments and walls forming in the bright high-density areas and voids forming in the dark low density areas.

Early time calculations of H_0 can be made by measuring the clustering of matter on large scales. By comparing measurements from early times when the universe was matter dominated to measurements from late times (SNIa) when the universe is dark energy dominated, we can quantify how dark energy is affecting the expansion of the universe. There are many ways to make this measurement but arguably the most effective is to use Baryon Acoustic Oscillations.

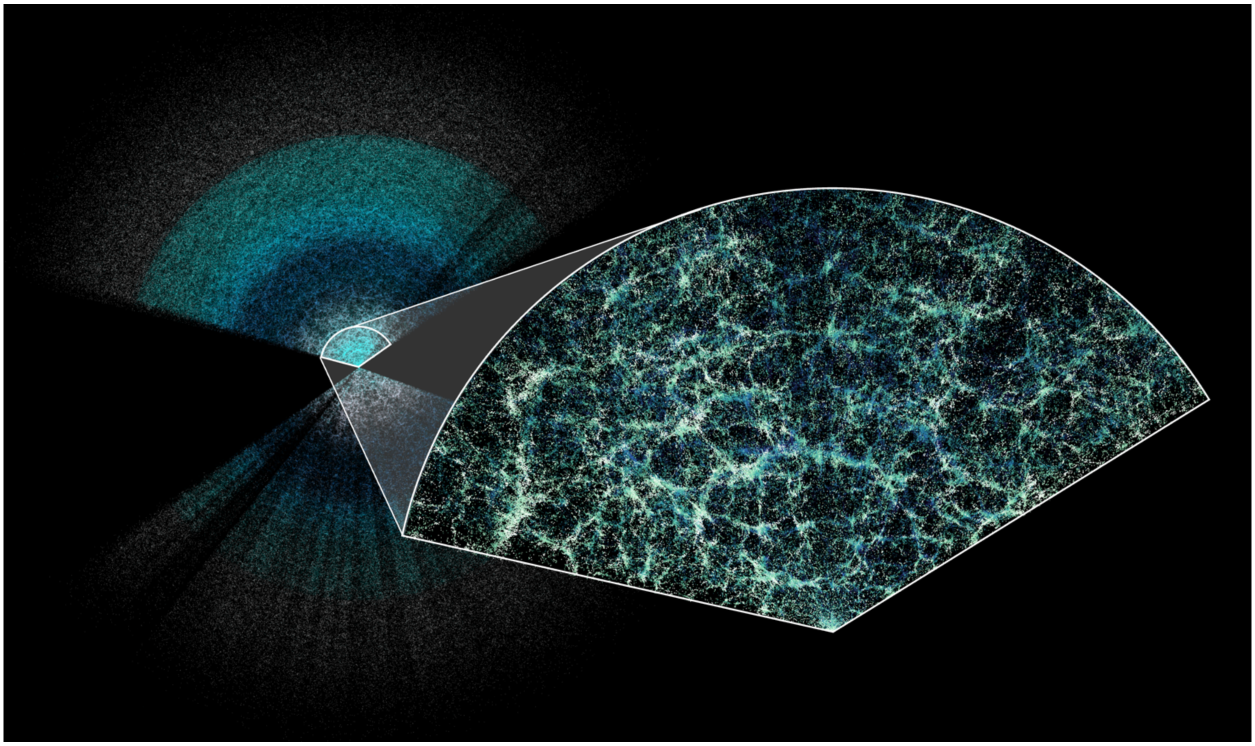

Figure 1.5: Cosmic web of DESI year 1 data. The different tracers are shown in different shades of blue. The underlying structure of matter is clearly seen in the zoomed in portion of the map. Figure credit: Claire Lamman/DESI Collaboration.

1.2.1 Baryon Acoustic Oscillations

Baryon Acoustic Oscillations (BAO) are sound waves that were imprinted in matter in the early universe. They are now “frozen” in the late-time clustering of matter and galaxies and act as a standard ruler for measuring distances. A full description can be found in [106] and [44] but we provide a brief description here.

Initial fluctuations in the primordial plasma created density and pressure waves that propagated through the early universe. At this time, the baryons and photons are tightly coupled in the plasma and the universe is hot and dense such that the plasma is ionized. These sound waves travelled away from their origin with a speed of approximately $c_s \approx c/\sqrt{3}$, while the dark matter perturbation grows in place. At recombination ($z = 1100$), the universe cooled enough for electrons and ions to recombine into neutral atoms, thus allowing photons to decouple from baryons. The baryon part of the sound wave is now “frozen” in place as the pressure from the wave is no longer driving the wave. An excess of matter was left at the source of the waves (from the dark matter perturbation) and where the waves terminated during recombination (from the baryons). As the universe becomes more matter dominated, the gravitational pull from the dark matter at the source and the baryons at the termination of the wave create over-densities of dark matter and baryons, leaving an imprint to be found in the large scale structure of galaxies and gas in the universe. The (co-moving) distance the baryon waves travelled before terminating is known as the *sound horizon* and is approximately 150 Mpc. The sound horizon is imprinted both along and across the line of sight:

$$r_d = \int_{z_d}^{\infty} \frac{c_s(z)}{H(z)} dz, \tag{1.13}$$

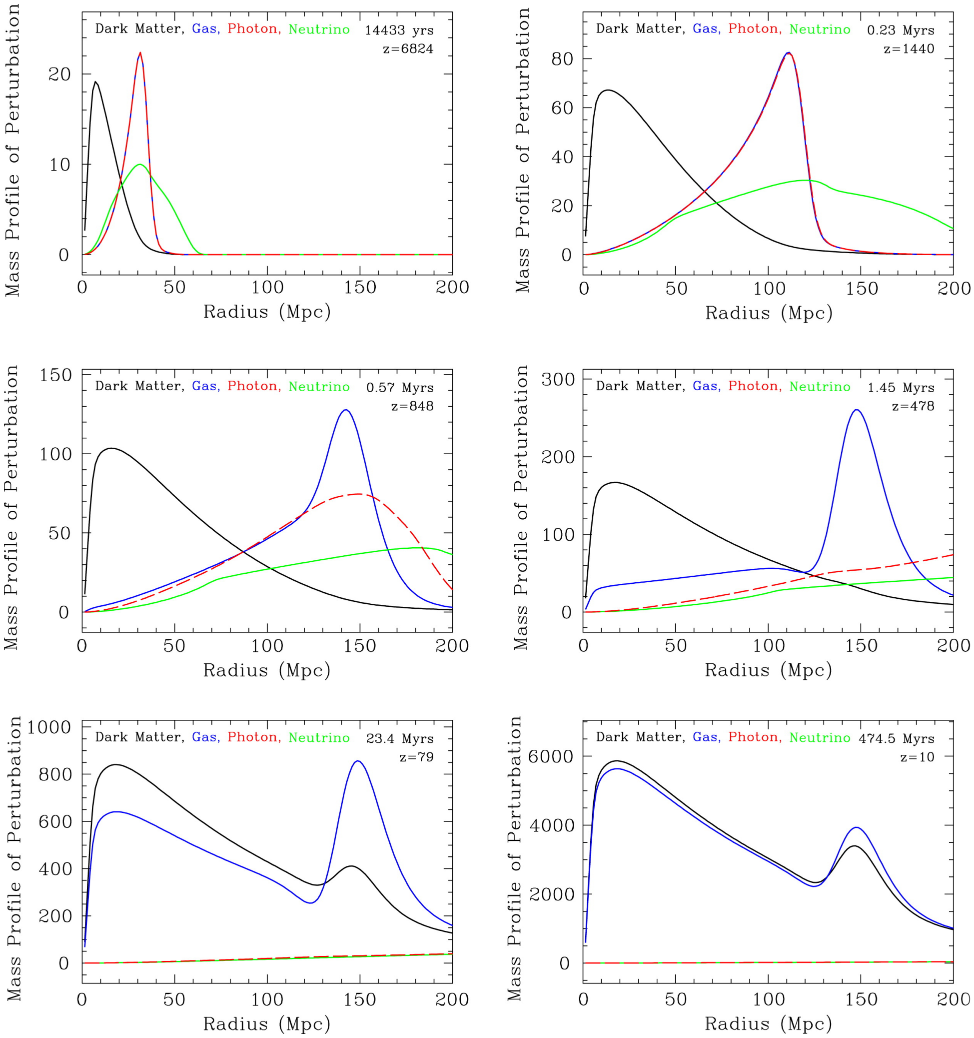

Figure 1.6: Snapshots showing the generation of the BAO peak from the initial perturbations in the primordial plasma. Each panel shows the radial perturbed mass profile for dark matter (black), baryons (blue), photons (red), and neutrinos (green). The redshift and time after the Big Bang are also given in each panel. Figure from [106] and [44].

where c_s is the sound speed [36], $H(z)$ is the Hubble rate at redshift z, and z_d is the redshift at the end of the baryon drag epoch. For BAO measurements, separations along the line of sight correspond to differences in redshift that depend on the Hubble parameter by $H(z)r_d$. Across the line of sight, separations correspond to differences in angle that depend on the angular diameter distance as $D_A(z)/r_d$.

BAO are measured by computing the 2-point correlation function (discussed in section 1.2.2) of different tracers at various redshifts. The Fourier transform of the correlation, the power

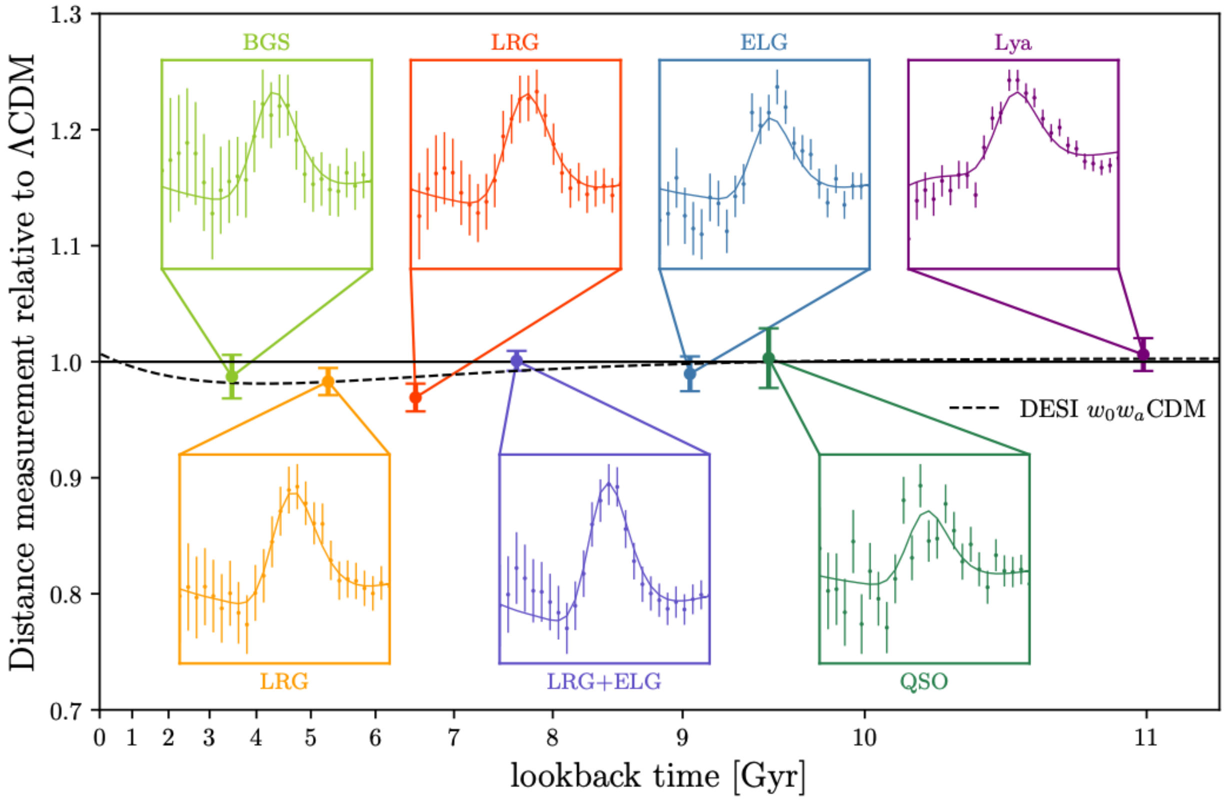

Figure 1.7: Newest distance measurements relative to ΛCDM for various tracers using BAO from DESI year 1 data. The BGS and two LRG tracers show a slight preference for the evolving dark energy, w_0w_aCDM, model. Figure from [28]. Figure created using data from [33].

spectrum, is also used to measure BAO. By observing the location of the BAO peak (r_d) in the correlation we can measure $D_A(z)$ and $H(z)$ to constrain cosmological models. The most recent measurements using BAO from various tracers comes from DESI and are shown in figure 1.7.

Tracers: Quasars and Galaxies

Galaxies have been used as tracers of the matter distribution for many years. Galaxies trace BAO at low redshifts, typically in the range $0 < z < 1.5$. The positions (redshifts) of each galaxy tracer are used to calculate the 2-point correlation function. There are different types of galaxy tracers that are used to probe different redshift ranges (see Table 2 of [35]). For example, in the DESI BAO galaxy results [35], bright galaxies (BGS) probe $0 < z < 0.4$, while luminous red galaxies (LRG) probe $0.4 < z < 1.1$ and emission line galaxies (ELG) probe $0.8 < z < 1.6$.

BAO was first detected in galaxy clustering by the Sloan Digital Sky Survey (SDSS, [45]) and the 2dF Galaxy Redshift Survey (2dFGRS, [24]). This prompted measurements from the next generation of surveys like the 6dF Galaxy Survey (6dFGS, [13]), the Baryon Oscillation Spectroscopic Survey (BOSS, [4]), the extended Baryon Oscillation Spectroscopic Survey (BOSS, [5]), and the WiggleZ Dark Energy Survey [14]. The most recent measurement is from DESI [35].

Quasars, or quasi-stellar objects (QSO) are among the most luminous sources in the universe and offer access to the highest extragalactic redshifts that can currently be observed. They have been used, both with galaxies and independently, as tracers to study the large scale structure of the universe and to probe the expansion history with BAO [19, 27, 43, 64, 81, 103]. In DESI [33, 35], quasars are used as tracers to probe redshifts in the range $0.8 < z < 2.1$.

Quasar spectra have broad and complex emission lines which can often cause errors on redshift measurements. Quasar spectra can also have broad absorption line (BAL) features that affect the absorption and emission blueward of the emission line centers. Damped Lyman Alpha (DLA) systems are often found in quasar spectra. While they do not affect redshift measurements, they can contaminate analyses of the power spectrum and correlation functions if not properly accounted for [52]. Figure 1.8 shows examples of a quasar spectrum, a BAL, and a DLA from the DESI DR1 data sample [29]. Some prominent emission lines (Lyman-α, CIV, CIII], and MgII) are highlighted in each spectra. The BAL quasar (middle plot) is particularly strong with the blueward portion of the CIV and SIV emission lines affected.

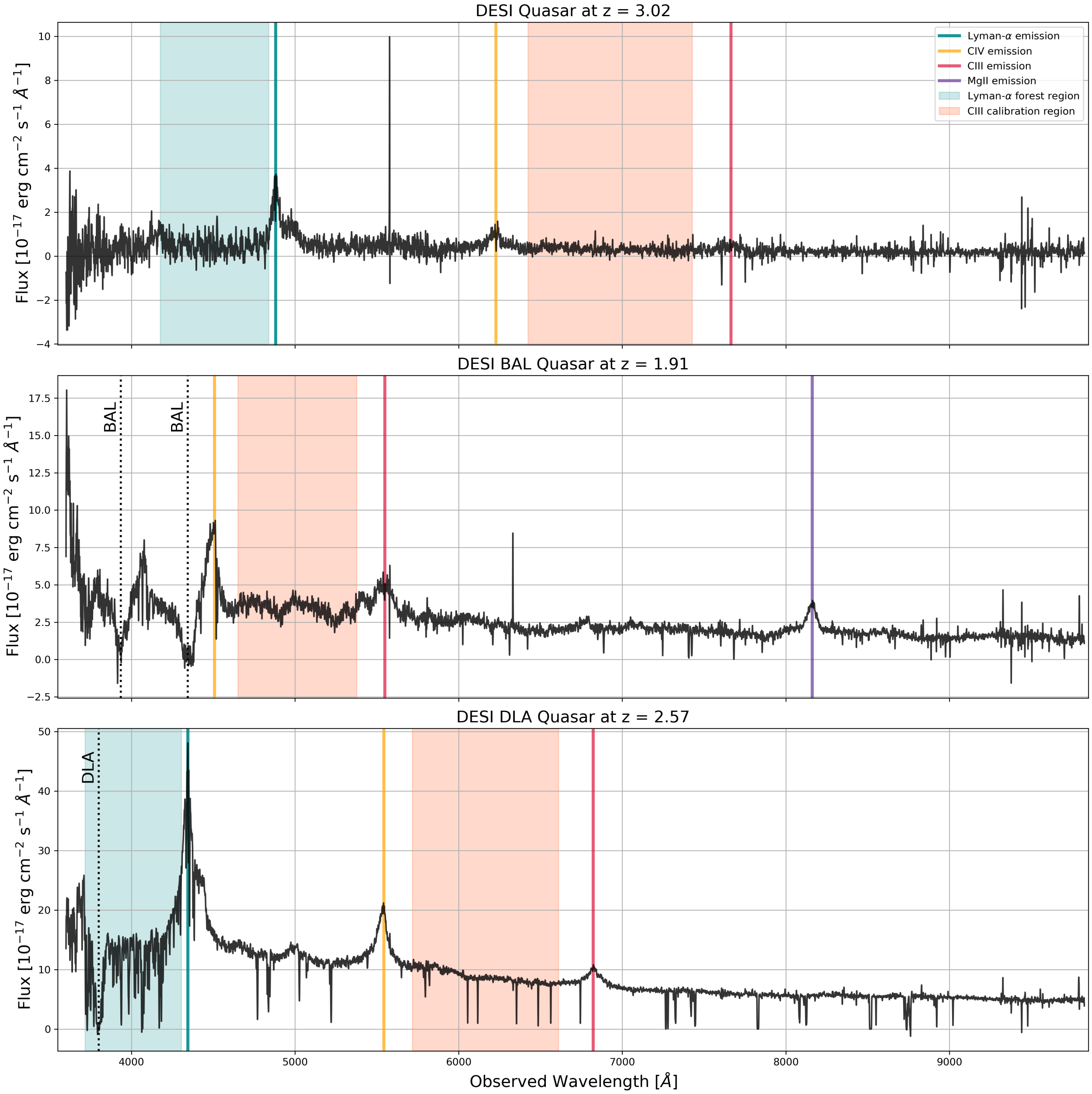

Figure 1.8: Three spectra from DESI DR1 showing a quasar at redshift $z = 3.02$ (top), a BAL quasar at redshift $z = 1.91$ (middle) and a DLA quasar at redshift $z = 2.57$ (bottom). The Lyman-α, CIV, CIII], and MgII emission lines are shown for each spectra where they are in range. Also highlighted are the Lyman-α forest region and the CIII] calibration region used in chapter 4.

Tracers: Lyman-α Forest

Observable galaxies become sparse at high redshifts however observable quasars are still abundant. At redshifts $z > 2.0$, visible wavelength quasar spectra feature the Lyman-α forest. The Lyman-α forest is a collection of absorption lines corresponding to neutral hydrogen in the intergalactic medium (IGM). The light from a distant quasar is constantly redshifting, and as it passes through the IGM it is absorbed and re-remitted, repeating many times to create a "forest" of absorption lines. The amount of absorption correlates to the density of neutral hydrogen. This also traces the underlying dark matter on large scales since it is coupled with baryonic matter (i.e, neutral hydrogen).

The use of the Lyman-α Forest to measure the structure in the universe was first done in BOSS [102]. The first detection of BAO using the Lyman-α forest was released by BOSS a few years later [19, 74, 103]. The eBOSS collaboration also released measurements of BAO with the Lyman-α forest [43]. The most recent results come from the DESI collaboration [34] where they measure the BAO scale parallel ($\alpha_{\parallel}$) and perpendicular ($\alpha_{\perp}$) to the line of sight with a precision of 2% and 2.4%, respectively.

1.2.2 Cosmology from Baryon Acoustic Oscillations

During the epoch of recombination, sound waves in the primordial plasma were imprinted into the present-day clustering of matter and galaxies as baryon acoustic oscillations. The fluctuations of the sound waves are what we see in the large scale structure today as galaxies, clusters, voids, and filaments. The BAO in this structure presents itself in two ways [98]:

1. as Doppler peaks, or "wiggles" in the anisotropies of the CMB (matter power spectrum), shown in the left plot of figure 1.9
2. as a peak in the amplitude of matter fluctuations as a function of scale (correlation

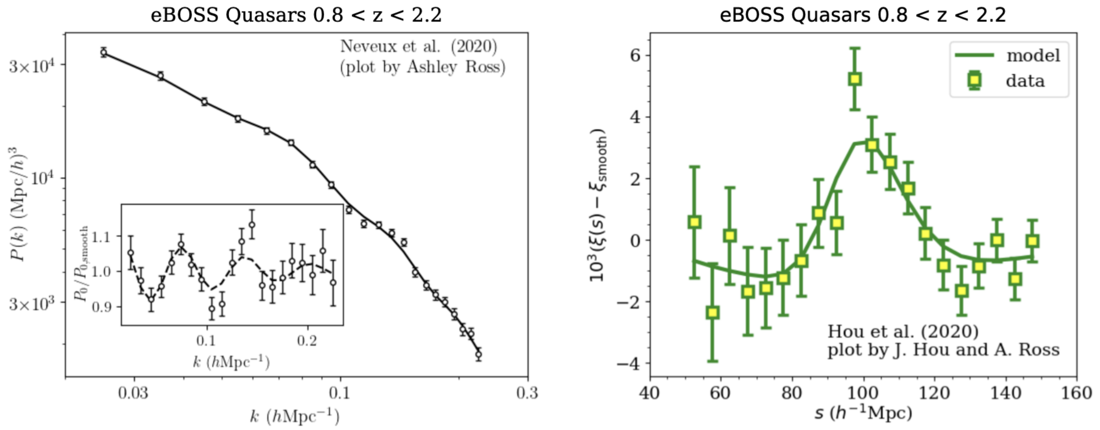

Figure 1.9: Examples showing the "wiggles" in the power spectrum (left) and the BAO peak in the correlations (right) from the measurement with eBOSS quasars at $0.8 < z < 2.2$. Images from [81] (left) and [64] (right).

function), shown in the right plot of figure 1.9.

BAO provide a distance scale of known size (also known as a standard ruler) which allows us to compute the angular diameter distance (equation 1.6) and the Hubble distance at different redshifts. By measuring the oscillations along and across the line of sight and then taking the ratio with the known physical scale r_d, we can measure $D_A(z)$ and $H(z)$ [46].

Matter Power Spectrum

In order to discuss the distribution of matter in the universe we first need to quantify how the density fluctuates. We define the matter density contrast as:

$$\delta(\mathbf{x}, t) \equiv \frac{\varepsilon_m(\mathbf{x}, t) - \overline{\varepsilon}_m(t)}{\overline{\varepsilon}_m(t)}, \tag{1.14}$$

where $\overline{\varepsilon}_m(t) = \frac{1}{V} \int_V \varepsilon_m(\mathbf{x}, t) d^3r$ is the average matter density at time t. δ will be positive in overdense regions and negative in underdense regions. Density fluctuations will evolve with time. Gravity will cause overdense regions to attract more matter and become more dense,

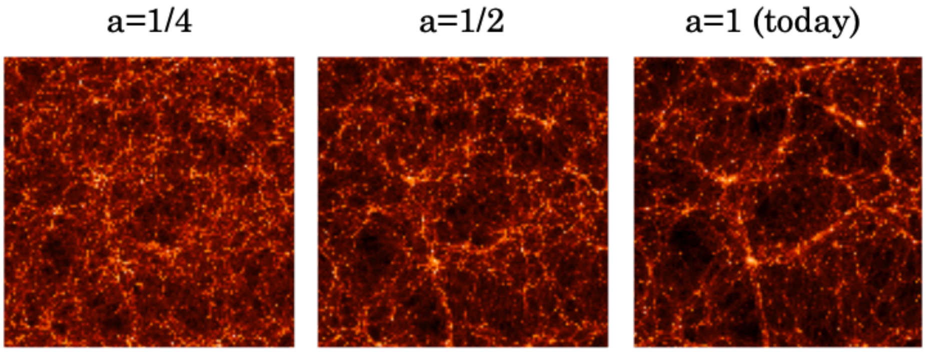

Figure 1.10: Snapshots from numerical N-body simulations by the Virgo consortium [67] following the ΛCDM model. The snapshots show a larger amplitude of fluctuations in the past (smaller a) compared to today. Figure from [66].

however, in contrast, the expanding universe will cause the overdense regions to become less dense. The growth of these fluctuations follows

$$\ddot{\delta}(\mathbf{x},t) + 2H\dot{\delta}(\mathbf{x},t) - \frac{4\pi G}{c^2}\bar{\varepsilon}_m\delta = 0, \tag{1.15}$$

where G is the gravitational constant, and $H\dot{\delta} = Hd\delta/dt$ is called the "Hubble friction" term acting to slow the growth of fluctuations in an expanding universe. In the linear regime (where $|\delta| \ll 1$), the linear growth function $D(a)$ is defined as a function of the scale factor as:

$$\delta(a) = D(a)\delta(a=1). \tag{1.16}$$

An example of how the fluctuations evolve with scale factor a in a ΛCDM universe is shown in figure 1.10. It is clear to see that matter is much more "clumped" at $a = 1$ than it was at earlier times.

The matter power spectrum $P(k)$ is the two-point correlation function of the Fourier Transform $\delta(\mathbf{k})$ of $\delta(\mathbf{r})$:

$$\langle\delta(\mathbf{k})\delta(\mathbf{k}')\rangle = (2\pi)^3\delta^{(3)}(\mathbf{k}-\mathbf{k}')P(k), \tag{1.17}$$

where $\delta^{(3)}$ is the 3D Dirac delta function and $|\mathbf{k}| = k$. The Fourier transform of the density contrast $\delta(\mathbf{k})$ and its inverse $\delta(\mathbf{r})$ are related by

$$\begin{aligned} \delta(\mathbf{k}) &= \int d^3r\ \mathrm{e}^{-\mathbf{k}\cdot\mathbf{r}}\delta(\mathbf{r}), \\ \delta(\mathbf{r}) &= (2\pi)^{-3}\int d^3k\ \mathrm{e}^{\mathbf{k}\cdot\mathbf{r}}\delta(\mathbf{k}). \end{aligned} \tag{1.18}$$

The power spectrum is expressed in terms of wavenumber $\mathbf{k}$ which corresponds to the different Fourier components of the density fluctuations. The mean square amplitude of the Fourier components defines the power spectrum such that $P(k) = \langle|\delta(\mathbf{k})|^2\rangle$. Results from [22] show the power spectrum $P_m(k)$ at $z = 0$ from Planck CMB data on large scales, SDSS galaxy clustering on intermediate scales, and SDSS Lyman-α clustering on the smallest scales.

A commonly used quantity used to describe the clustering is the rms amplitude of mass fluctuations on the scale R, σ_R. σ_R^2 is the variance of the mass fluctuations and is given by:

$$\sigma_R^2(a) = \int_0^\infty \frac{k^3 P_{\mathrm{linear}}(k,a)}{2\pi^2} W^2(kR) d\ln k, \tag{1.19}$$

where W is the Fourier transform of the real-space window function and P is the power spectrum defined according to linear theory. σ_R describes the amount of matter fluctuations averaged over a sphere of radius R at redshift z. A common choice is to use $R = 8\ h^{-1}$Mpc, with a top-hat realspace window function where $\sigma_8 \equiv \sigma_8(a = 1)$. We then define the parameter S_8

$$S_8 \equiv \sigma_8(\Omega_m/0.3)^{0.5}, \tag{1.20}$$

which is used to measure clustering in terms of σ_8 and the matter density parameter Ω_m.

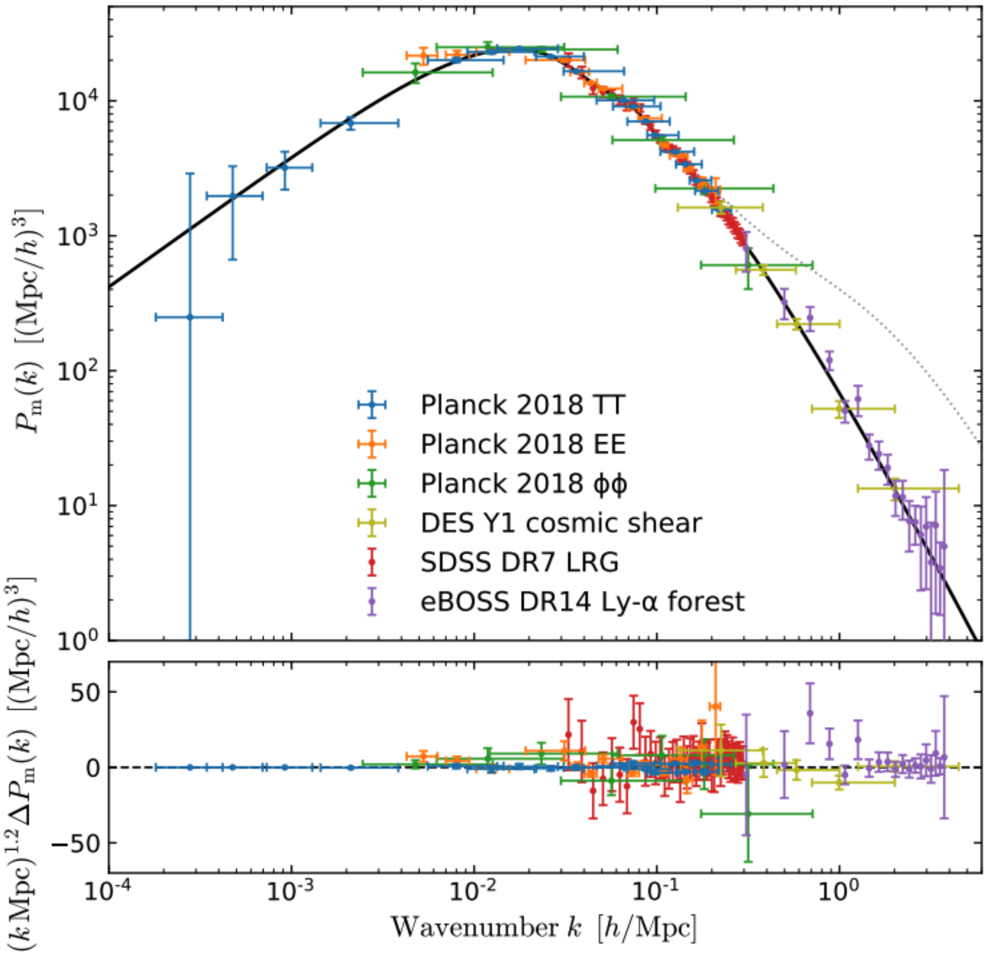

Figure 1.11: Top: 3D matter power spectrum at z=0 from Planck CMB (large scales, i.e, small k), SDSS galaxy clustering (intermediate scales), and SDSS Lyman-α clustering and DES cosmic shear (small scales, i.e, large k). The solid black line is the best-fit Planck 2018 ΛCDM model. Bottom: deviation of the data from the Planck 2018 best-fit ΛCDM model for ΛCDM 3D matter power spectrum. Figure from [22].

Correlation functions

The two-point correlation function is given by

$$\xi(\mathbf{r}) \equiv \langle \delta(\mathbf{x})\delta(\mathbf{x}+\mathbf{r}) \rangle, \tag{1.21}$$

with $\mathbf{r} = (r_\parallel, r_\perp)$ is the separation between two tracers along and across the line of sight. These distances are calculated by measuring the direct observables $\Delta\theta$ and Δz and assuming some cosmological model:

$$\begin{aligned} r_\parallel &= [D_c(z_i) - D_c(z_j)] \cos\left(\frac{\Delta\theta}{2}\right), \\ r_\perp &= [D_M(z_i) + D_M(z_j)] \sin\left(\frac{\Delta\theta}{2}\right), \end{aligned} \tag{1.22}$$

where $D_c(z) = c/H(z)$ is the comoving distance and $D_M(z) = (1+z)D_A(z)$ is the angular diameter distance. As a function of $\Delta\theta$ and Δz, the correlation function is calculated as

$$\begin{aligned} \xi(\Delta\theta, \Delta z) &= \langle \delta(\theta_1, z_1)\delta(\theta_2, z_2) \rangle \\ &\propto \frac{1}{N} \sum_{\text{all pairs}} \delta(\theta_1, z_1) \times \delta(\theta_2, z_2), \end{aligned} \tag{1.23}$$

where $|\theta_1 - \theta_2| \approx \Delta\theta$ and $|z_1 - z_2| \approx \Delta z$ for all pairs. For the various tracers, the position information is observed directly. However the Lyman-α forest is treated a little differently because there can be multiple absorption lines at different redshifts in one forest. Instead of using one position, using the Lyman-α forest tracer measures correlations between the transmitted flux (absorption) along the line of sight of high redshift ($z > 2.1$) quasars.

The mean flux transmission field of a quasar q is defined as

$$\delta_q(\lambda) = \frac{f_q(\lambda)}{\overline{F}(\lambda) C_q(\lambda)} - 1, \tag{1.24}$$

where $f_q(\lambda)$ is the observed flux and $\overline{F}(\lambda)C_q(\lambda)$ is the mean expected flux. For the Lyman-α auto-correlation all the $\delta \rightarrow \delta_q$ in equation 1.23. The flux-transmission δ_q is broken down into "pixels" and then the correlation function is estimated by

$$\xi_A = \frac{\sum_{(i,j)\in A} w_i w_j \delta_i \delta_j}{\sum_{(i,j)\in A} w_i w_j}, \tag{1.25}$$

where i, j indicate two pixels, w_i and w_j are the weights of each pixel, and δ_i and δ_j are the flux transmission field from equation 1.24 for two pixels. For the cross-correlation of Lyman-α with another tracer, like quasar position, the flux transmission for the new tracer is equal to one, and the estimator is then:

$$\xi_A = \frac{\sum_{(i,j)\in A} w_i w_j \delta_i}{\sum_{(i,j)\in A} w_i w_j}. \tag{1.26}$$

In this case i indexes the Lyman-α pixel and j indexes the quasar. Correlations are measured in bins of $r_\parallel$ and $r_\perp$, typically out to 200 h^{-1} Mpc, or roughly twice the BAO scale. The correlations are then fit to a theoretical model. For the Lyman-α auto-correlation this model is:

$$\xi^t = \xi^{Ly\alpha \times Ly\alpha} + \sum_m \xi^{Ly\alpha \times m} + \sum_m \xi^{m_1 \times m_2} + \xi^{sky}, \tag{1.27}$$

where the first term is the component for the Lyman-α absorption, the next two terms are the components for correlations of Lyman-α absorption with metals and other absorbers, and the final term is for any correlations from sky subtraction. For the cross-correlation of Lyman-α with quasars this model looks slightly different:

$$\xi^t = \xi^{Ly\alpha \times \mathrm{QSO}} + \xi^{\mathrm{QSO} \times m} + \xi^{\mathrm{TP}}. \tag{1.28}$$

The differences here (compared to the auto-correlation) are that there is no term for sky

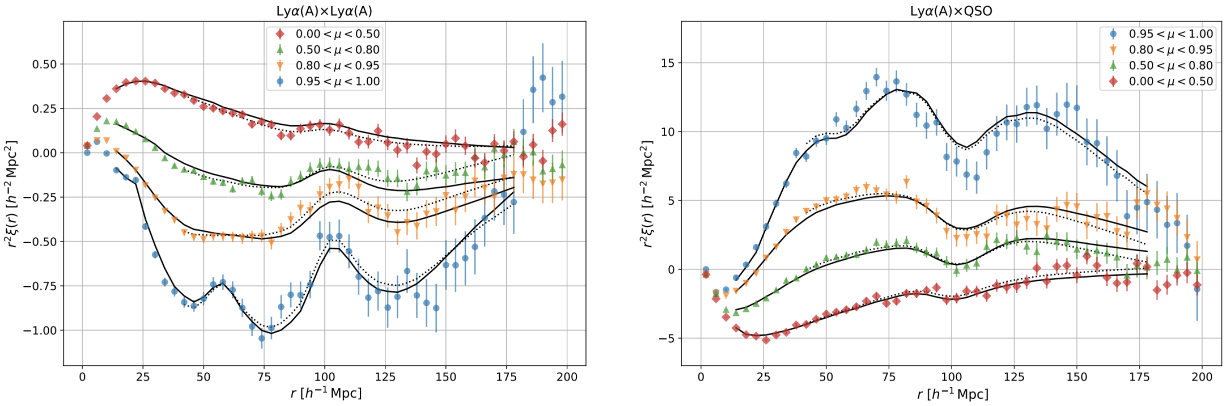

Figure 1.12: Lyman-α auto- and cross-correlations from DESI year 1 data. Each plot shows the correlations for different angular separations on the sky, parameterized by $\mu = r_{\parallel}/r$, where $\mu \to 1$ indicates separations along the line of sight and $\mu \to 0$ indicates separations across the line of sight. Figure from [34].

subtraction and there is an additional term to account for the transverse proximity effect (TP) (which is the effect of radiation from the quasar on the nearby surrounding gas).

The most recent results for both the auto- and cross-correlations of the Lyman-α forest come from DESI. The Lyman-α auto-correlation and the cross-correlation with quasars was measured using the DESI EDR[1] in [56]. The most recent results come from DESI DR1[2] and the Lyman-α auto-correlation and cross-correlation with quasars from [34] results are shown in figure 1.12. The correlations are shown for four different angular separations on the sky, parameterized by $\mu = r_{\parallel}/r$, along ($\mu \to 1$) and across ($\mu \to 0$) the line of sight. The left panel shows the auto-correlation and the right panel shows the cross-correlation with quasars.

---

[1] EDR is available at: `https://data.desi.lbl.gov/doc/releases/edr/`

[2] DR1 will be available in 2025 at: `https://data.desi.lbl.gov/doc/releases/`

1.3 From Stage-IV to Stage-V Experiments

The mission of stage-IV dark energy experiments is to determine and understand the nature of dark energy and how it is driving cosmic expansion. Stage-IV experiments are also anticipated to increase the Dark Energy Task Force (DETF) figure of merit (FOM) by a factor of 10 compared to Stage-II and Stage-III experiments [2]. While some Stage-IV experiments have already begun, others will come online within the next decade. The timeline for the surveys discussed in this section is shown in figure 1.14.

1.3.1 DESI, DESI-ext, and DESI-2

The Dark Energy Spectroscopic Instrument (DESI), is a Stage-IV experiment that began collecting data in 2021 and surpassed the power of Stage-III surveys within the first year. DESI will provide the largest 3D map of the universe to study the expansion history of the universe via baryon acoustic oscillations (BAO) and to study the growth of structure via redshift space distortions (RSD) [76]. The DESI instrument and survey are described in detail in Chapter 2.

An extension to the DESI survey, called DESI-ext, is planned (but not yet approved by DOE) to start immediately after the DESI main survey ends. DESI-ext would run for approximately 2.5 years and no instrument upgrades are planned. The survey would have the same targets as DESI, but the footprint would expand by 20% to 17,000 deg^2. The primary goal of the extension is to increase the precision of the BAO measurement. This can be done in three ways: increasing target density, especially for LRGs, increasing the completeness, especially for ELGs, and increasing the survey footprint.

The DESI-2 program has been proposed and recommended to the DOE by the Particle Physics Projects Prioritization Panels (P5). DESI-2 will consist of new target types and science objectives, with a priority to validate the high redshift program for Spec-S5. The focus would be on high redshift galaxies such as LAEs and LBGs, as these will provide dark energy constraints further into the matter dominated regime than provided by DESI. Parts of the DESI instrument would be upgraded for DESI-II. It is planned to upgrade the CCDs in the blue arm of the spectrographs to reduce the amount of read noise. The DESI-2 survey would begin in 2029 and run for 6 years.

Both the DESI-ext and DESI-II surveys would complement the science being done by Rubin's LSST.

1.3.2 LSST

Rubin Observatory's Legacy Survey of Space and Time (LSST) is another Stage-IV experiment that is set to see first light in 2025 and the 10 year survey will begin roughly 4 to 7 months later[3]. LSST is a 6-band optical survey that will map a 20,000 deg^2 area in the southern sky [78]. LSST has four main science goals: making an inventory of the solar system, mapping the Milky Way, exploring the transient sky, and probing dark energy and dark matter.

LSST was designed to scan the sky in a single pass, with an observing strategy that is wide, deep, and fast. This strategy is called the"universal cadence" and will make up about 90% of of observing time. The other 10% will be reserved for very deep observations, observations requiring short revisits, and observations of special regions [78]. Individual observations, or a "visit", consist of a pair of 15-second exposures performed back to back in a given filter. Each field is projected to be observed twice, with at least 15 to 60 minutes between visits.

To achieve this level of efficiency, the LSST instrument has an 8.4 meter primary mirror with a 3.5 deg field of view. There are 6 optical band filters, u, g, r, i, z, y that cover the

---

[3] As of June 2024: `https://www.lsst.org/about/project-status`

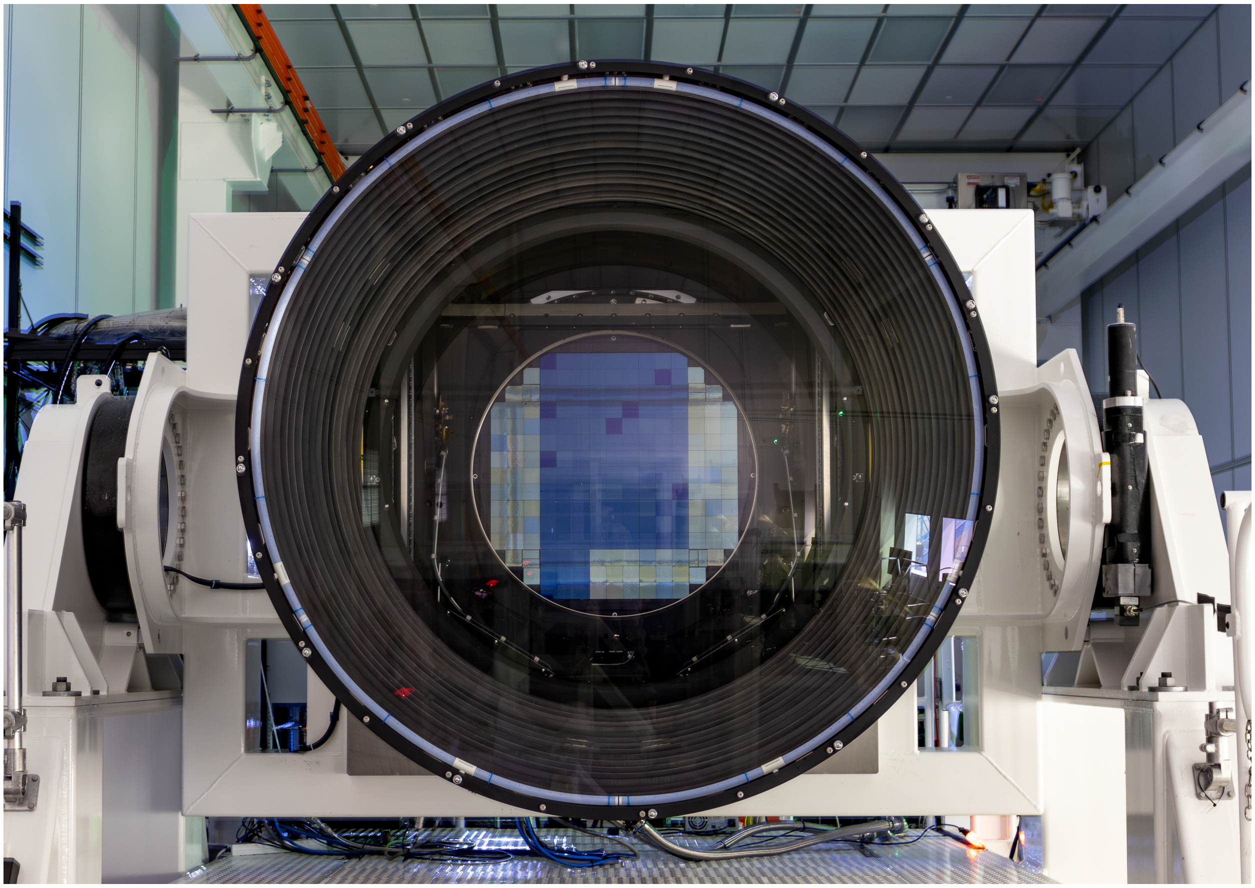

Figure 1.13: The completed LSST camera at SLAC National Accelerator Laboratory. Photo credit: Jacqueline Ramseyer Orrell/SLAC National Accelerator Laboratory.

wavelength range of 320 to 1080 nm. The focal plane, 0.6 m in diameter, is a 3.2-gigapixel camera/focal plane array (shown in figure 1.13) that consists of 189 CCD sensors each with a 10 μm pixel size. Once online, LSST will collect more than 60 petabytes of data over a decade.

1.3.3 Spec-S5

While the Stage-IV experiments are still ongoing, the scientific community is already looking ahead to future Stage-V experiments [97]. Spec-S5 is the proposed Stage-V ground-based spectroscopic experiment as a follow up to DESI. The recent 2023 P5 report [3] recommended support for Spec-S5 research and development such that a more mature Spec-S5 concept

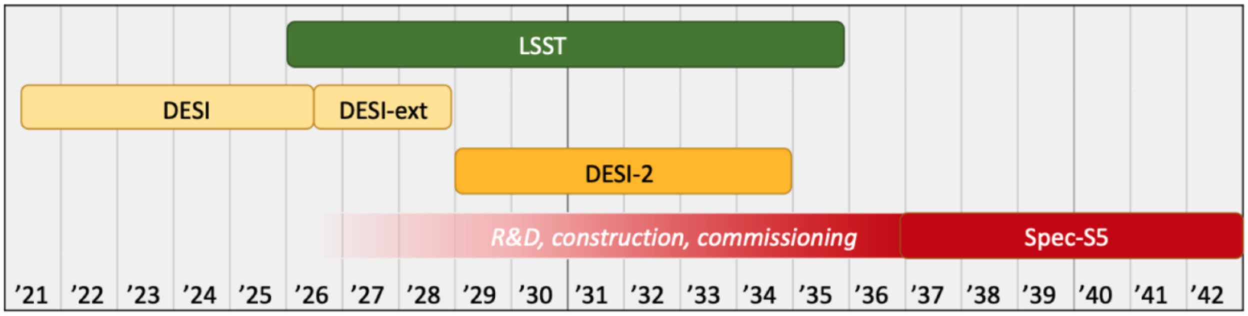

Figure 1.14: Timeline for the current Stage-IV surveys and proposed Stage-V survey Spec-S5.

could be considered for funding at the end of the current decade. The primary focus of Spec-S5 will be to understand inflation and dark energy with three main science categories: early universe physics and inflation, dark energy via BAO and redshift space distortions (RSD), and measuring the distribution of dark matter in the Milky Way. The information presented in this section is described in [105].

Early Universe Physics

Spec-S5 will study inflation and early universe physics by mapping primordial features in high redshift galaxies. At redshifts $z > 2$, the number density of galaxies and quasars visible by DESI is too small to do clustering and BAO measurements. Spec-S5 is projected to map 62 million galaxies at $z > 2$. In combination with an additional 100 million galaxies at $z < 2$, this will provide enough statistics to make BAO and RSD measurements to better than 1% precision in the redshift range $2.1 < z < 4.5$. This will also allow for better measurements of N_{eff} and $\sum m_\nu$ in the neutrino sector, as well as for better constraints on primordial non-Gaussianity and other inflationary physics.

Dark Energy

The recent results from DESI indicate a slight preference for evolving dark energy [33]. The DESI BAO measurement alone is not able to break the degeneracy between w_0 and w_a, however this preference still exists even with the addition of data from the CMB and SNIa. The full-sky coverage and improved target density will allow Spec-S5 to reach the precision necessary to confirm or refute evolving dark energy.

Dark Matter

Dark matter was discovered by Vera Rubin in the 1970s when she measured the rotation curves of galaxies and found that the velocities were too fast for the amount of visible matter. Over 50 years later the fundamental nature of dark matter has yet to be understood. Spec-S5 plans to build on early observations from DESI and will collect 50 million stellar spectra to explore the properties of dark matter. These spectra will consist of stellar streams and satellite galaxies that will allow for tests of dark matter models that impact structure formation on small scales.

Instrument

Spec-S5 will not be a brand new telescope. Instead, two existing telescopes, the Mayall at Kitt Peak National Observatory (KPNO) and the Blanco at Cerro Tololo Inter-American Observatory (CTIO) will be refurbished and upgraded to accommodate the Spec-S5 instrument. These two telescopes are currently 4-m telescopes, however the proposed plan is to modify the telescope mounts to accommodate 6-m mirrors at each site. This will allow for a more feasible optical corrector and instrument design while increasing the number of fibers at each telescope to 13 thousand. The fiber positioner design is not yet finalized, however

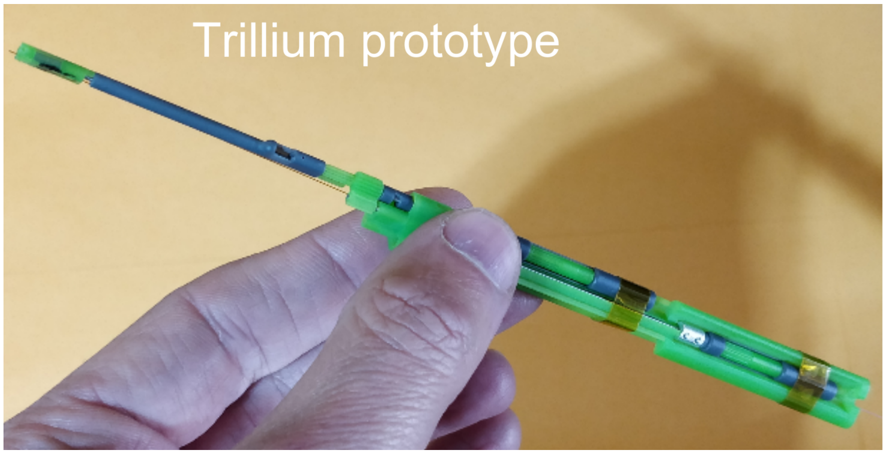

Figure 1.15: Trillium prototype design showing one-third of the assembly. The final design will have three arms, each with one fiber. Figure from [100]/Joe Silber (LBNL).

the leading design, called Trillium [97, 100], is similar in size and mechanical design to the DESI positioners. Instead of one fiber per assembly, the Trillium design allows for three fibers per assembly. An example of the trillium design is shown in figure 1.15.

Chapter 2

The Dark Energy Spectroscopic Instrument

2.1 The DESI Instrument

2.2 Focal Plane System

The DESI focal plane system contains both the Focal Plane Assembly (FPA) and the Fiber View Camera (FVC). The FPA consists of 10 petals, each with 500 robotic fiber positioners, 12 fiducials[1], and 1 guide-focus-alignment (GFA) CCD camera. Of the 10 total GFA cameras, 6 are used for guiding and 4 are used for maintaining focus within the instrument. All of the components of the FPA are concealed within a temperature and humidity controlled enclosure. This enclosure is mounted to the corrector such that the light from celestial objects reflects off the primary mirror, travels through the corrector, and lands on the focal plane where it is collected by the fibers. The FVC camera is mounted in the "donut hole"

---

[1] Two petals have 13 and 14 fiducials to break any symmetries from the FVC.

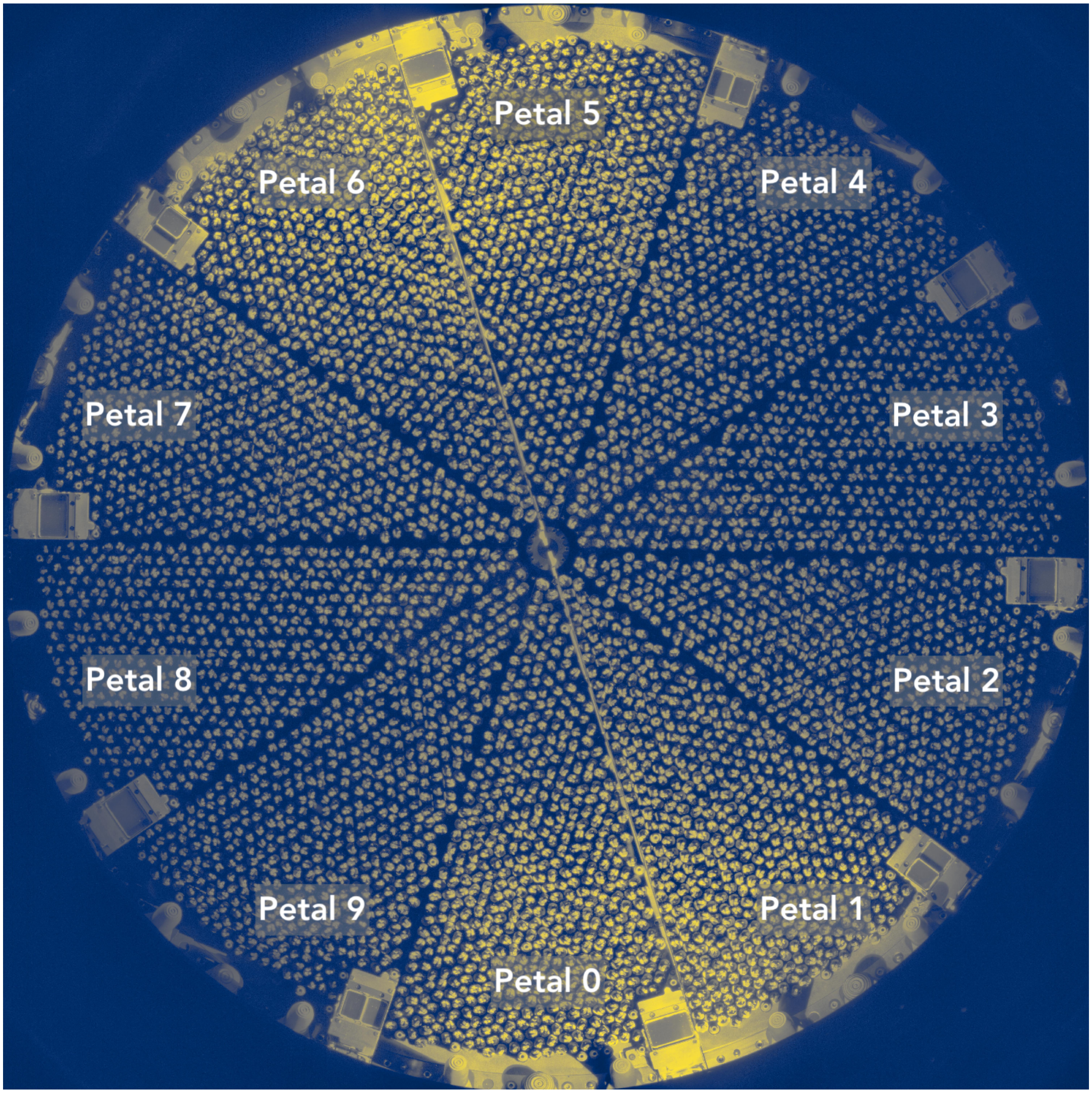

Figure 2.1: Front illuminated image of the focal plane with each petal labelled. Each petal contains 500 fibers, 1 GFA camera, approximately 12 fiducials, and 2 sky background fibers. Petals 0, 2, 3, 5, 7, and 8 contain guide GFAs, while petals 1, 4, 6, and 9 contain focus GFAs.

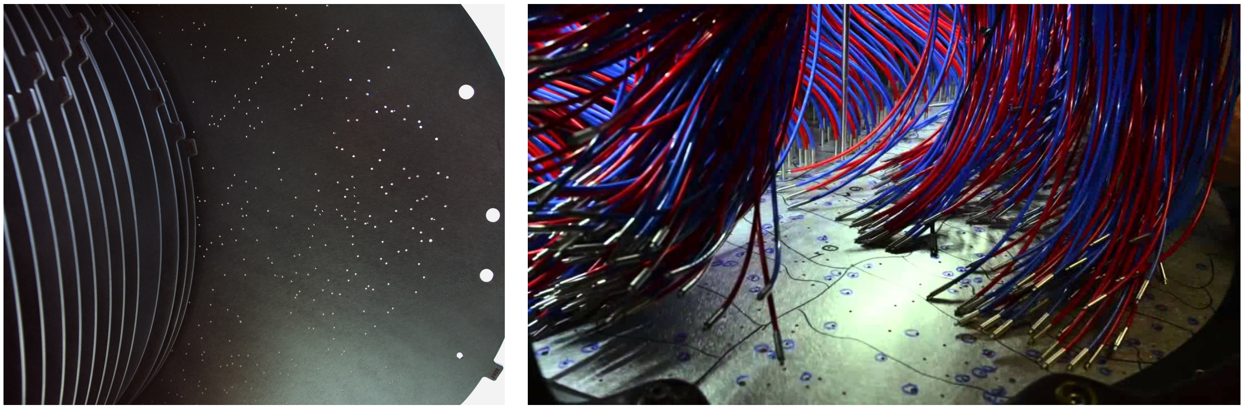

Figure 2.2: Examples of fiber plug plates from the SDSS instrument for the BOSS and eBOSS surveys. The left image shows a single plate with pre-drilled holes for the fibers to be plugged into. Image credit: David Kirkby. The right image shows a still from [7] where the fibers are being inserted by hand.

of the primary mirror and points at the focal plane through the corrector. The FVC is used to take images of the focal plane when the fiducials are illuminated and the fibers are back-illuminated from the spectrographs to measure their relative locations on the focal plane. An example of the back-illumination is shown in figure 2.7.

2.2.1 Fiber Positioners

The DESI robotic positioners are the first of their kind and allow for completed positioning within minutes. Prior to this, fiber plates were used where fibers had to be inserted by hand and often took around 20 minutes to complete (see figure 2.2).

The DESI positioners are gear-based positioners that have two rotational axes: theta (θ) and phi (ϕ), shown in figures 2.3, 2.4, and 2.5. The theta axis rotates about its center, while the phi axis rotates about an arm offset (nominally 3 mm) from the theta axis (“R1” in figure 2.5). The fiber tip is located 3 mm from the phi axis (“R2” in figure 2.5). This allows the robot to position the fiber anywhere within a 6 mm diameter patrol radius. The robots have a 10.4 mm pitch (i.e., the spacing between the center of one positioner and any of its

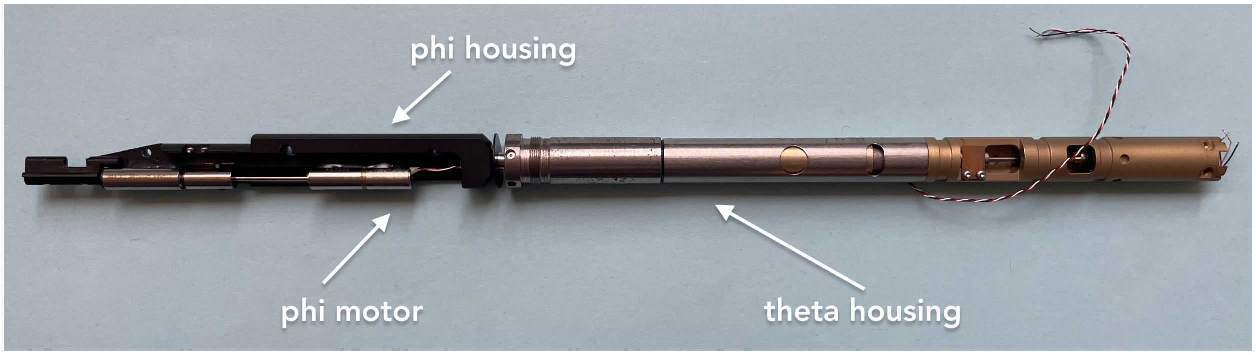

Figure 2.3: An image of a positioner with motors and axes labeled. The theta motor is not shown as it is inside the theta housing. This positioner does not have a fipos electronics board attached (as shown in figure 2.4), nor does it have a fiber in place.

neighbors), which necessitates the use of anti-collision software [101] to control any potential collisions between neighboring positioners.

Each positioner is controlled by two 4-mm DC motors for each theta and phi axis, shown in figures 2.3 and 2.4. The motors have gearbox with a fixed gear ratio (from the motor shaft to output at the fiber) of $\approx 1/337$. The motors are run at two speeds during positionings: a 9900 RPM “cruise” speed and a 150 RPM “creep” speed. The motors need an acceleration and deceleration phase to operate at the cruise speed, referred to as the ramp-up and ramp-down. At 9900 RPM this corresponds to $1.995 \times 2 = 3.99$ degrees at the output shaft (approximate rotational speed of $176^\circ\ \mathrm{s}^{-1}$). This drives the cutoff for the speed a robot will be commanded to move with. For any move request greater than 4 degrees, the move will occur at the cruise speed. Any move requests less than 4 degrees will be at the creep speed.

The typical move sequence within DESI consists of a blind move followed by a correction move. The blind move is usually a larger move at cruise speed. The correction move is usually a smaller move at creep speed. There are cases where the blind move is a small move at creep speed, and vice versa. The positioner performance for the first three years of the main survey, from May 14th, 2021 to April 9th, 2024, is shown in figure 2.6. As shown in the figure, the positioning error on the blind move (red histogram) is larger than the error for correction move (blue histogram), with an RMS error of 50 μm compared to an RMS error

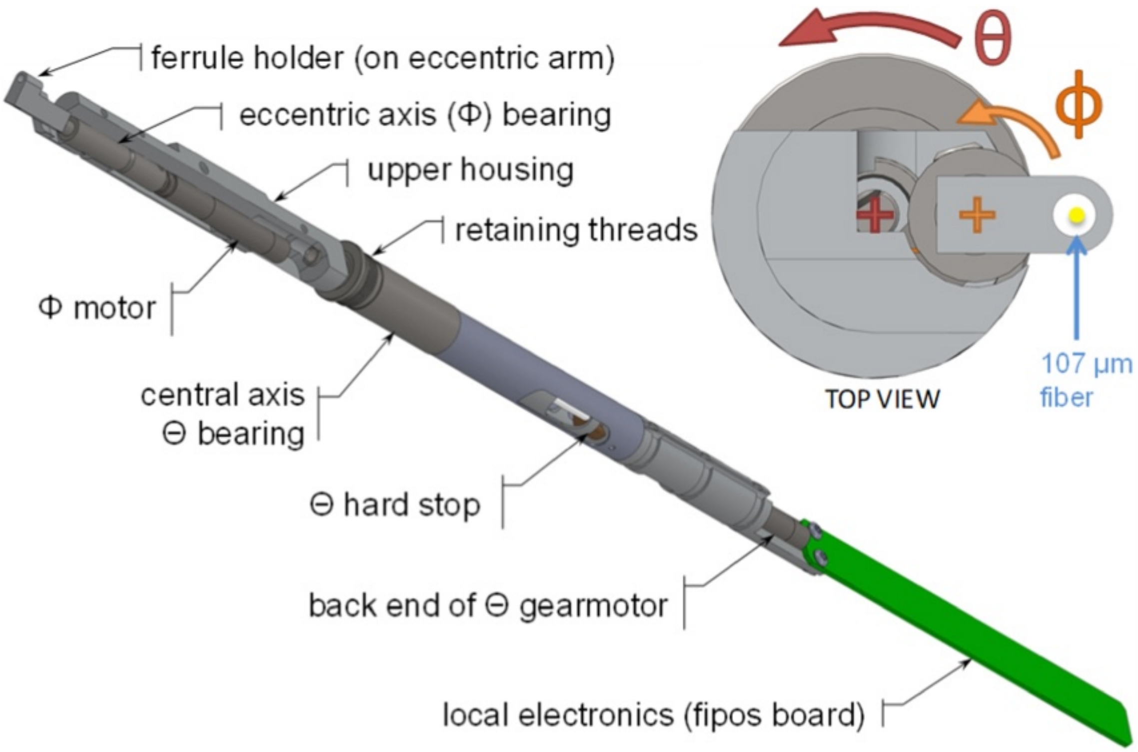

Figure 2.4: Drawing of a positioner with parts labeled. Also included is a diagram of the two rotational axes, θ and ϕ. Image from [101].

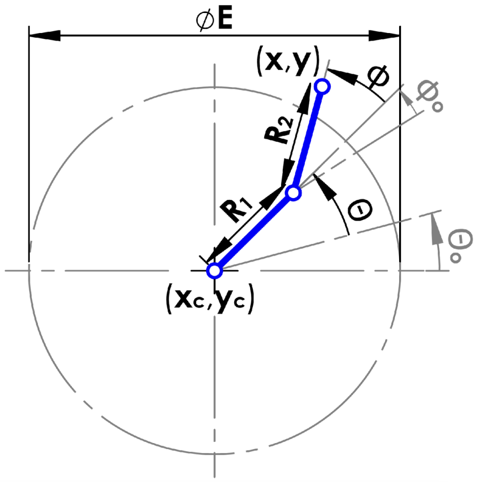

Figure 2.5: Schematic drawing showing the range of each positioner's rotational axes. "R1" is the θ arm and "R2" is the phi arm. When phi is fully extended the positioner will have an arm radius of 6 mm (nominal).

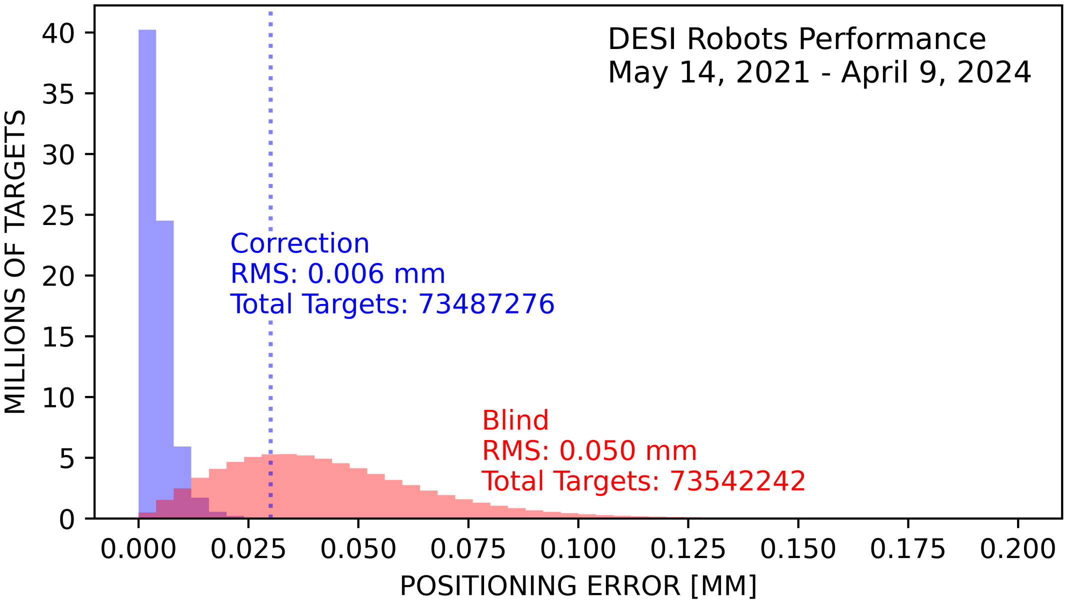

Figure 2.6: Positioning error for the first three years of the main survey from May 14th, 2021 to April 9th, 2024. The RMS of the positioning error for the blind move is 50 μm while the RMS of the positioning error for the correction move is 6 μm. These errors are calculated across all positioners with over 73 million total targets.

of 6 μm.

The positioners move using the "retract-rotate-extend" algorithm discussed in [101]. First, the phi arm is *retracted* such that the fiber tip is within the envelope E in figure 2.5. The positioner is then free to *rotate* about its theta axis without the risk of a collision. Once the theta axis is in position, the phi arm is then *extended* to place the fiber tip on its assigned on-sky target. This algorithm is designed to reduce the number of possible collisions, however they are not completely unavoidable, and the anti-collision software will then either pause a positioner while its neighbor moves or reject the move all-together.

The theta and phi axes both have physical limits to their rotation. Nominally, the limits are -5° $< \phi <$185° and -195° $< \theta <$ 195° [101]. There are mechanical hardstops at these limits that prevent the motors from rotating beyond these limits. The theta range is larger than

360°, meaning there is a 30° area where the fiber location can be degenerate, known as the ambiguous zone.

2.2.2 Fiducials

Spread throughout the focal plane are approximately 120 fiducials. The fiducials are used as reference points when calculating the physical positions of fibers on the focal plane from their pixel location in the FVC images.

Though all fiducials on the focal plane serve the same purpose, there are two types of fiducials: Field Illuminated Fiducials (FIFs) and Guide Illuminated Fiducials (GIFs). There are approximately 100 FIFs are spread throughout the focal plane among the positioners. Two GIFs are mounted on each GFA camera (section 2.2.3), for 20 total on the focal plane, and therefore need to be shorter than FIFs.

Each FIF is roughly the same size as a positioner, however, the tip of each fiducial differs as shown in figure 2.7. The tip of each fiducial is covered with a blue chrome glass diffuser. Four 10 μm diameter pin holes are etched in the glass that are then illuminated by a 470 nm LED light located within the body of the fiducial, shown in figure 2.7. The four dots are used as a standard pattern to allow the FVC to accurately measure fiber positions. Studies in [30] found that the positions of fibers and fiducials could be measured to 20 millipixels due to the resolution and stability of the FVC. An example of how fiducials appear in FVC images is shown in the right of figure 2.7.

2.2.3 Guide-Focus-Alignment CCDs

Along the edge of the DESI focal plane (see figure 2.1), there are 10 GFAs used for guiding and focusing the instrument. 6 are used as guider cameras with a flat surface and 4 are

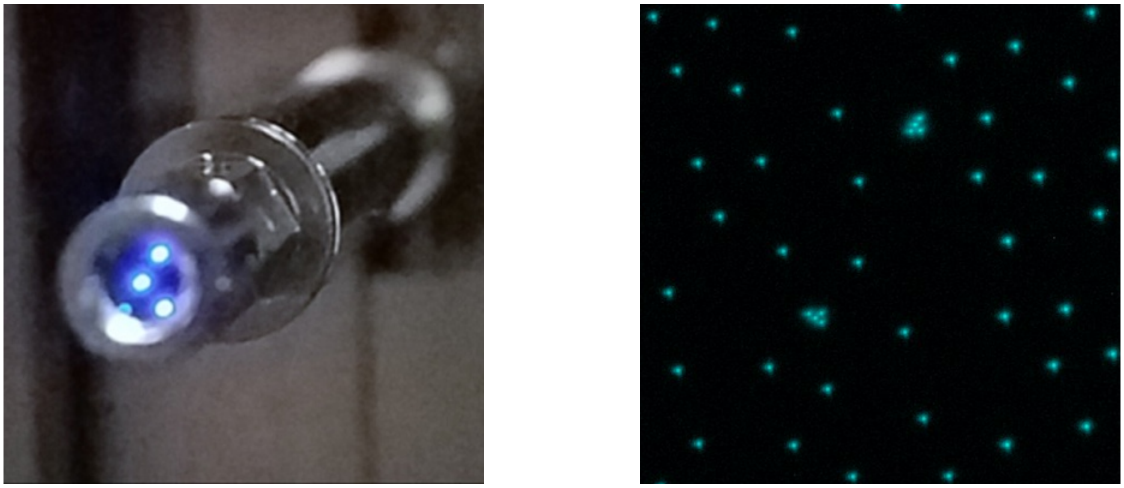

Figure 2.7: Examples of a fiducial among the focal plane (left) and as it appears in the FVC images (right).

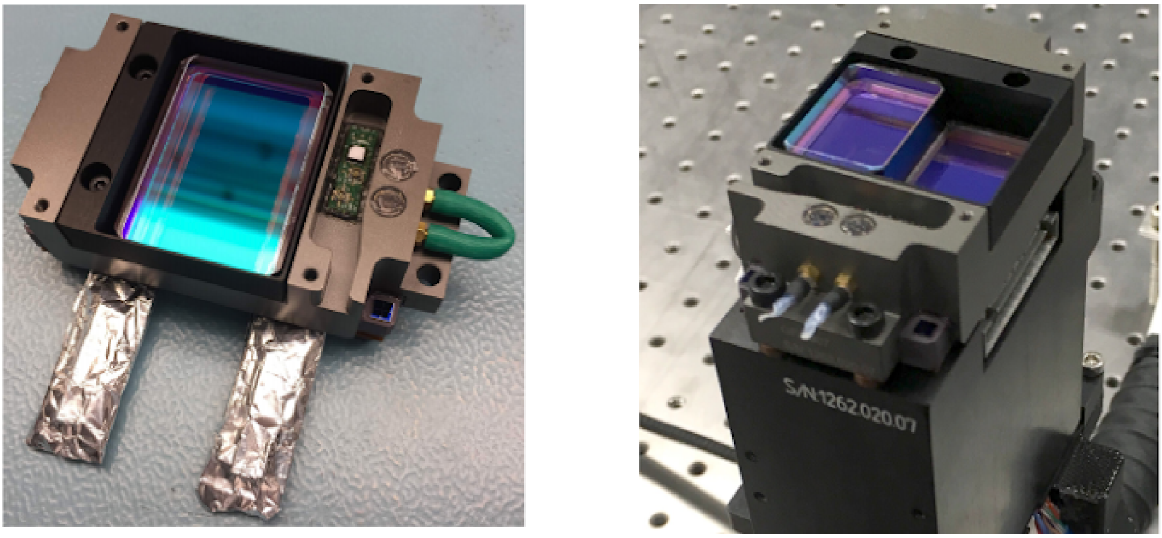

Figure 2.8: Guide and focus CCDs. Left image shows a guide CCD (which has a flat surface) and the right image shows a focus CCD (which has a stepped surface). Both CCDs have r-band filters.

wavefront sensors with a stepped surface. Both are shown in figure 2.8. Each CCD consists of an e2v Model CCD 230-42 [1] with a size of 2048 x 2064 pixels. We use the center 1024 x 2048 pixels for imaging (regions B and C in figure 2.9). The remaining sections are used as a frame store. The CCDs are read out through four amplifiers, shown in figure 2.9, and each amplifier has a pre- and post-scan region, also referred to as the overscan region.

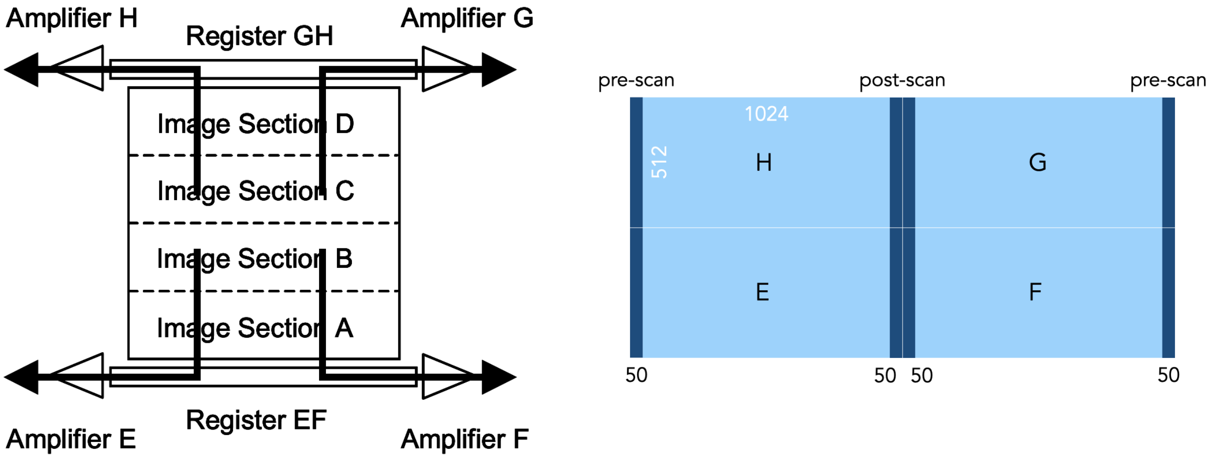

Figure 2.9: Examples of readout direction for the GFA CCDs. The left plot shows the 4-amp readout configuration. Sections B and C are the central region used for imaging. Sections A and D are the frame store regions. Image taken from [1]. The right plot shows the central imaging region of the CCD. The dark blue regions on the outer edge of each amplifier region are used as either a pre-scan or post-scan region.

All ten GFA cameras have an r-band filter placed directly in front of the CCD. As the cameras do not have a shutter, this filter was chosen to maximize signal from stars as well as to block the blue light when the fibers are back-illuminated and the fiducials are illuminated. The filter placed on the guider CCDs is 5 mm thick. The wavefront CCDs are designed to be out of focus across the entire CCD, with one half recording intra-focal images and the other half recording extra-focal images. The filter placed in front of the CCD is either 1.625 mm or 8.375 mm thick, corresponding to intra- and extra-focal, respectively [30].

The images from the GFA cameras are calibrated for read noise, dark current, and amplifier bias. This is done by using GFA data from the zeros, dark, arcs, and flats that are taken as part of the spectrograph calibrations. Zeros are many zero second exposures that are used to calibrate the bias of the overscan regions and to measure the read noise for each amplifier. The read noise comes from within the electronics during the read out process: from converting CCD charge to voltage as well as the processing and conversion from analog to digital units (ADU). Read noise is typically added uniformly to every pixel in the CCD.

The flat-field, or flats, are a series of exposures collecting uniform, or “flat” signal, with increasing exposure time for each exposure. The flats are used to measure the gain of each amplifier in the CCD. The amplifier gain is important as it allows us to convert from electrons to ADU, though to convert from ADU to electrons we use the inverse gain which is just 1/gain. Typical values for gain are around 4 ADU/electron, and the gains do not have to be equal across amplifiers. Different amplifier gains will cause the amplifier boundaries in the GFA images to be very prominent, as shown in figure 2.10a, with each amplifier a different shade of blue or purple.

The dark exposure is used to measure and then subtract the amount of current in the CCD before collecting any scientific data. This dark current is strongly correlated with the temperature of the CCD, where cooler CCDs will have less dark current. The dark current appears as a geometric “waffle” structure, shown in figure 2.10b, and the pattern will be more pronounced when there is a larger amount of dark current in the CCD. To measure the dark current, dark exposures are typically taken with the shutter closed. However, since the DESI GFAs do not have a shutter the same effect is achieved by keeping the Mayall dome closed and dark during dark exposures.

Calibration of GFAs during DESI Commissioning

Many calibration exposures were collected during commissioning of the DESI instrument. As part of the ETC calibration discussed in the next section (2.2.4), the GFA images needed to be calibrated as well. The set of calibration data used in figure 2.10 was taken in November 2020.

A raw GFA image taken on February 26, 2020 is shown in 2.10a. In this image, the amplifier boundaries are distinct and the overscan region on the outer edge of each amplifier is easily identified. The stars in this image are barely visible due to the un-calibrated amplifier gain.

To calibrate this image, the first step is to use the zero and flat-field exposures to calibrate the read noise and gain for each amplifier. This step also removes the overscan regions. The average amplifier read noise for this data set and GFA camera is 4.93 ADU and the average gain is 3.73 ADU/electron. Figure 2.10b shows the calibrated image using these values. In this image we can no longer easily identify the amplifier boundaries

The next step is to calibrate and subtract the dark current from the image. The dark current appears as the geometric "waffle" pattern in figure 2.10b. The dark current is measured as a function of temperature. For this set of calibration data and this GFA camera, the dark current was measured as 37.8 elec/s + 18.1%/C at 11.0 C. This is then subtracted from the image to create the final, fully calibrated GFA image, shown in figure 2.10c.

This calibration procedure is applied to all images taken on every GFA camera during the course of an exposure. This includes guide and focus images, as well as the acquisition image used to calculate the seeing, transparency, and fraction of light that is collected by a fiber.

2.2.4 Exposure Time Calculator

DESI utilizes a tool called the Exposure Time Calculator (ETC) to track and estimate the signal to noise ratio (SNR) accumulated by the spectrographs during an exposure. This is done using data from 20 fibers along the edge of the focal plane and the data from the 6 guide GFA cameras. The data from the fibers is read out every few minutes, while the data from the GFA cameras is read out every 10 seconds.

Once the desired SNR is reached, the ETC sends a signal to the instrument control system (ICS) to close the spectrograph shutter and the system moves on to the next tile in the queue. If the maximum exposure time is reached before the SNR, the stop signal is still sent but a second exposure on the same tile is then started.

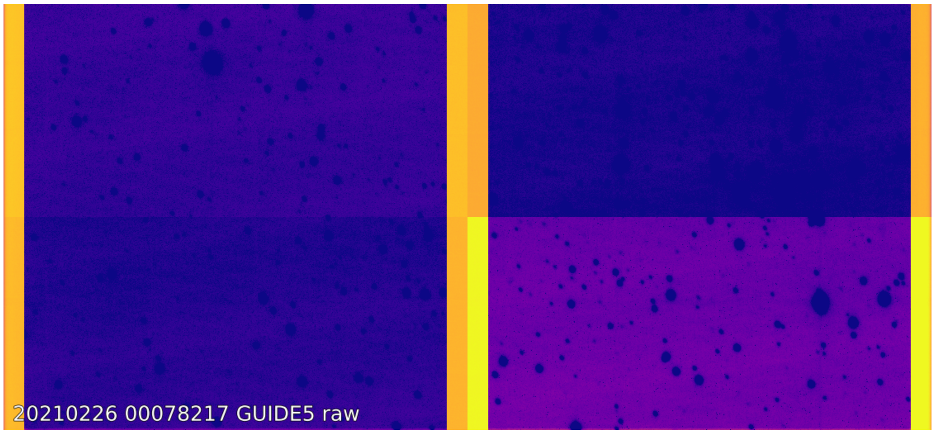

(a) Raw GFA image from a guide camera taken in February 2021. The overscan and different amplifier regions are clearly visible.

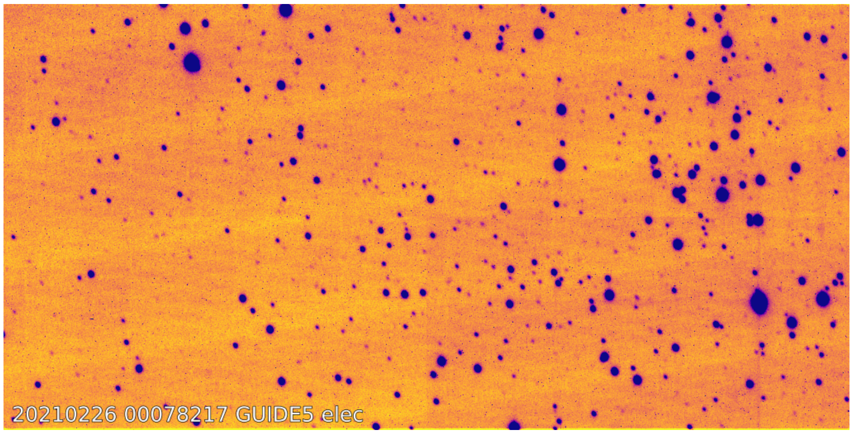

(b) The same GFA image after the overscan regions are removed, and the amplifier read noise and gains have been calibrated.

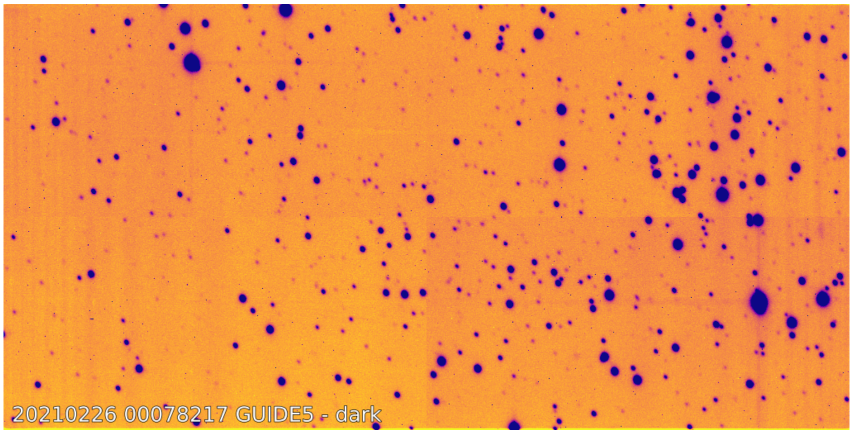

(c) The same GFA image after the dark current has been calibrated. This is the final image after all calibrations have been applied.

Figure 2.10: An example of the calibration steps for one GFA image for one guide camera taken in February 2021. The images show the raw GFA image in (a), the zero and flat-field calibrated GFA image in (b), and the final dark calibrated GFA image in (c).

Figure 2.11: Examples of ETC images showing the difference in observing conditions for two exposures taken on March 15, 2020. The left image shows a star in the GFA camera with 0.99″ seeing and 65% fiber fraction. The right image shows a star with 1.60″ seeing and 36% fiber fraction.

The ETC measurement of the SNR depends on the seeing, transparency, and fiber fraction. The seeing measures how stable the atmosphere is. For the Mayall, typical seeing values are on the order of 1.17 arcseconds [38] for r-band images. The ETC measurement of the transparency tells us how clear the atmosphere is. For example, on a clear night the transparency will be high, but on a cloudy night it will be low. The values of transparency can vary within a single exposure. The fiber fraction is the fraction of light collected by a DESI fiber and is correlated with the seeing and transparency. Lower seeing values and higher transparency values correspond to better observing conditions and higher fiber fraction values, as they mean that the PSFs of the observed objects are distorted less by the atmosphere. An example of this is shown in figure 2.11.

The ETC estimates the SNR in a single wavelength bin during time Δt with:

$$\nu^2 \equiv \frac{(\text{signal})^2}{(\text{noise})^2} = \frac{(D \cdot E \cdot T \cdot A \cdot f \cdot \Delta t)^2}{N^2 + T \cdot s \cdot \Delta t}. \tag{2.1}$$

Here, D accounts for the dust extinction, E for atmospheric extinction, T for the instrument throughput, A for the fraction of light collected by a fiber, N for the instrument read noise, s for the sky brightness, and f is the source flux. All quantities are wavelength dependent and N and T are also camera dependent [73].

The ETC updates the algorithm in equation 2.1 to estimate the SNR^2:

$$\nu^2_{\mathrm{ETC}} \equiv \sum_{\lambda} \frac{(D \cdot \tau E^0 \cdot T \cdot aA^0 \cdot \Delta t)^2 \langle (f - \tilde{f})^2 \rangle}{N^2 + T \cdot \Delta t \cdot rs^0}, \tag{2.2}$$

where τ is the transparency of the atmosphere measured by the ETC, E^0 is a nominal atmospheric extinction model, a is the fiber fraction measured by the ETC, A^0 is a nominal fiber fraction, r is the sky level measured by the ETC, and s^0 is a nominal sky brightness model. $\tilde{f}$ is the source spectrum, f, smoothed by a 100 Å median filter. The ETC measures the quantities τ, r, and a, while the quantities D, T, and N are fixed during the exposure.

Image Quality/ETC Calibration

It is very important that the ETC measures correctly the values for seeing, transparency, and fiber fraction, as those values are used to determine the exposure time for observations. During the Survey Validation (SV) phase of DESI, the ETC was run "offline", i.e, not as a part of the exposure pipeline. During this time, many tests and calibrations were performed using the data provided by the ETC. The first step was to confirm that the values for seeing were consistent with what was found in [38] and another unpublished offline GFA pipeline.

During the two nights of SV0 (the first part of SV), March 14th and 15th, 2020, the ETC was used in "offline mode" to measure the seeing, shown in figure 2.12. Conditions were highly variable on the first night, as shown in figure 2.13, but the median seeing across both nights was 1.1 arcseconds. The measured transparency and fiber fraction values for each guide GFA camera for the two nights are shown in figure 2.13.

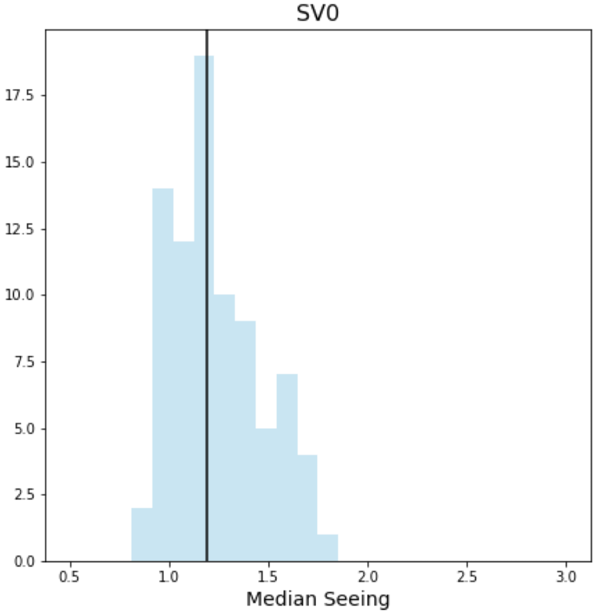

Figure 2.12: Seeing measurements for exposures during the two nights of SV0. The solid black line is the median seeing for these two nights, and is around 1.2″.

2.3 The DESI Survey

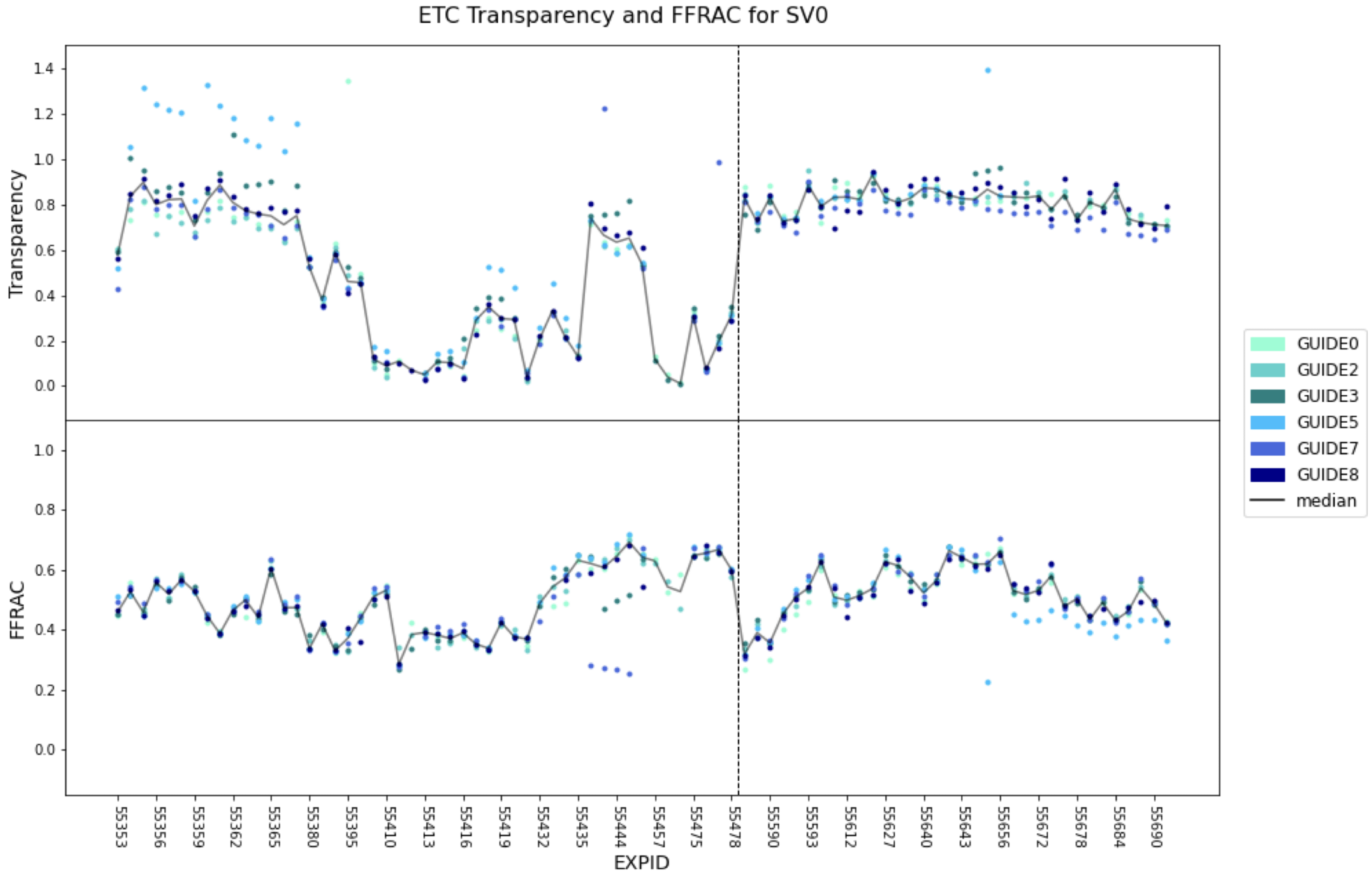

Figure 2.13: Transparency and fiber fraction (FFRAC) values calculated by the ETC during the two nights composing SV0 for each guide GFA camera. Conditions on the first night were highly variable but were much more stable on the second night. The dashed grey line separates the two nights.

Chapter 3

Testing and Mitigation of the DESI Linear Phi Positioners

The Dark Energy Spectroscopic Instrument (DESI) [36, 37, 76] will use redshifts collected throughout the 5 year survey from 40 million extragalactic sources to study the effects of dark energy on the expansion of the universe. DESI is the first of its kind to use robotic fiber positioners instead of pre-drilled metal plates like its predecessor, the Sloan Digital Sky Survey (SDSS) [104, 107] (see figure 2.2). These robotic positioners allow for completed positionings of new tiles within minutes.

The DESI focal plane consists of 5,020 robotic fiber positioners [30, 101] that can move individually to align fibers and collect light from distant objects. The fibers are grouped into 10 petals each containing 502 fibers, shown in figure 2.1. The outer edge of each petal also has one guide-focus-alignment (GFA) CCD camera and two fibers that reserved for measuring the sky background level. There are 123 stationary fiducials throughout the focal plane that are used with the Fiber View Camera (FVC) to measure the locations of each fiber.

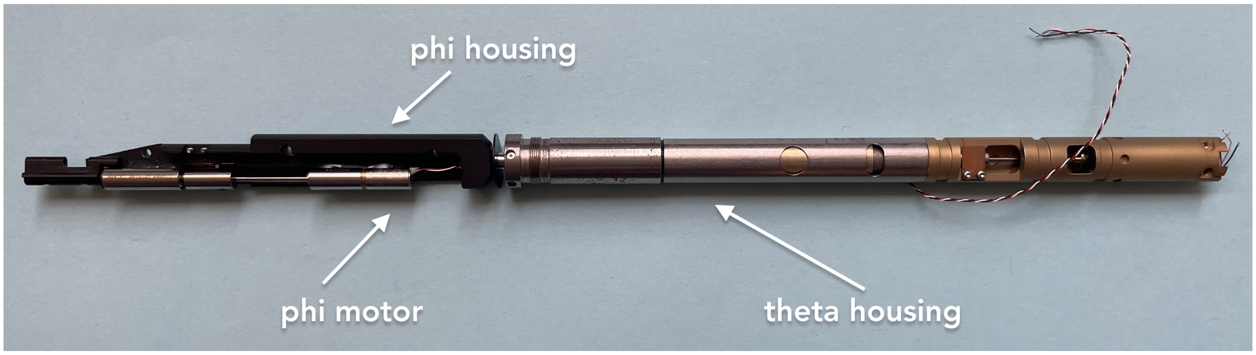

Figure 3.1: The same figure as figure 2.3 showing the body of a positioner.

The DESI positioners are described in detail in section 2.2.1 and in [101], but I briefly describe the positioners in section 3.1.

3.1 The DESI Linear Phi Problem

The DESI positioners gear-based robots with two rotational axes, theta (θ) and phi (ϕ). The theta axis rotates about its center, while the phi axis is offset and rotates about that point, each with a nominal radius of 3 mm. Each axis has a motor that can operate at two speeds: "cruise" and "creep". For the cruise speed, the motor rotates at 9900 RPM, and 150 RPM for the creep speed. The motors need to accelerate before reaching the cruise speed and decelerate before stopping, referred to as the ramp-up and ramp-down. At 9900 RPM, the total ramp is 3.99 degrees at the output shaft (with a gear ratio of $\approx 1/337$ and an output rotational speed of ≈ 180 deg s^{-1}). A DESI positioner is shown in figure 3.1.

The typical DESI move sequence consists of a blind move followed by a correction move. The blind move is usually a larger move ($\geq$ total ramp) done at the cruise speed, while the correction move is usually a smaller move ($<$ total ramp) done at the creep speed. As shown in figure 2.6, the DESI robots achieved an average positioning error of 50 μm in the blind move and 6 μm in the correction move for positionings between May 14th, 2021 and April 9th, 2024.

The positioner motors have around 2 degrees of internal backlash in the gears [101]. This can be seen in the CT image of a positioner in figure 3.2, where the teeth of the gears are not completely flush with each other. We correct for this by performing a 3 degree creep move after each cruise move, in the same direction as the cruise move [101].

While the majority of the positioners behave perfectly, a large fraction of the positioners are disabled due to poor behavior during prior move sequences. These positioners consistently do not move the requested amount, and because they do not arrive at their expected locations, sometimes cause collisions with neighboring positioners. Approximately 12% of the positioners are disabled due to this behavior, corresponding to approximately 600 positioners. We call these positioners either *linear phi* or *linear theta* positioners, depending on which axis is affected. Of the disabled positioners, roughly half are linear phi and half are linear theta. This chapter focuses solely on the testing and mitigation of the linear phi positioners.

We classify a positioner as a linear phi positioner based on it's scale factor, s: the ratio of the actual measured move to the requested target move. A perfect robot will have $s = 1.0$, while a linear phi positioner will have $s < 1.0$. An example of this is shown in figure 3.4, where the scale factor is just the slope of line that is fit to the points. In the left panel is an example of a good positioner, M05496, where the moves for phi (orange points) lie perfectly along the grey line with s (slope) = 1.0. The same positioner is shown in the right panel, although now the moves for phi lie along a line with a slope of ≈ 0.7. M05496 transitioned to a linear phi positioner after the first move of the night, as shown in the right panel of figure 3.4, where only one point has a scale factor of 1.

The exact cause for a positioner to become a linear phi positioner is believed to come from the motors. CT scans of linear phi positioners showed a cracked pinion gear within the motors, shown in figure 3.2. The pinion gear connects the motor shaft to the planetary gears inside the gearbox, which controls the output speed of the fiber tip. When the pinion

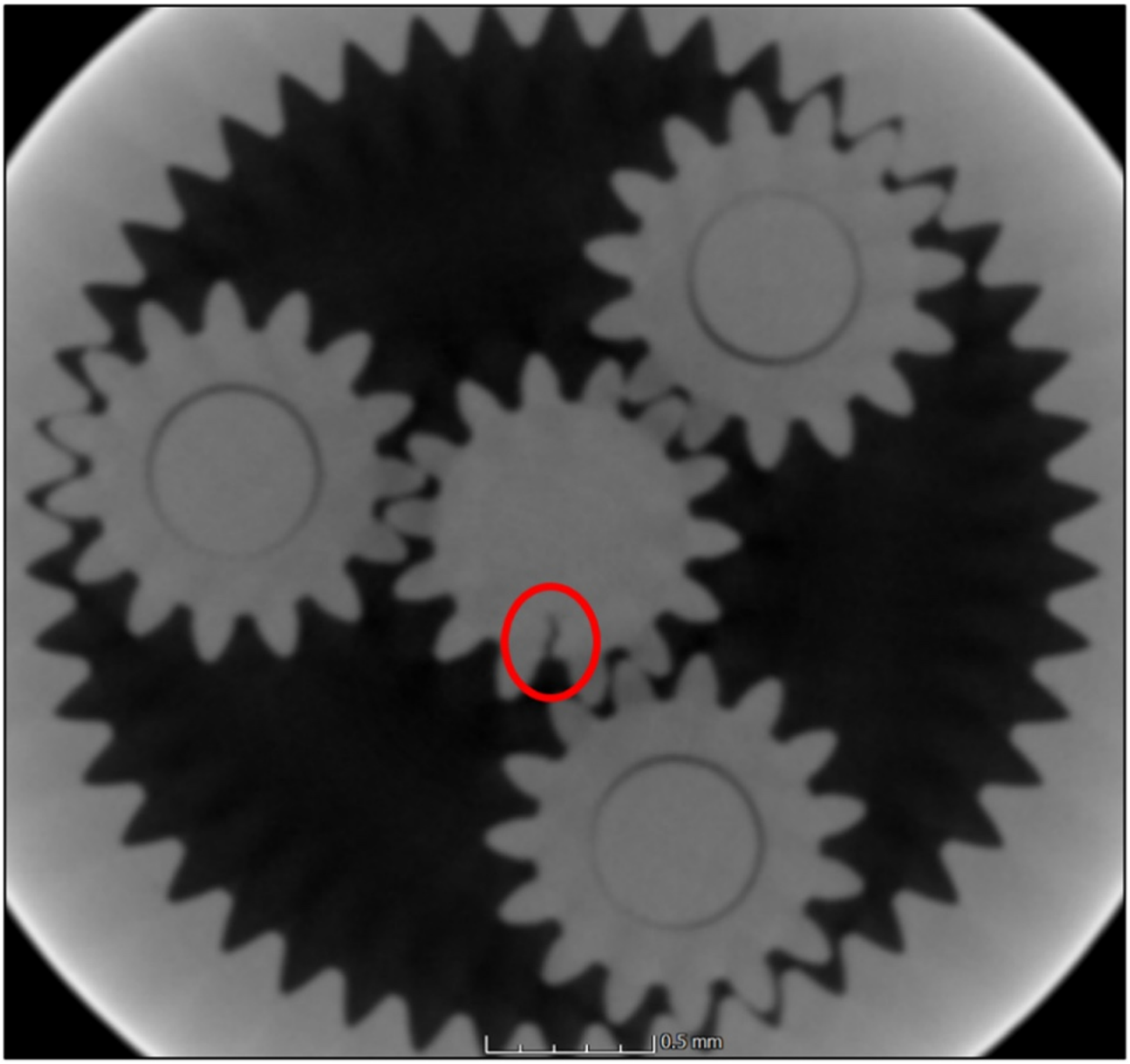

Figure 3.2: CT scan of a linear phi positioner, showing the crack in the pinion gear. This image also shows how the gears do not sit perfectly flush with each other, leading to approximately 2 degrees of backlash.

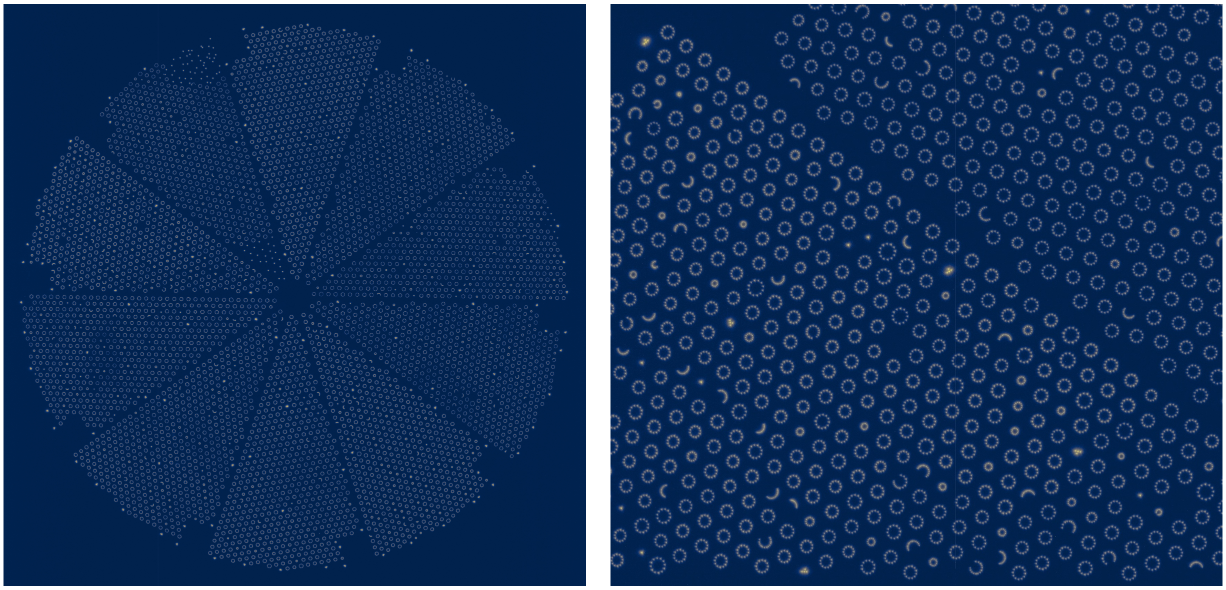

Figure 3.3: Positioner tests run in June of 2021 on all positioners. The left image shows the full focal plane and the right image shows a portion of petals 6 and 7. Positioners with arcs indicate linear theta and positioners with smaller, but still complete, circles indicate linear phi. Dots indicate positioners that did not move during these tests.

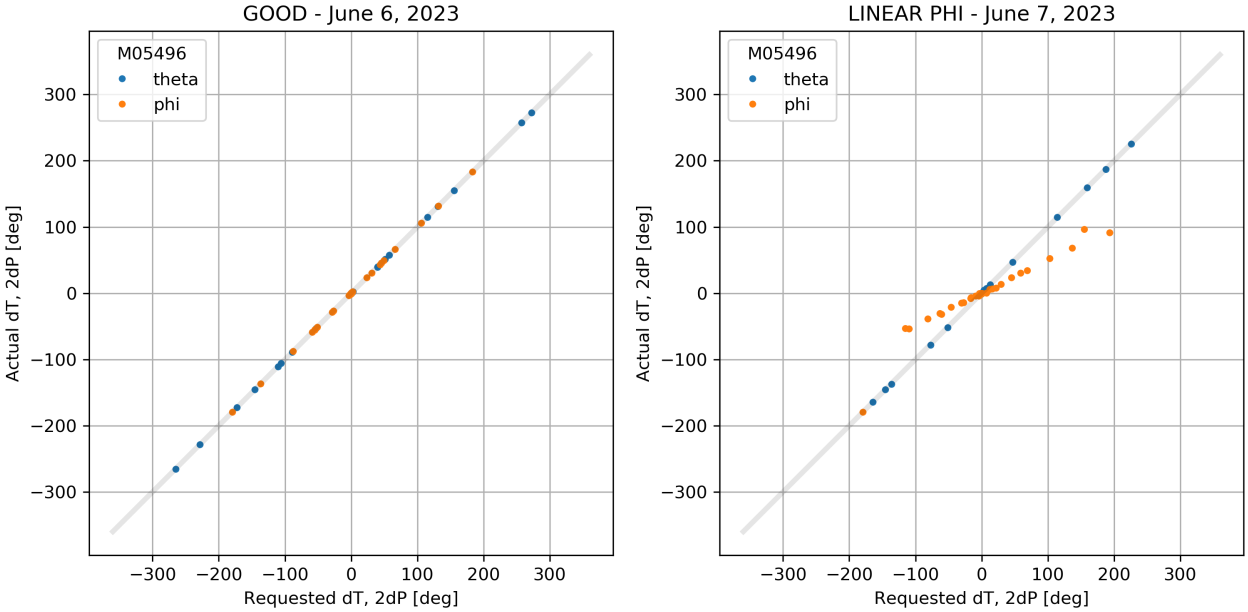

Figure 3.4: Move data for a positioner, M05496 when it transitioned to a linear phi positioner. Both panels show the requested move vs the actual move, and the scale factor is defined as the slope of the line between these points. For phi (orange points), all moves have been scaled by a factor of two for visual purposes. The left panel shows move data for M05496 before it was a linear phi positioner on June 6th, 2023. The right panel shows the move data for M05496 on June 7th, 2023. M05496 transitioned to a linear phi positioner with a scale factor (slope) of about 0.7 after the first move of the night.

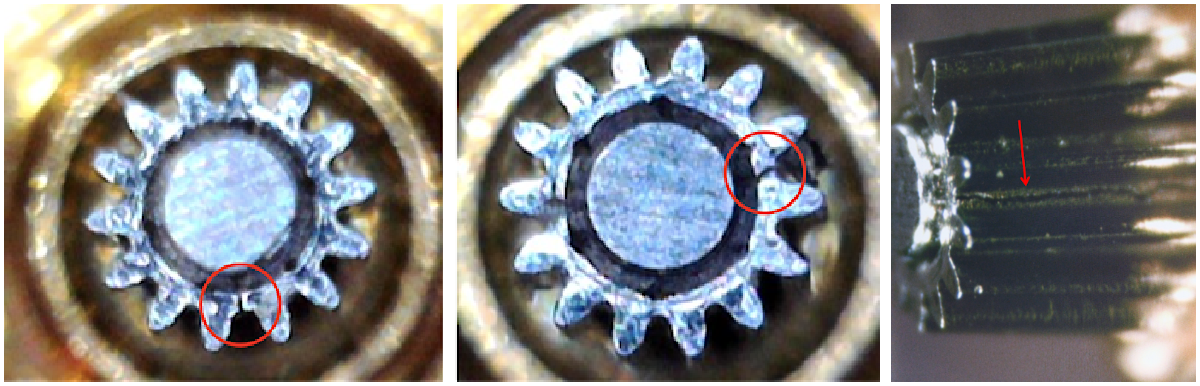

Figure 3.5: An example of a cracked pinion gear on the motor shaft. The two left images show examples of cracked pinions, circled in red. The right image shows a different view of the cracked pinion (red arrow pointing toward the crack) and how the gear has started to slip axially down the motor shaft.

gear cracks, the gear then slips down the motor shaft, losing contact and friction. Once the pinion gear slips far enough down the motor shaft and enough friction is lost, the positioners become linear phi positioners. Some positioners have shown the ability to "recover" when inverted (this causes the gear to slip down the shaft back into place), however it is impossible to invert the focal plane so other recovery methods must be pursued.

There are many variables that could cause the pinion gears to crack, however the main component appears to be time. The rate at which a positioner becomes a linear phi positioner is appears to be constant at roughly one per week, as shown in figure 3.6, which shows the number of linear phi and theta positioners since the start of the main survey in May of 2021. There are gaps when no new linear positioners were found corresponding to planned and unplanned (due to wildfires and instrument malfunctions) instrument shutdowns highlighted by the purple shaded areas. However, when the instrument was brought back online, there were new linear positioners corresponding to the number of weeks the instrument was offline.

In this chapter we discuss the testing and mitigation of the DESI linear phi positioners. In section 3.2 we discuss the sample of linear phi positioners available and the test stand used for testing. In sections 3.3 and 3.4 we discuss the tests run using different cruise and creep speeds. In section 3.5 we discuss a replacement for the creep move. In section 3.6 we

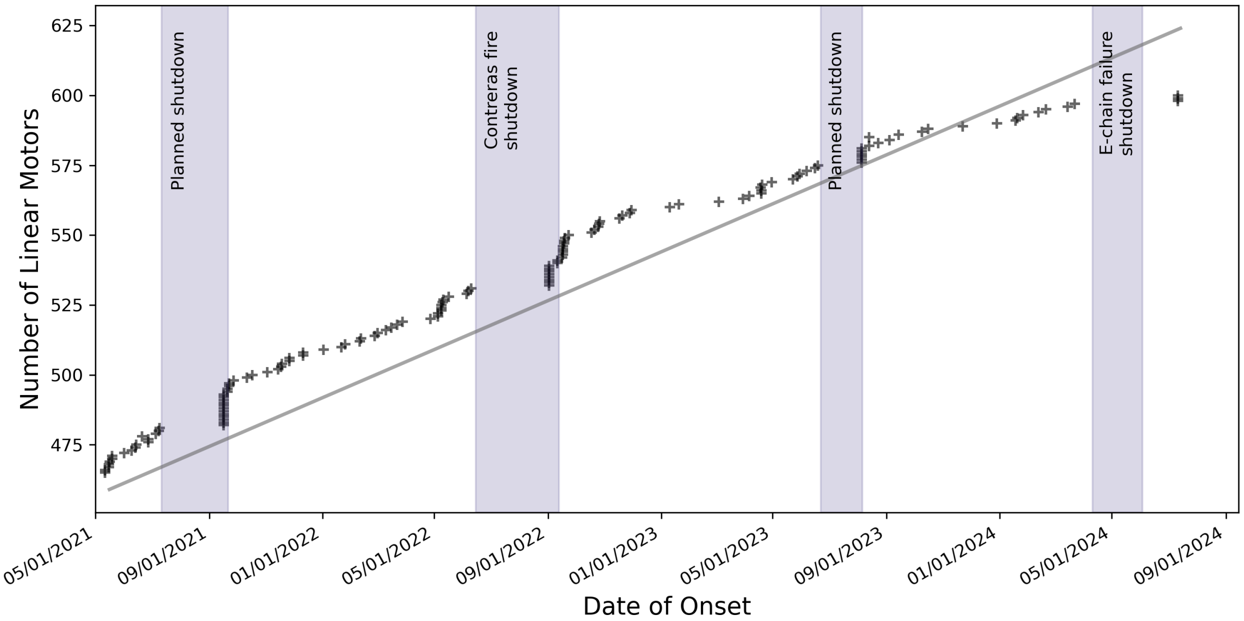

Figure 3.6: Rate of onset of linear phi and linear theta positioners since the start of the main survey in May of 2021. At this time there were already approximately 460 linear motor positioners. As of July 25th, 2024 there are approximately 600 total linear motor positioners on the focal plane. The shaded areas correspond to planned and unplanned instrument shutdowns.

discuss the recovery of the linear phi positioners, including necessary code changes and tests at LBNL and KPNO. Finally, we conclude in section 3.7

3.2 Positioner Sample

During the summer of 2021 the instrument was shut down to replace and install new electronics and remove 18 positioners that were identified as linear phi or linear theta positioners. These positioners are listed in table 3.1 along with the petal they were removed from and their measured scale factor at the time of removal. These are scale factors measured at the default cruise speed of 9900 RPM.

As part of the DOE Office of Science Graduate Student Research (SCGSR)[1] program, I

---

[1] `https://science.osti.gov/wdts/scgsr`

POSID	Affected Motor	Scale Factor	Petal ID	Phi Behavior at LBNL
M01722	PHI	0.20	4	Normal
M02725	PHI	0.79	4	Normal
M03236	THETA	0.26	7	Normal
M03556	THETA	0.53	7	Normal
M03567	THETA	0.33	7	Unknown
M03648	PHI	0.49	7	Linear
M03709	PHI	0.43	4	No movement
M03824	PHI	0.86	7	Linear
M03912	PHI	0.47	7	Linear
M03918	PHI	0.67	7	Linear
M03996	PHI	0.50	4	Linear
M04024	PHI	0.65	7	Linear
M04182	PHI	0.67	4	Linear
M05743	PHI	0.63	6	Unknown
M06848	THETA	0.42	5	Normal
M06891	THETA	0.88	5	Normal
M06931	THETA	0.42	5	Normal
M07550	THETA	0.55	5	No movement

Table 3.1: 18 linear phi and theta positioners were removed from the DESI focal plane during the summer 2021 shutdown. Listed here are their positioner IDs (POSID), which motor was affected and its corresponding scale factor, and which DESI petal they were removed from. We also list the behavior from the PHI arm that was observed at LBNL.

tested these positioners at Lawrence Berkeley National Laboratory (LBNL). Of the 11 linear phi listed in table 3.1, 7 displayed linear phi behavior, 2 displayed normal behavior, 2 had no movement in the phi arm, and 2 were unknown as they were not available to test in the lab. Of the 7 confirmed linear phi positioners, M04024 was placed on the LBNL test petal (sec 3.2.2), M03912 was sent to the University of Michigan to be used in their test stand, leaving the remaining 5 to be tested at LBNL.

3.2.1 LBNL Test Stand

The LBNL test stand was built to test the positioners removed from DESI and is shown in figure 3.7. The test stand consists of many components. First, there are blocks that hold the positioners in place, with their fibers pointing down. A digital camera is used to capture

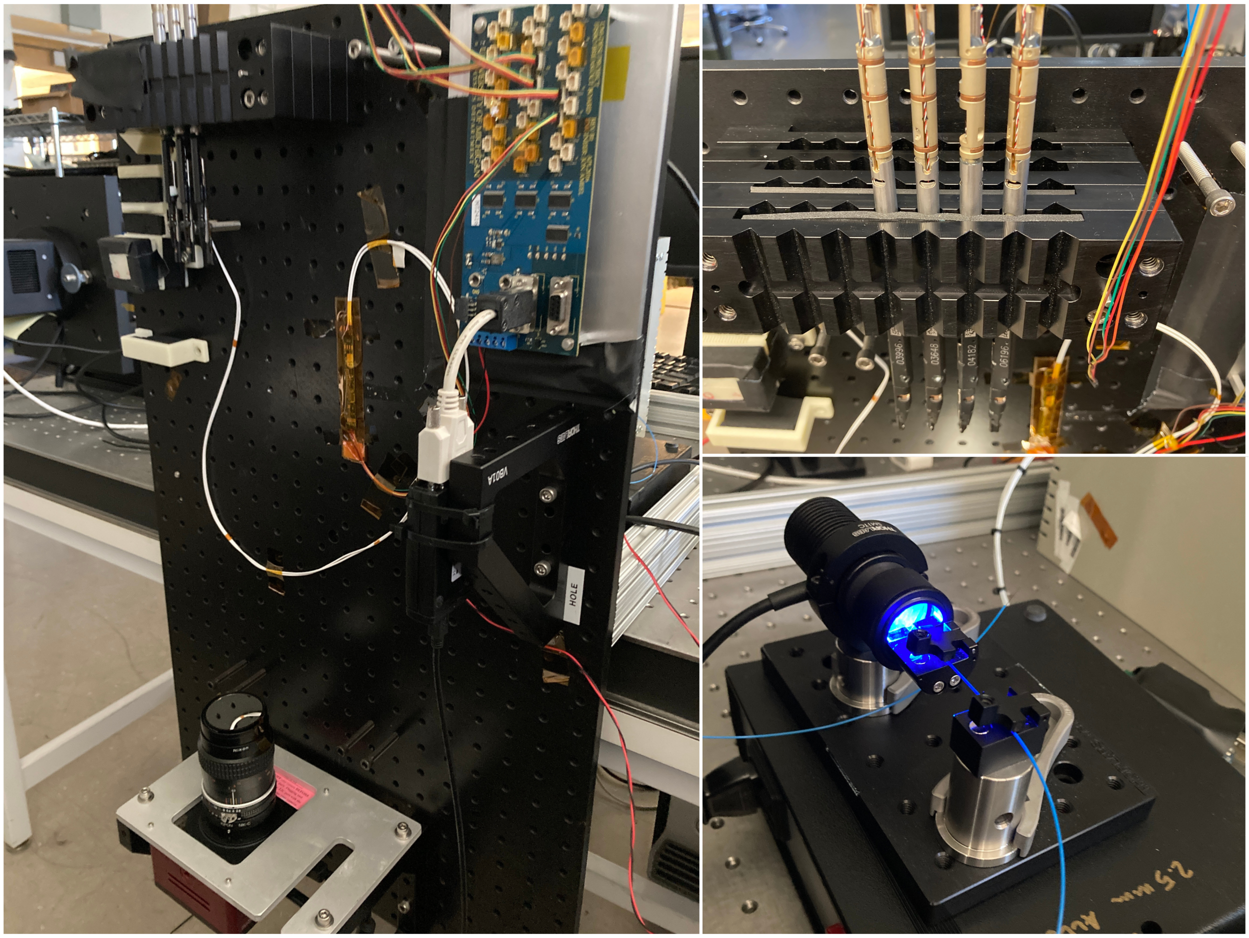

Figure 3.7: The LBNL test stand used to test the linear phi positioners that were removed from DESI. The left panel shows the full test stand, a few positioners mounted in the bracket, the digital camera (with filter), and the electronics (CanBus and fipos board) used to communicate with the positioners. The upper right panel shows a close up view of four positioners mounted in the bracket, with the fiber tips facing down toward the digital camera. The lower right panel shows how one fiber is back-lit with a blue LED.

the movement of the fibers. To communicate with the positioners we use a fipos board along with a CanBus and some python code. The CanBus and digital camera are connected to a laptop via USB, and the python code interfaces with all elements. The positioners have fibers installed and are back-lit with a blue LED. A filter is applied to the digital camera lens to filter out any stray light from room and the nearby windows. All tests are performed with back-lit fibers. Images are taken between each move and coordinates are measured from spots in the images. Positioners must be calibrated before the tests to set a reference point for calculations.

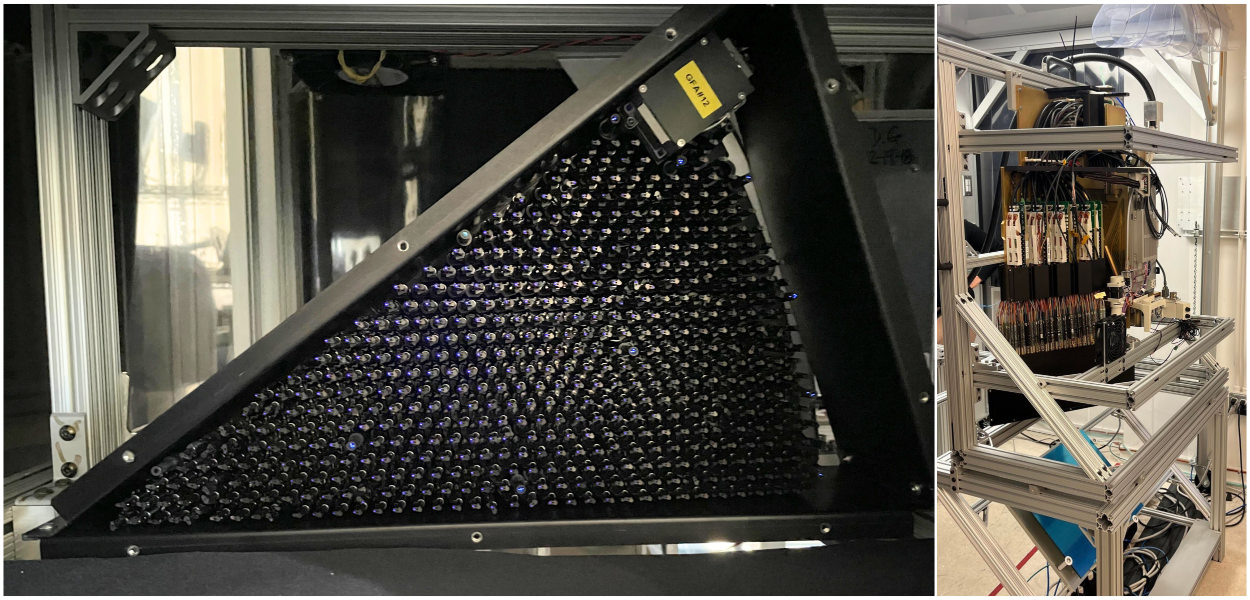

Figure 3.8: One of two spare test petals at LBNL, petal0. These petals are identical to those installed on DESI, except they do not contain a GFA camera. The left panel shows the face of the petal with the fibers back-lit. The right panel shows the petal and petal electronics after it was flipped into the vertical position. The mirror is partially blocked by the mounting bracket, but can be seen at the bottom of the image.

3.2.2 petal0

During the construction of DESI, two extra petals were built and are used as spare test petals at LBNL. These test petals, named petal0 and petal1, are identical to each other and the petals installed on DESI at Kitt Peak, although they do not have a GFA camera installed. Given the size of the lab at LBNL, the two petals are placed horizontally in order to create the largest possible distance from the FVC camera, which is approximately twenty feet from the petal surface. In June of 2023, the decision was made to mount petal0 in a vertical position such that the fiber tips were pointing down, to match the configuration of the focal plane at Kitt Peak. The FVC was left in the same position, and a mirror was added to reflect the light from the back-lit fibers. This is shown in the right panel of figure 3.8. The left panel of figure 3.8 shows the face of the petal.

Since some positioners can recover when inverted, we expected that some positioners on petal0 would have an onset of linear phi or linear theta behavior when flipped to the vertical position. These positioners could have been linear phi positioners prior to the flip, however this behavior would go undetected since petal0 was only ever in the horizontal position.

Prior to the flip, a short move test was run to get a baseline status for the petal. No positioners were flagged as having a scale factor < 1.0. We ran the same test after the flip, and found that six positioners had problems with the theta motor: three were linear and three were no longer moving. After running tens of thousands of more moves, we found four more linear theta positioners, two more theta positioners that did not move, and four linear phi positioners. This count does not include the linear phi positioner from Kitt Peak that was added to the petal in 2022. One additional linear phi positioner was found during the tests on petal0 discussed in section 3.6, bringing the total to six. These positioners are M01825, M02139, M04024, M06504, M07770, and M08069.

3.3 Cruise Move Tests

At the default cruise speed of 9900 RPM, the five confirmed linear phi positioners available for testing had scale factors ranging from 0.4 to 0.9, as given in table 3.1. This is consistent with the positioners on the focal plane, where the linear phi scales range from 0.2 to 0.9 for the disabled positioners.

Since a positioner likely becomes a linear phi positioner when the cracked pinion gear slips just enough down the motor shaft, we decided to study the behavior of these positioners at various motor speeds. It's possible that by changing the motor speed we can increase the amount of friction between the pinion gear and the gearbox, thus changing the behavior of the linear phi positioners. We test various speeds with different motor RPM and total ramp combinations as given in table 3.2.

Speed Name	Motor RPM	Ramp-up/Ramp-down	Total Ramp
default	9900	1.995/1.995	3.99
speed_5	19800	0.655/0.655	1.31
speed_6	6600	0.075/0.075	0.15
speed_8	29700	1.467/1.467	2.934
speed_10	40500	2.721/2.721	5.442
speed_11	50100	4.158/4.158	8.316
speed_12	34800	2.012/2.012	4.024
speed_14	25200	1.058/1.058	2.116
speed_100	30000	1.497/1.497	2.994
speed_66_2_3 (speed_9)	19800	1.311/1.966	3.277
speed_82_2_2	24600	2.017/2.017	4.034
speed_82_1_3	24600	1.009/3.026	4.035
speed_82_3_1	24600	3.026/1.009	4.035
speed_82_2_3	24600	2.017/3.026	5.043
speed_82_3_2	24600	3.026/2.017	5.043
speed_82_3_3	24600	3.026/3.026	6.052
speed_82_1_2	24600	1.009/2.017	3.026
speed_82_2_1	24600	2.017/1.009	3.026
speed_82_1_1	24600	1.009/1.009	2.018

Table 3.2: Speed parameters for the various speeds tested during move tests at LBL and at Kitt Peak. The first column gives the speed name. The second column gives the motor RPM (at the cruise speed). The third column gives the ramp up and ramp down angles in degrees (the amount a motor must turn through before accelerating/decelerating to/from the cruise RPM), and the final column gives the total ramp angle in degrees. The first set of speeds were tested during the cruise moves tests at LBL. The second set were tested at Kitt Peak. The third set of speeds were used to perform the ramp angle tests.

The parameter space for these speeds is large, so speeds both slower and faster than the default speed were chosen for these initial tests. The goal was to see if any speed caused better behavior and performance from the linear phi positioners.

Our first test used the first group of speeds in table 3.2. We command angles of 15 to 165 degrees in 15 degree increments in both the clockwise (CW) and counter-clockwise (CCW) directions. This is performed at least twice per speed. We then calculate measured angles and plot the average, as shown in figure 3.9 for positioner M03824. We estimate the scale factors by fitting a line to each set of points.

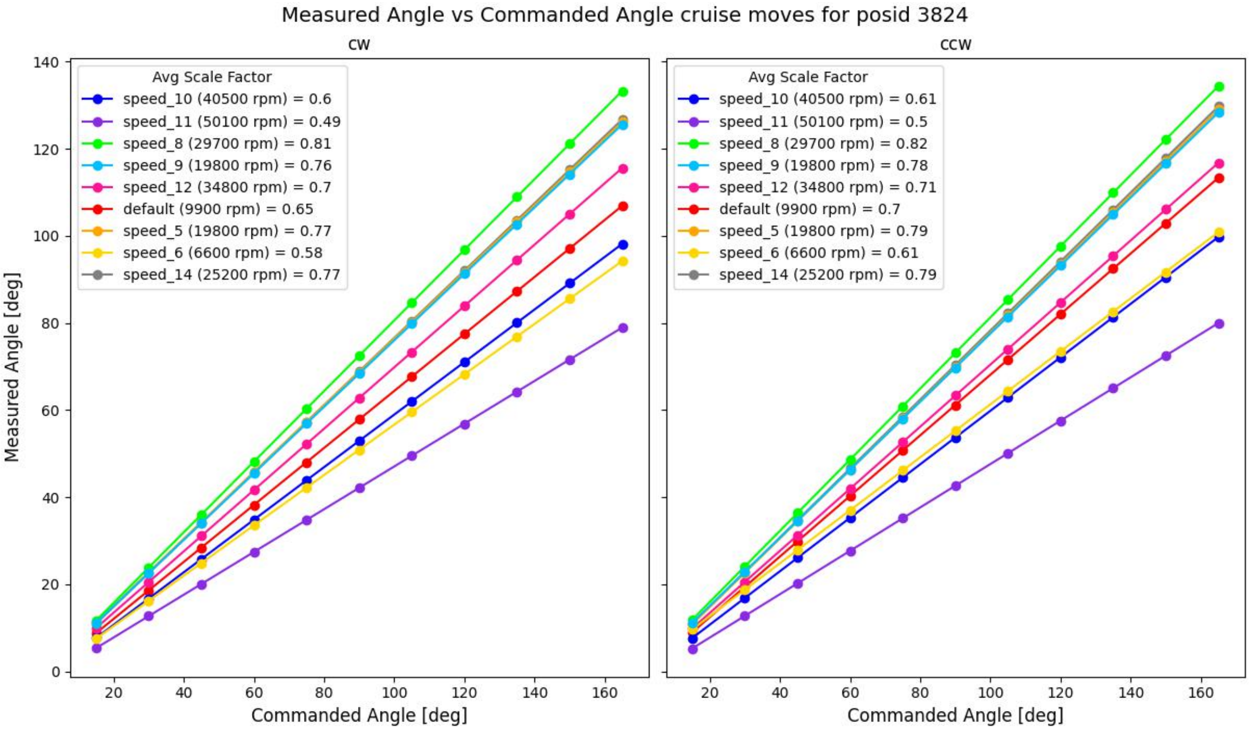

Figure 3.9: Measured vs requested angles for the first set of cruise move tests on positioner M03824. The left panel shows moves in the clockwise (CW) direction and the right panel shows moves in the counter-clockwise direction (CCW). The scale factor is measured by fitting a line to each set of points and is given for each direction in the legend for the corresponding speed.

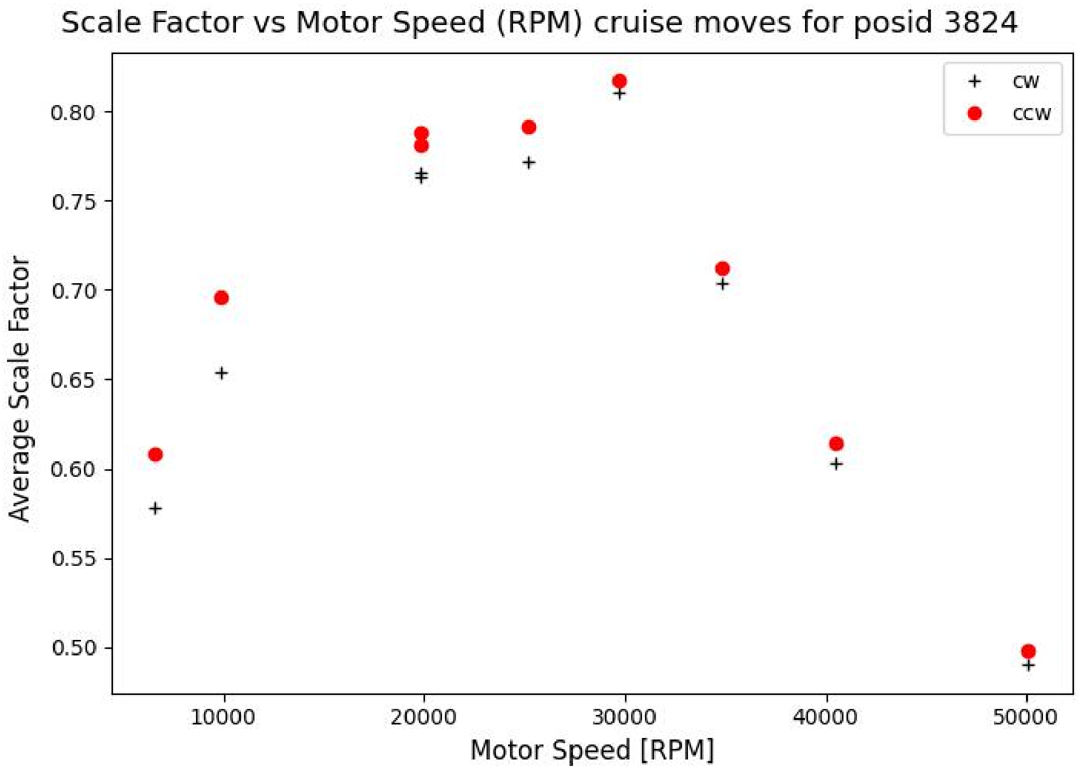

Figure 3.10: Average measured scale factor versus motor speed for the speeds tested during the first set of cruise move tests for positioner M03824. The scale factors for clockwise moves are shown as red points and black pluses for count-clockwise moves. The scale factors follow a quadratic pattern, with the highest measured scale factor corresponding to a motor speed of 30,000 RPM.

The scale factors vary for the different speeds but are generally consistent between the CW and CCW directions. We plot the scale factors against the motor RPM in figure 3.10 for M03824. As shown, the scale factors follow a quadratic pattern, with the slowest and fastest motor speeds having the worst scale factors. The scale factor peaks around 30,000 RPM, and the scale factors in each direction become more similar as the RPM increases. This is due to the variance at the different speeds. We find that moves at slower speeds typically have more variance (i.e., scatter) than moves at higher speeds. We estimate the variance of each speed and plot it against the motor RPM in figure 3.11 for M03824.

All five linear phi positioners display similar behavior to M03824. When comparing the measured scale factor with the motor RPM, they all follow a quadratic pattern with peaks

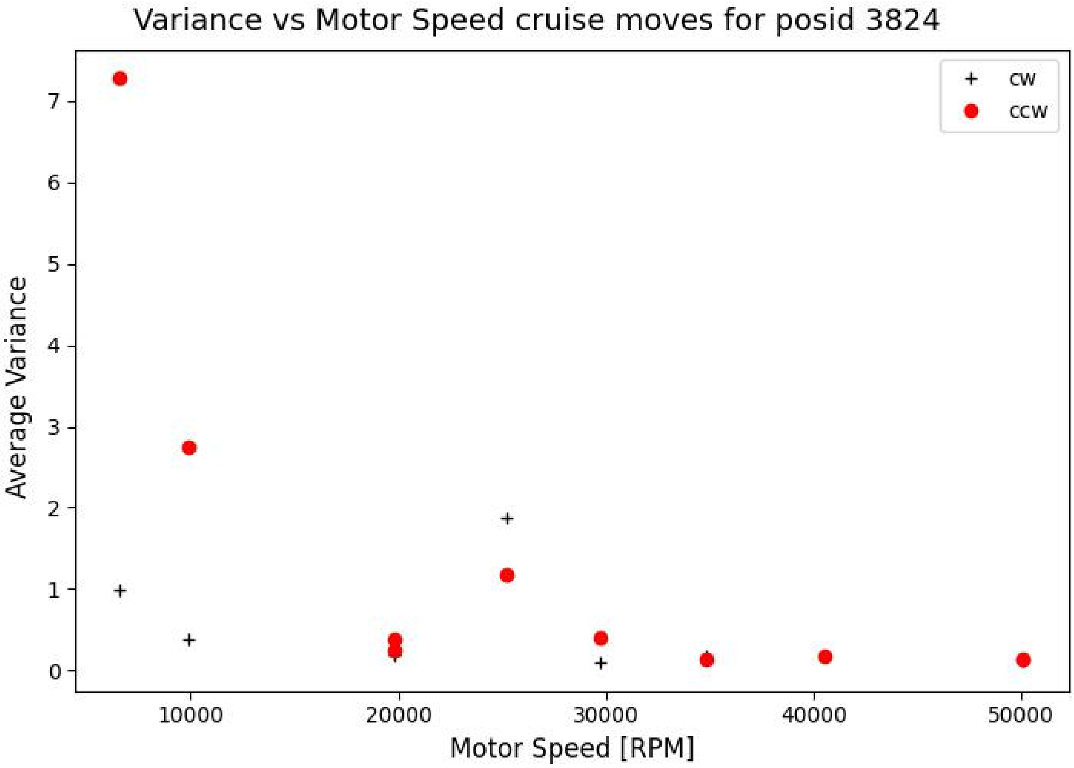

Figure 3.11: Average scale factor variance versus motor speed for the speeds tested during the first set of cruise move tests for positioner M03824. The variance for clockwise moves are shown as red points and black pluses for count-clockwise moves. The variance is larger for slower motor speeds, meaning the measured scale factors for moves at the same requested angle will vary more than moves at higher motor speeds.

around 30,000 RPM. The positioners also all follow the same general pattern for the variance: decreasing with increasing motor RPM. However the magnitude of the variance varies greatly between each positioner.

We want to run tests at a speed that will provide the highest scale factor with the lowest amount of variance, but not cause any further damage to the motors. For tests using the five linear phi robots on the LBNL test stand, we decided to use speed_12 from table 3.2. This speed has a motor RPM of 34,800, and a ramp-up/down of 2.012 degrees. Even though this speed does not have the highest scale factor, it was chosen because across the five available positioners it generally had the lowest variance. The scale factor is easily corrected for (as discussed in the "Fast Cruise" Tests section), however it is much harder to correct for the scatter when a positioner has a high variance.

Though this speed was chosen for tests on the test stand at LBNL, it is important to note that future tests done at KPNO and on the spare petal (discussed in sections 3.6.3 and 3.6.2) were performed using a different speed. This was due to growing concerns that the 34,800 RPM was potentially too fast for some motors, and could not be well tested given the small sample size available at LBNL.

3.3.1 Fast Cruise Tests

Now that an optimal speed was chosen we designed a test to randomly command a given number of angles between the total ramp angle and 165 degrees. The minimum commanded angle must be larger than the total ramp as we are not performing any creep moves in these tests, and commanding an angle less than the total ramp will cause calculation errors in the software.

At the beginning of the test, the phi arm starts at one of the mechanical hardstops. As angles are commanded, the test keeps track of the measured angles for each move. When the next angle is commanded, if the sum of that angle and the previous moves will cause the phi arm to hit the other hardstop, it is first moved back to its starting position and the angle sum is reset to 0. When directions are changed, before performing any moves the minimum angle is commanded to remove any gear backlash. The same random angles are commanded for each of the CW and CCW directions.

We run this test for three of the five positioners: M03824, M03648, and M03918. The results are shown in figure 3.12 as the blue points. Each positioner was run for a different number of moves, indicated in () in the legend. We fit a line to each set of points to estimate the scale factors, and the result is also indicated in the legend. The scale factors range from 0.68 to 0.72. These are the scale factors that are used when running scale factor corrected moves.

We run the test again and correct for the scale factor. To do this, we calculate new target angles to command given the scale factor:

$$\texttt{commanded angle} = \frac{\texttt{target angle}}{s} \tag{3.1}$$

Without a scale factor correction, the commanded angle is equal to the target angle. The results from the scale factor correction for three positioners are shown in figure 3.12 as the orange points. Again, the number of moves is indicated in () in the legend. When we fit a line to estimate the scale factors we find they range from 0.99 to 1.01. We plot the positioning error in microns in the third column for all scale factor corrected moves. We calculate the positioning error as

$$\texttt{error} = r\ (\texttt{target angle} - \texttt{measured angle}) = r\ \mathrm{d}\phi, \tag{3.2}$$

where r is the nominal radius of the phi arm (3 mm) and dϕ is the difference between the requested target angle and the actual measured angle, in radians. The calculation of the positioning error is especially sensitive to incorrect scale factors. This is most visible in figure 3.12 for positioner M03824, where there is a clear shift toward positive positioning errors. This indicates that the measured scale factor is close but not quite correct, and means that the measured angles are less than the requested target angles for this positioner.

To return linear phi positioners to operation at KPNO, we defined a grading scheme similar to Table 2 in [101], but with different requirements. For the blind (cruise) move, we require these positioners to have a positioning error $< |200|$ μm 95% of the time. These requirements are discussed more in depth in section 3.6. For the three positioners, M03824, M03648, and M03918, in figure 3.12, 96.8%, 98.9%, and 98.0% of scale factor corrected moves are within 200 μm for the positioners, respectively. Though not a requirement, it is also important that the maximum positioning error on the blind move be less than 250 μm as larger errors can cause collisions between neighboring positioners. This is not the case for any of these positioners, however, less than 1% of moves for the three positioners are outside this range. Based on just the fast cruise move alone, were these positioners still on the DESI focal plane they would be very strong candidates for recovery.

The 34,800 RPM speed at which these initial tests were run is not the speed that was chosen to run the positioners at KPNO. Only one of the positioners, M03824, was run at the KPNO operational speed of 30,000 RPM. We show those results in figure 3.13 for both uncorrected and scale factor corrected moves. The clockwise scale factor is over-correcting moves, as shown in the third panel where there is a large distribution of negative positioning errors. Due to this, only 94% of moves are within the 200 μm requirement, however 99.6% of moves are within 250 μm. It is likely that with an adjustment to the scale factor the positioning errors for this positioner would significantly improve in the clockwise direction.

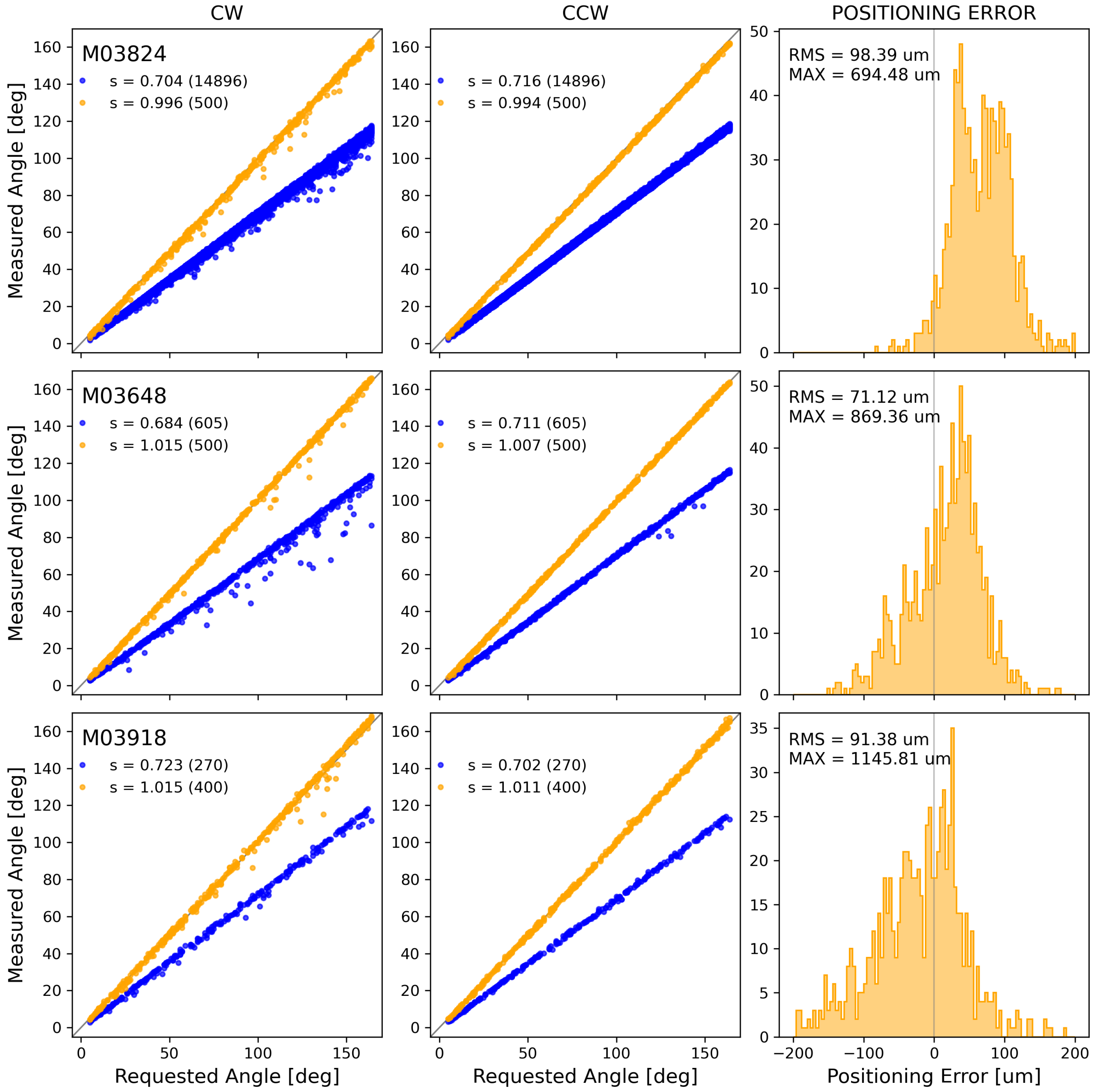

Figure 3.12: “Fast” cruise move tests for three linear phi positioners M03824 (top row), M03648 (middle row), and M03918 (bottom row) at speed_12 (34,800 RPM). We estimate the scale factor as the slope of the line of the uncorrected moves (blue points). We then use that scale factor as a correction factor for new moves (orange points). The left column shows the moves commanded in the clockwise (CW) direction and the middle column shows the moves commanded in the counter-clockwise direction (CCW). The right column shows the positioning error as the distance from the target angle in microns, where a positive error means the positioner did not move the full commanded angle.

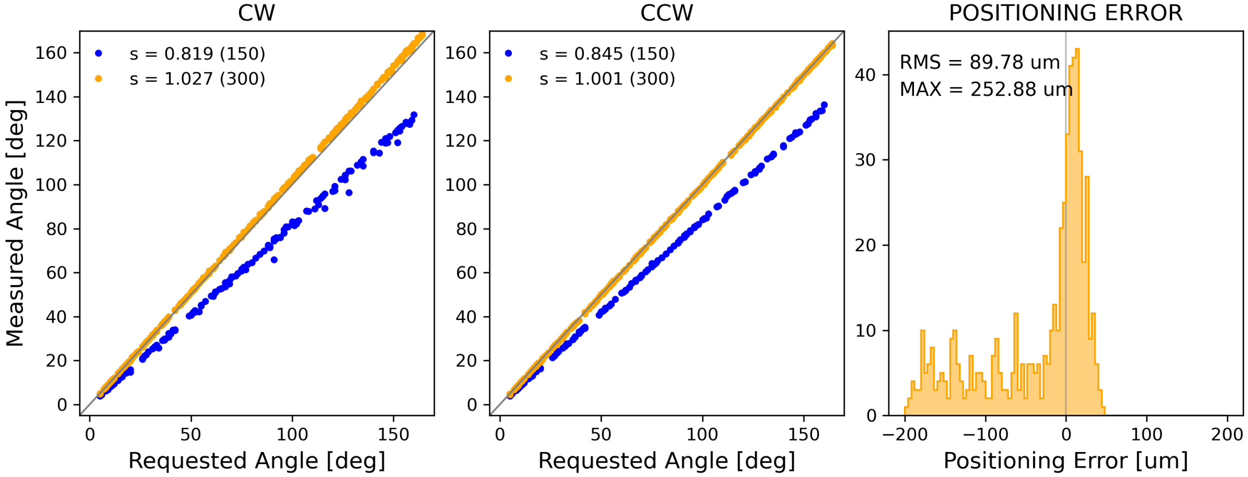

Figure 3.13: “Fast” cruise moves for positioner M03824 at the chosen operational speed of 30,000 RPM (speed_100). For this positioner the clockwise scale factor was overestimated, as shown in the positioning error where there is a large distribution of negative errors.

3.3.2 Lifetime Tests

As mentioned at the end of section 3.3, there were growing concerns that the 34,800 RPM motor speed was too fast for some of the motors, and that using this speed would degrade performance over time. We decided to simulate and test this theory on one positioner, M03824. On an average night, DESI observes anywhere from 20 to 50 different tiles, depending on observing conditions [96]. This means that, on average, there are roughly 30 move sequences in one night. Assuming that the telescope is in operation for 90% of the year, this translates to just under 10,000 move sequences in one year. For our lifetime tests, we decided to simulate three years worth of blind move sequences using the “fast” cruise move procedure described in the previous section. We commanded 30,000 moves to M03824, 15,000 in each of the clockwise and counter-clockwise directions.

Figure 3.14 shows the results from the lifetime test on positioner M03824. There is no apparent change in the scale factor in either of the clockwise (blue points) or counter-clockwise (red points) directions - it is constant around 0.7 throughout all 30,000 moves. There is also no change in the amount of scatter throughout these moves. There are a handful of points

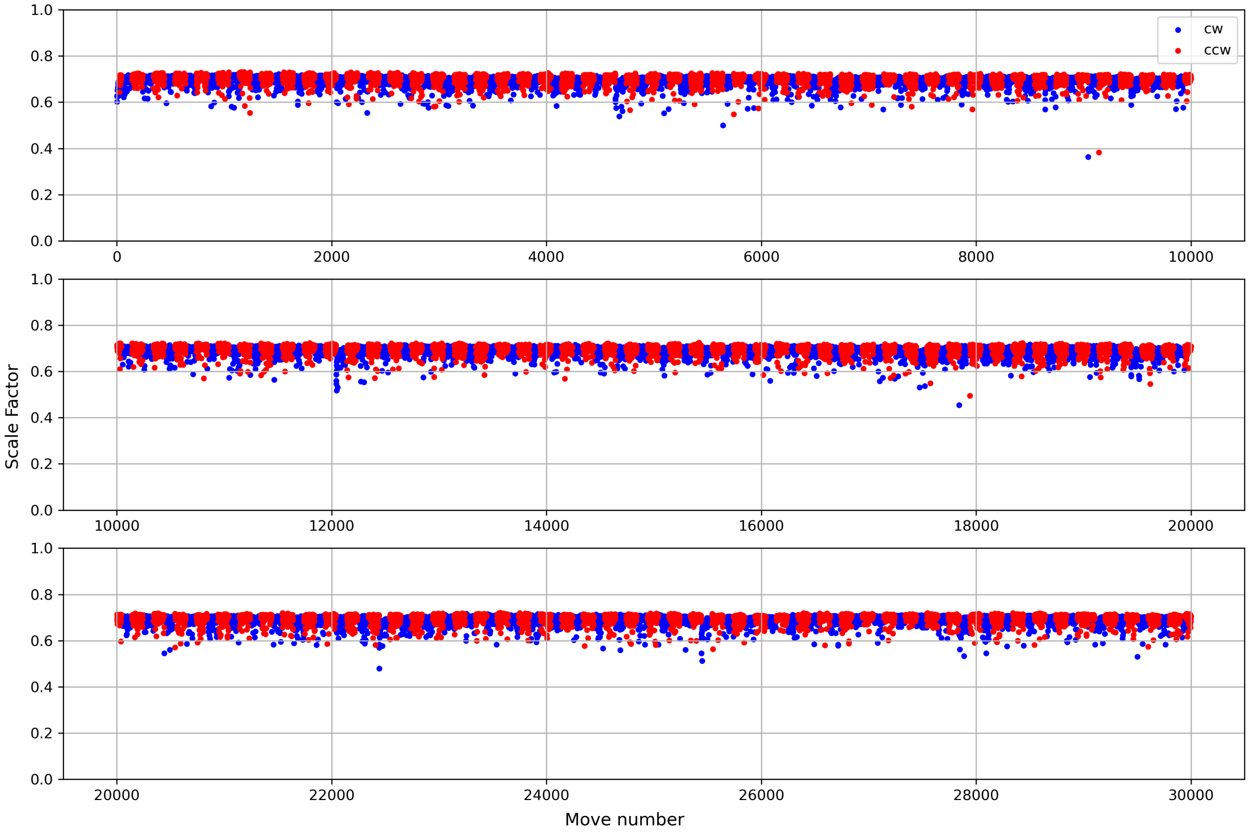

Figure 3.14: Lifetime test results for positioner M03824 with the 34,800 RPM motor speed. After roughly three years worth of simulated blind moves there is no apparent degradation in performance for this robot at this motor speed, as the measured scale factor for each move is constant.

that have scale factors of less than 0.5, however these are scattered throughout the moves and there does not appear to be any sort of trend.

Though the sample size is small, this indicates that operating these positioners at higher motor speeds does not cause any further damage or performance degradation.

3.3.3 Ramp Tests

The parameter space for choosing motor speeds is vast, and there are infinitely many combinations of motor acceleration, deceleration, and final cruise speed that can be tested. We decided to test if changing the acceleration and deceleration speed of the motors would change the performance. There were theories that by changing how fast the positioners accelerated and decelerated to and from the cruise speed, we could control how much scatter was seen in some of the previous fast move tests. At this time, there were three motor speeds being considered as the operational speed at KPNO: speed_66_2_3, speed_82_2_2, and speed_100, and the favored speed was speed_82_2_2 (24,600 RPM). The parameters of these speeds are described in table 3.2.

We tested four of the linear phi positioners, M03824, M03648, M03918, and M03996 using a top cruise speed of 24,600 RPM and varying the ramp up and ramp down parameters between 1, 2, and 3 degrees. The speeds are listed in the third group of table 3.2. We run the same sequence as described in section 3.3.1, but we randomize the order of the speeds for each positioner to eliminate any potential biases (i.e, if the first few moves are always worse). We show the results for each of the speeds and each of the positioners in figures check that order is correct: 3.32-3.40 in the appendix. Each set of plots shows the results at a different speed for the four linear phi positioners, with the speed indicated at the top. We show both the uncorrected and corrected moves in the clockwise and counter-clockwise directions as well as the positioning error for the corrected moves. We list the RMS of the

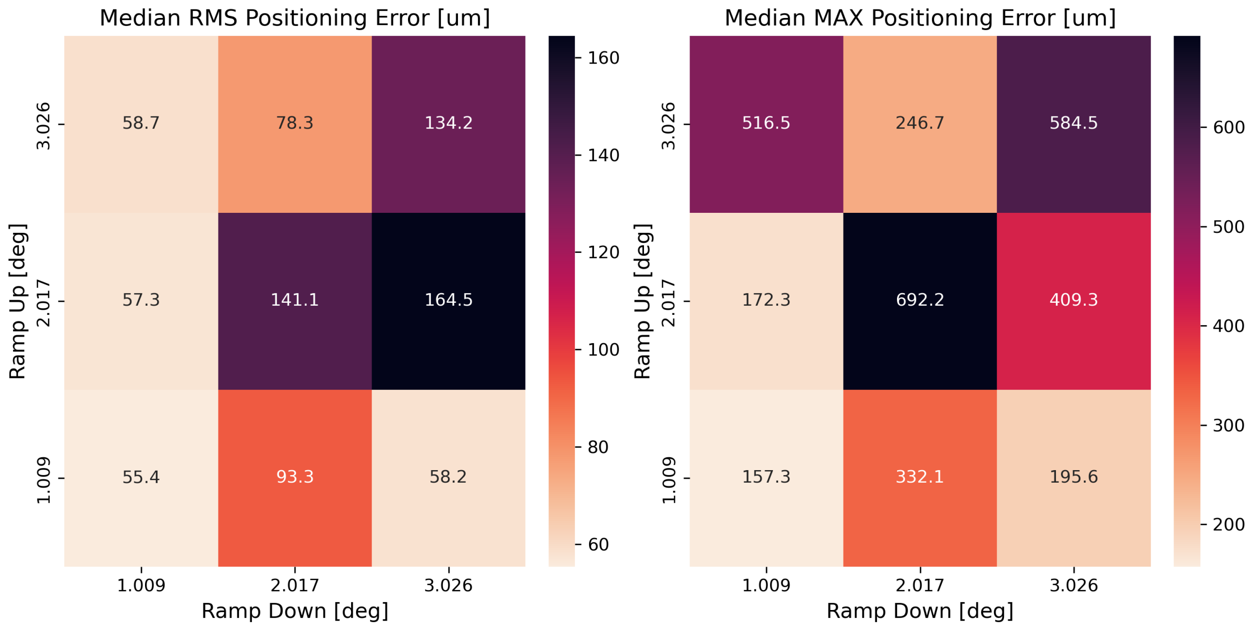

Figure 3.15: Statistics for the nine speeds tested during the ramp cruise tests. All speeds have the same motor RPM and the ramp up and down angles are indicated on the X and Y axes, respectively. The left plot shows the median RMS positioning error across the four linear phi positioners. The right plot shows the median maximum positioning error across the four positioners. These plots exclude outliers from catastrophic failures, likely due to the sun shining on the test stand during these tests.

positioning error and the maximum of the positioning error with each histogram.

During the scale factor corrected moves tests, some positioners had moves that moved very little or did not actually move, or appeared to move more than they were commanded. These catastrophic failures happens for M3996: speed_82_1_1 and speed_82_1_3, M03824: speed_82_2_3, and M03918: speed_82_3_1. The tests for these positioners and speeds occurred on various days in March of 2023 but all between the hours of 5 and 6:30 PM Pacific time. This is the time when the setting sun shines directly on the test stand lab room, and even though curtains and light blocking materials are on the window they are neither perfect nor light tight. It is likely that these failures occurred due to the setting sun interfering with the digital camera, causing the code to find the wrong spot in the image taken after each move. This means the code is no longer correctly keeping track of the position, and the fiber is likely stuck at the hard stop boundary.

Excluding the outliers mentioned above, we show the RMS and maximum positioning error in microns by taking the median value across the four robots in figure 3.15. The rows and columns indicate the different ramp up and ramp down angles given in table 3.2, with the right diagonal indicating where the ramp up and ramp down are equal. The left plot shows the RMS of the positioning error, where a lower number (lighter color) is better. There is no requirement for what the RMS should be, but historically an RMS of 100 μm or less is considered good. The three speeds (speed_82_2_2, speed_82_2_3, and speed_82_3_3) that have an RMS above 100 μm are likely due to a large amount of scatter in the scale corrected moves and scale factors that were over- or under-correcting (see figures 3.35, 3.37, and 3.38). The right plot shows the maximum of the positioning error, where again a lower number is better, however for the recovery discussed in section 3.6 there is a requirement that the 95% of the positioning error for the blind move be within 200 μm. While not a requirement, it is preferred that the maximum positioning error be $< 250\mu$m. There are four speeds that meet this requirement. There are five speeds that do not meet this requirement, likely due to the mis-estimation of scale factors and scatter within the scale corrected moves. With slight adjustments to the incorrect scale factors, it is possible that the positioning errors for these speeds would improve.

3.4 Creep Move Tests

In addition to testing a fast cruise move for the linear phi positioners we also tested different alternatives to the 150 RPM creep move. These alternatives included a fast creep move (i.e, a motor speed between 150 and 9900 RPM), and a fast creep move without any ramp-up or ramp down. Using the fast creep move with a ramp up and ramp down was difficult to study, as any target angles less than the total ramp would not be commanded properly.

We first tried to operate the linear phi positioners with a fast creep speed but with no ramp

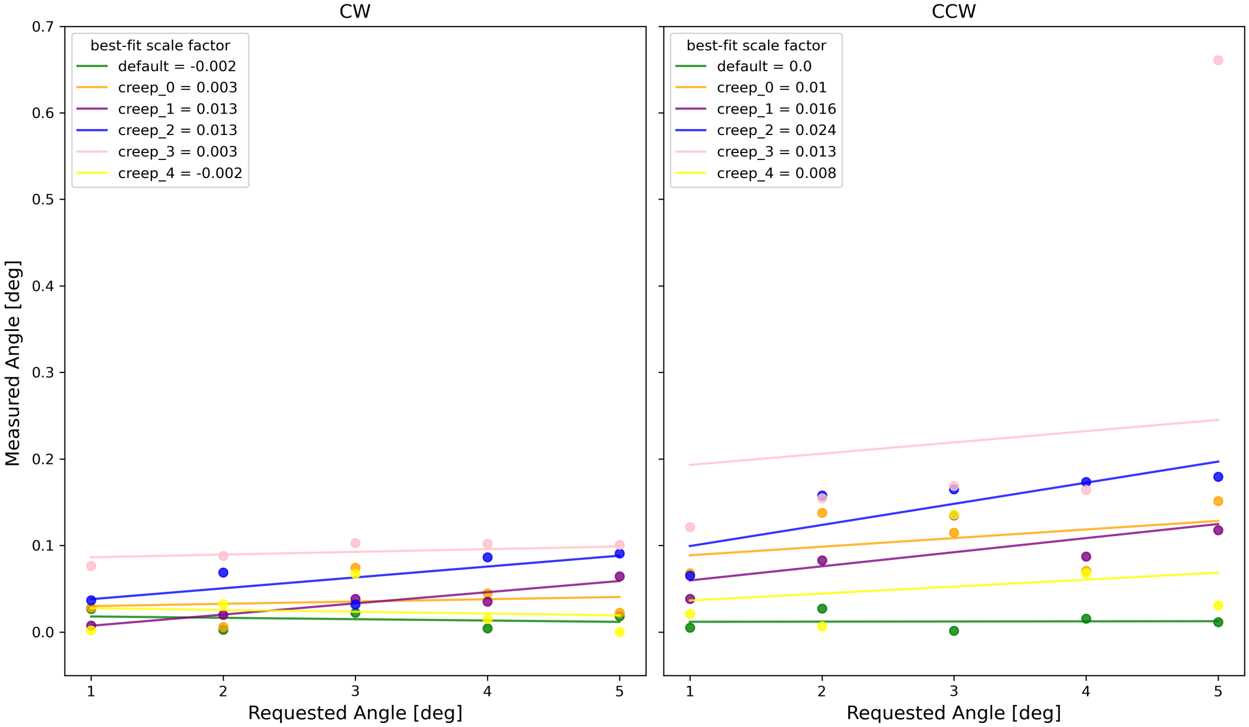

Figure 3.16: Results for testing a fast creep move with no ramp up or ramp down (i.e, immediately run at cruise speed). This strategy did not work and all measured scale factors were consistent with zero.

up or ramp down. This means that there was no acceleration period for the motors, and they were commanded to reach the top cruise speed immediately. The speeds tested are described in table 3.2. For this test, we created a move sequence and commanded small angles between 1 and 5 degrees. The results for one move sequence for each creep speed is shown in figure 3.16. We found that without any acceleration (ramp-up), the positioners did not move when commanded, and all measured scale factors were consistent with zero.

In a move sequence with a blind move and a correction move, we attempted to constantly undershoot the blind move by the commanding the target angle minus the total ramp angle to ensure that the correction move would have a large enough request. This proved difficult to achieve, especially if the scale factors were off, and the positioning errors were too large to consider this strategy.

3.5 New Move Algorithm

As discussed in section 3.3, we can reliably position linear phi positioners when performing a fast cruise move, however, we were unable to find a successful replacement strategy for the creep moves. As mentioned in section 3.4, using a fast cruise move in place of the creep move is not a stable alternative, as any target angles that are less than the total ramp angle for that speed will not be commanded properly. There are a few solutions to this problem and one example is to undershoot the first move in a move sequence such that the second move will be more than the total ramp angle away. This solution is impractical and having positioning errors so large on the first move could cause potential collisions.

Another solution is to split the second move into two sub-moves, however the two sub-moves are in opposite directions. The two sub-moves will be a combination of a *jog* move and a *jog + d* move, where d is the desired target angle. These moves will always have a scale factor correction applied. This algorithm is discussed in detail in [10] and depicted in figure 3.17. The rules of the algorithm are as follows:

1. There are two sub-moves
2. The first sub-move must always be opposite in sign to the previous move
3. No sub-move can be less than the jog in magnitude
4. The sum of the two sub-moves must equal, in magnitude and direction, the desired new move

There are four cases in which this algorithm will be used. There are two sets of two cases that are equal but opposite in direction. Each case is depicted in figure 3.17. The jog move is shown as the green arrow and the desired target move (jog + dP) is shown as the black arrow. The current and target positions are labeled to show directionality. We define a positive move as a counter-clockwise move (i.e., to the right in the figure).

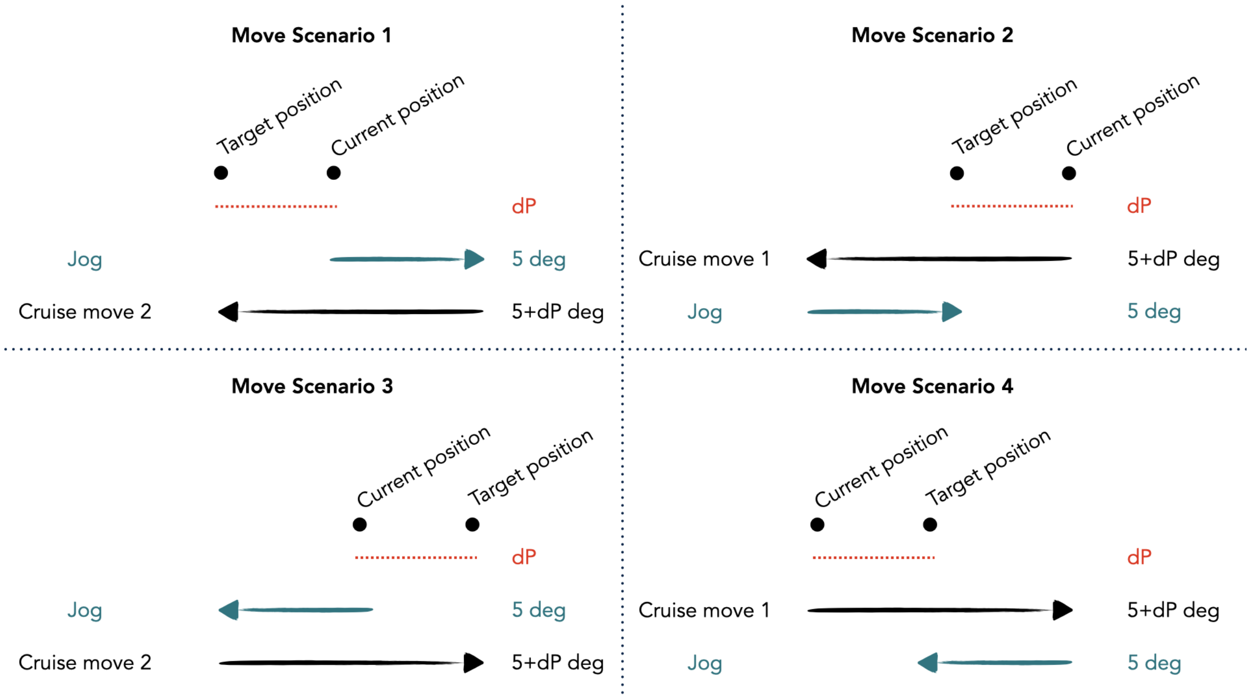

Figure 3.17: Different move scenarios when the back and forth move algorithm will be applied. Moves following scenarios 1 and 3 will occur when the previous move and the desired move are in the same direction. Moves following scenarios 2 and 4 will occur when the previous move and the desired move are in opposite directions.

There are two cases applicable if the previous move and the desired new move are in the same direction, as depicted by the left column of figure 3.17. In this case, the first move will move away from the target position by jog/s, and then back toward the target position by $(jog + dP)/s$, where jog is a move that is larger than the total ramp, d is the desired target move, and s is the scale factor for that direction.

The other two cases arise when the previous move and the desired new move are in opposite directions. This is shown in the right column of figure 3.17. In this case, the first move will move through and past the target position by $(jog + dP)/s$, and the second move will then move back toward the target position by jog/s.

This move algorithm was originally intended to replace only the creep move. However, there is a consequence of this sequence, in that we can not accurately account for the gear backlash within the motors. The gear backlash can introduce anywhere between 0.5 to 2 degrees of error in each move. It is simple to account for the backlash in the scale factor, but this introduces errors as only moves in the opposite direction as the previous move will encounter backlash, and any moves that do not encounter backlash will therefore be over-corrected.

To mitigate this, we decided that every move for a linear phi positioner would follow this move algorithm and be a combination of two sub-moves. This allows us to keep track of the backlash and account for it in the measured scale factors.

3.6 Recovery of Linear Phi Positioners

To start the recovery process at Kitt Peak, extensive testing needed to be completed first on petal0. There are two types of tests that were run on the linear phi positioners: arc tests and XY tests. Arc tests are run in only one axis, and each move is incremented in the same amount. XY tests create a grid of points that the positioner is then commanded to go to. Depending on the XY test, these points are in either uniform or random order. An example of the two XY tests is shown in figure 3.18. XY tests also allow for the inclusion of multiple correction moves, while arc tests only perform one move per target angle. For the linear phi positioners, each commanded move is the compound move discussed in section 3.5, while for non-linear phi positioners these moves are commanded as normal.

Though speed_100 was ultimately chosen as the recovery speed for the linear phi positioners, two other speeds were also tested: speed_66_2_3 and speed_82_2_2. The parameters for these speeds are given in table 3.2. To run these tests and include the compound move, the magnitude of the jog move needed to be decided. The value needed to be larger than the total ramp for whatever speed was being used and it also needed to be small enough to not

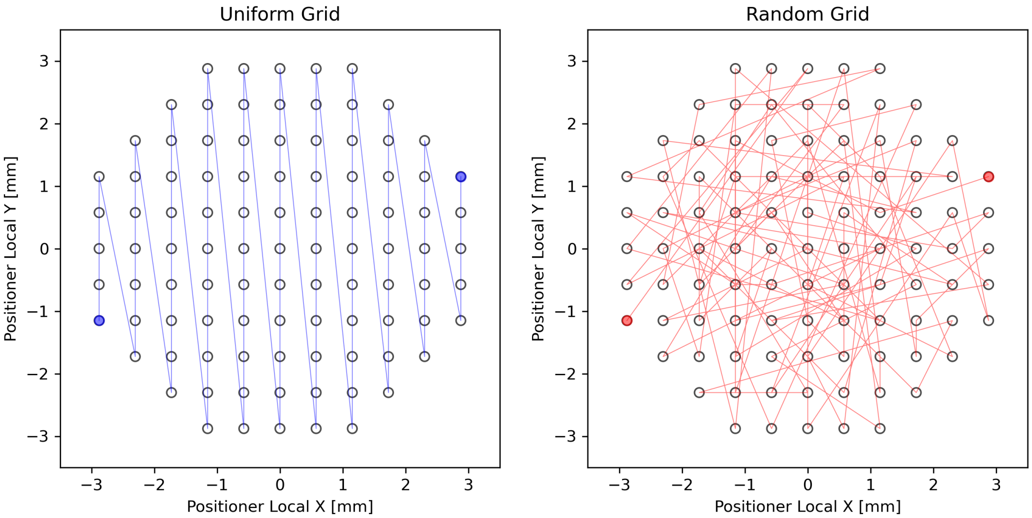

Figure 3.18: Uniform and random grid of points used in the XY tests. The start and end points are highlighted for each grid.

cause anti-collision to block the moves of neighboring positioners. The total ramp for the speeds being considered ranged from 2.99 to 4.03 degrees, which put a lower limit on the jog move. After discussion with the creator of the anti-collision software, we decided on a 5 degree jog move, as it would be sufficient for any speed we chose and would not cause any issues with neighboring positioners.

Measuring the scale factors for the linear phi positioners when the compound move is performed is not trivial. Without the compound move, the scale factor is the ratio of the actual move to the requested move. If we were to perform the same calculation on the compound move data, we would be calculating the *effective* scale factor, as the move is now a combination of two moves in either direction. Instead, we can calculate the true scale factor, S^t, as a function of the effective scale factor, s^e, with

$$\begin{aligned} S^t_{\text{ccw}} &= \frac{J\left(s^e_{\text{ccw}} - s^e_{\text{cw}}\right) + s^e_{\text{ccw}}P}{2J+P}, \\ S^t_{\text{cw}} &= \frac{J\left(s^e_{\text{ccw}} - s^e_{\text{cw}}\right) + s^e_{\text{cw}}P}{2J+P}, \end{aligned} \tag{3.3}$$

where J is the magnitude of the jog move, P is the requested target angle, and we define positive moves in the counter-clockwise direction. Regardless of which move scenario listed in figure 3.17 occurs, the equations for the scale factors all simplify down to those in equation 3.3. Unfortunately, these equations only work when calculating scale factors using arc test data, since they assume that you have a move request of P degrees in both the clockwise and counter-clockwise directions. This is not true in an XY test as the grid setup means there is not a move request of P degrees in both directions. Calibrating scale factors using arc tests is a potential option, but these equations do not allow us to confirm the scale factors using data from positioning sequences during DESI observations. This is because the positioning sequences are similar to an XY test and follow the *retract-rotate-extend* algorithm discussed in section 2.2.1.

To calculate scale factors for an XY test we instead model a linear phi motor's behavior with four parameters: S, the true average (of CW and CCW) scale, dS, the cruise-ramp offset, dC, the cruise CCW-CW offset, and dR, the ramp CCW-CW offset. We perform a χ^2 minimization on the four parameter model to find the best fit. We then calculate the true scale factors as

$$\begin{aligned} S^t_{\text{ccw}} &= S + dS + dC \\ S^t_{\text{cw}} &= S + dS - dC \end{aligned} \tag{3.4}$$

3.6.1 code changes

The software used to control the focal plane, called PetalController [101], is designed to handle communications with the positioners and fiducials. It receives move schedule tables from the Petal application, converts and then sends them via CAN messages to the positioners. The move commands are created by the Petal application. We describe here the changes made to this software to operate the linear phi positioners.

The linear phi positioners require the code to be modified to account for the jog moves, scale factors, and faster motor speed. The positioner calibrations database was updated to add columns to store flags and scale factors for linear phi positioners. If a positioner is flagged as a linear phi, the modified PetalController and Petal codes will be used, otherwise the code will work as normal. We test and validate all code changes on petal0 before deploying it to KPNO.

The PetalController software is responsible for applying the scale factors and setting the motor speed for the linear phi positioners. The parameters for the default cruise, default creep, and new linear phi motor speed are hard-coded into PetalController. Each speed has three parameters that describe the ramp up, the ramp down, and the cruise RPM. PetalController sends these parameters via CAN to the positioners on startup.

The move tables that PetalController sends to the positioners via CAN are also modified. This is where the scale factors are applied to the target angles. The modified move tables are printed in the log for debugging purposes, and include the scale factors and the target angles both before and after scaling. These move tables are also saved in the logs during regular operations.

The Petal application software is responsible for scheduling the moves and sending that information to PetalController. Petal reads the scale factors and a flag for whether a positioner is a linear phi from the database. If the positioner is a linear phi, Petal follows the new move algorithm discussed in section 3.5 and adds the jog move in the appropriate direction. Petal then sends the modified movedtable to PetalController along with the scale factors.

3.6.2 Arc Test Results

The first tests we ran on the linear phi positioners on petal0 and at KPNO were small angle arc tests. Small angles are more likely to occur during a correction move where positioning accuracy is very important. The small angle tests allow us to determine if we meet the required positioning accuracy for science data using the new move algorithm. We designed new arc tests with target angles of 0.5, 1.0, 2.0, and 4.0 degrees. Each arc test consisted of 80 total moves, where each move was a compound jog move following the algorithm in section 3.5.

Petal0

The code changes during these tests were not yet complete, and could not properly handle compound moves where the direction changed (i.e, a turnaround due to reaching a hardstop). To validate the code changes discussed in section 3.6.1, we picked four normal positioners on petal0 to run as "pretend" linear phi positioners to establish a baseline. Since we did not yet have a measurement of any scale factors, all positioners were run with scale factors set to 1.0.

The results for one linear phi and one normal positioner are shown in figure 3.19, which was a four degree arc test. The right column shows the results for the linear phi positioner. It is clear from these plots that no scale factors were applied. In the top and middle plots, this is seen where the blue and pink points do not lie along the solid grey line. These points also trend toward lower absolute phi values, indicating that the scale factors in either direction are not equal. The bottom right plot shows a histogram of the measured angle change in phi. If the scale factors were applied (and correct) the two histograms would be centered at four degrees. The left column shows the results for the normal positioner. It is clear in these plots that the positioner has a scale factor equal to one as the points follow the solid

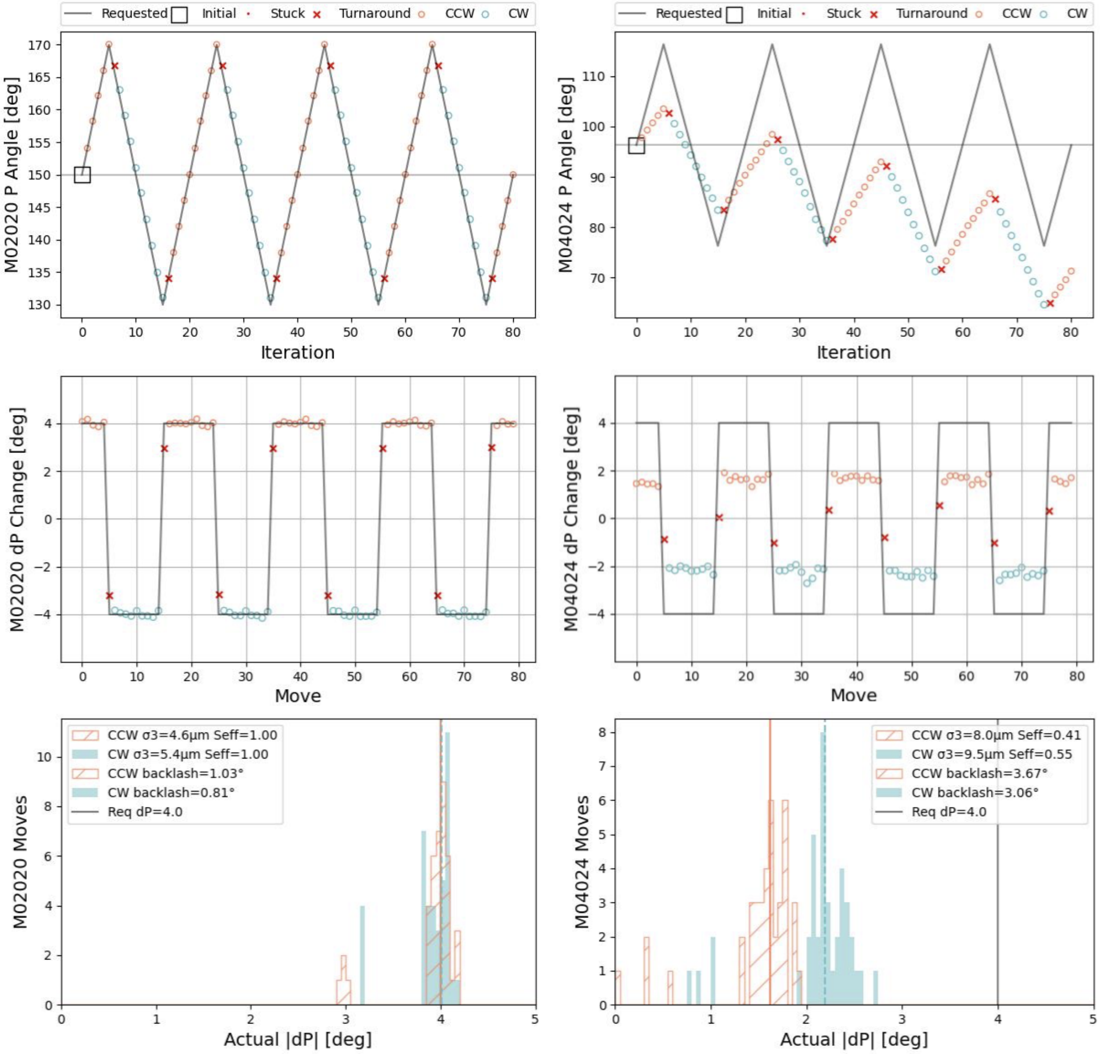

Figure 3.19: Results of an arc test performed at LBL for a pretend linear phi (left column) and a true linear phi (right column). The top row of plots shows the expected position in phi (grey line) and the actual position in phi for each direction (CW: blue, CCW: pink). The middle row of plots shows the requested change in phi (ΔP) angle (grey line) and the actual change in phi angle for each direction (CW: blue, CCW: pink). The bottom row shows the histogram of the actual ΔP angles for each direction (CW: blue, CCW: pink). The turnaround points (red X's) are where backlash is introduced and are excluded from calculations.

grey line and the histograms are centered at four degrees. There are a few points in the histogram that are centered around three degrees - these are the turnaround points that are excluded from the analysis.

KPNO

We ran the same small angle arc tests on all linear phi positioners at Kitt Peak. For these tests at Kitt Peak, we ran with three different speeds: speed_100, speed_82_2_2, and speed_66_2_3 (parameters in table 3.2). Linear theta positioners were used as the baseline for this test, as their behavior in phi was fine. There were a total of 627 positioners tested at this time, roughly half of which were confirmed linear phi positioners.

We ran multiple 0.5, 1, 2, and 4 degree arc tests at the three speeds, with a focus on speed_82_2_2 and speed_66_2_3. At the time, these speeds were assumed to have better performance, however speed_100 turned out to have the best performance. Since there were no scale factor corrections applied during these tests, we attempted to estimate the scales. This is harder to do with only small angle data, as the errors are much smaller than at larger angles. We show in figure 3.20 the estimated scale factors for the 627 positioners at speed_100. The peak of scale factor = 1.0 corresponds to the linear theta positioners which were used as a control sample. The range of scales measured is 0.4 to 0.9 with a peak around 0.7, which is consistent with what is seen in other tests.

3.6.3 XY Test Results

The next tests that we ran on petal0 and at KPNO were XY tests. XY tests are more similar than arc tests to positioning sequences during nightly observations. We run each XY test with one correction move to accurately reflect the positioning sequence at KPNO. The

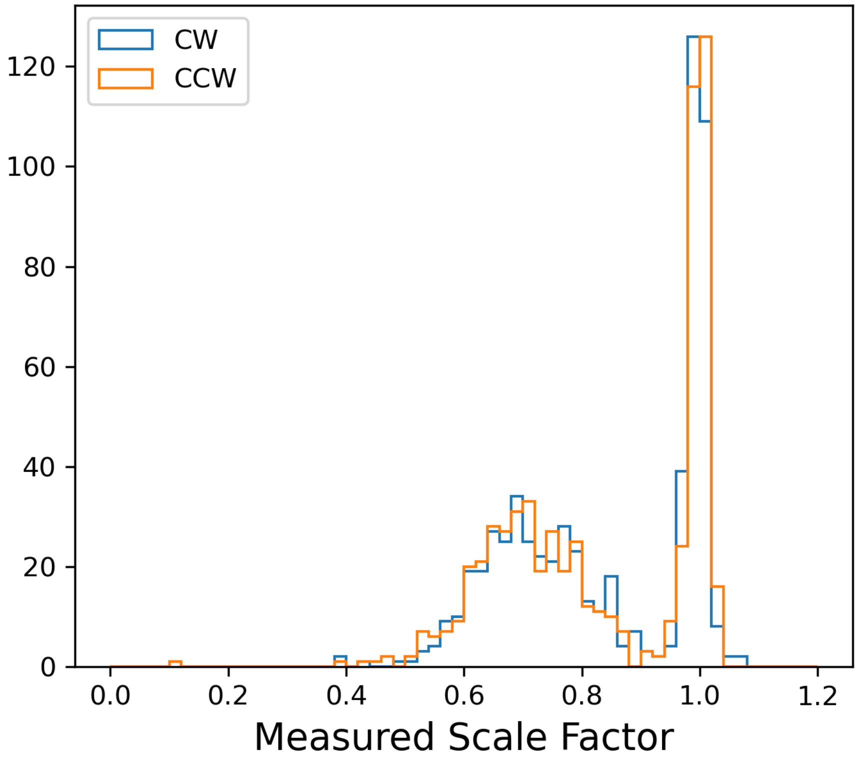

Figure 3.20: Measured scale factors from small angle arc tests at speed_100. The peak at scale factor = 1.0 corresponds to the linear theta positioners that were included in these tests as a control sample. The scale factors are estimated for each direction with clockwise (CW) shown in blue and counter-clockwise (CCW) shown in orange.

Grade	Max Blind Move Error	Max Correction Move Error
A	200 μm ($\geq$95%)	30 μm ($\geq$80%)
B1	200 μm ($\geq$95%)	30 μm ($\leq$80%)
B2	200 μm ($\leq$95%)	30 μm ($\geq$80%)
C	200 μm ($\leq$95%)	30 μm ($\leq$80%)

Table 3.3: Positioning error requirements for linear phi positioners. Linear phi positioners are categorized according to three grades, A, B, and C, with grade A returning to service. Grade B positioners are looked at more closely to decide if they perform well enough to return to service. Grade C positioners do not meet the requirements and will not return to service.

number of moves in the XY test can change depending on which sequence is used. We start with a 4-point XY test to validate and confirm the code is working as expected. We can then run either a 24-point, 50-point, or 100-point XY test. The moves in the 24-point test are ordered, while the moves for 50-point and 100-point tests are random.

In order to return the linear phi positioners to operation their positioning errors had to meet certain requirements. These are given in table 3.3. We defined three grades, A, B, and C, to categorize the performance of the linear phi positioners, essentially corresponding to “yes”, “maybe”, and “no” for returning positioners to operation. Grade A requires that 95% of blind moves be within 200 μm and that 80% of correction moves be within 30 μm. These are positioners that are expected to perform well during nightly operations. Grade B has two subcategories: B1 for positioners that meet the blind move requirement but not the correction move requirement and B2 for positioners that do not meet the blind move requirement but do meet the correction move requirement. Grade B positioners need to be looked at on a case by case basis to determine if they will perform well in nightly operations or not. Positioners with Grade B1 are more likely to be returned to service than those with Grade B2 since they perform well in the blind move and are not likely to cause any collisions. Grade C positioners do not meet any of the requirements and will not be returned to operations. They likely have erratic behavior and do not move well, even with a higher motor speed and scale factor corrections. Examples of the four grades are shown in 3.25.

petal0

On petal0 we ran multiple 100-point random XY tests to estimate and add scale factor corrections for the linear phi positioners. Figure 3.21 shows the results for one linear phi positioner, M02815, with scale factor corrections during a 100-point random XY test. The left plot shows the requested versus actual moves in phi for the blind move (black points) and correction move (green pluses). Aside from a few moves with a large requested phi angle, the points lie along the dashed line indicating that our applied scale factors are very close to the true value. The applied scale factors are listed in the upper left corner of the plot. The right plot shows the positioning error in microns over the 100-point test, with the blind move errors shown in the hashed histogram and the correction move errors shown in the solid green histogram. For this positioner, it had a maximum blind move error of 260 μm and 95% of its moves were within 163.5 μm. For the correction move roughly 38% of moves were within the 30 μm limit imposed by the science pipeline.

The positioning accuracy for all positioners in the 100-point XY test run on petal0 is shown in figure 3.22. There are 5 confirmed linear phi positioners on petal0, however one of them is also unstable in theta. We show the errors for the remaining four linear phi positioners in the right plot where roughly 80% of the correction moves were within the 30 μm and considered on target. The left plot shows the errors for the good phi positioners with 99% of the moves reaching the target threshold of 30 μm. The linear phi positioners had a correction move RMS of 22.9 μm compared to 20.8 μm for the good phi positioners. These numbers are high compared to what is achieved by the focal plane at KPNO, however, petal0 has a vastly different setup and as such typically has positioning errors 10-15 μm larger than what is seen at KPNO.

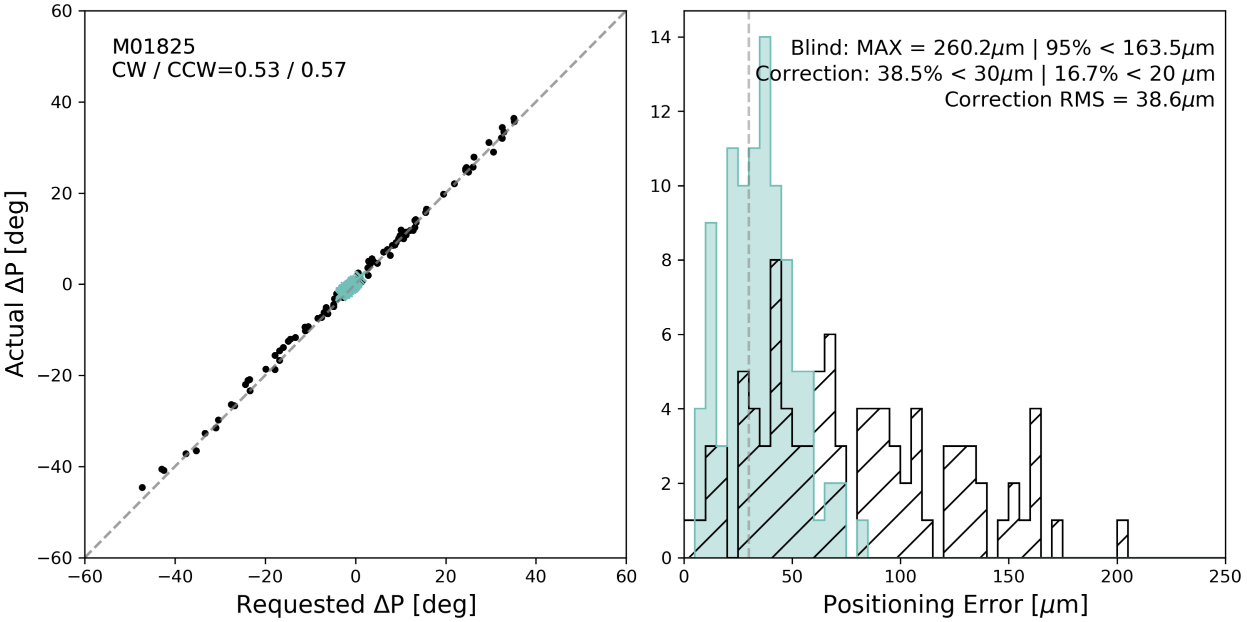

Figure 3.21: Results for one linear phi positioner, M01825, from petal0 for a 100-point XY test. The left plot shows the requested versus actual ΔP moves. The blind move is shown as the black points and the correction move is shown as the green pluses. The right plot shows the positioning error in microns for the XY test, with the blind move shown in the black hatched histogram and the correction move shown in the solid green histogram. The dashed grey line represents the 30 μm cutoff for the science pipeline.

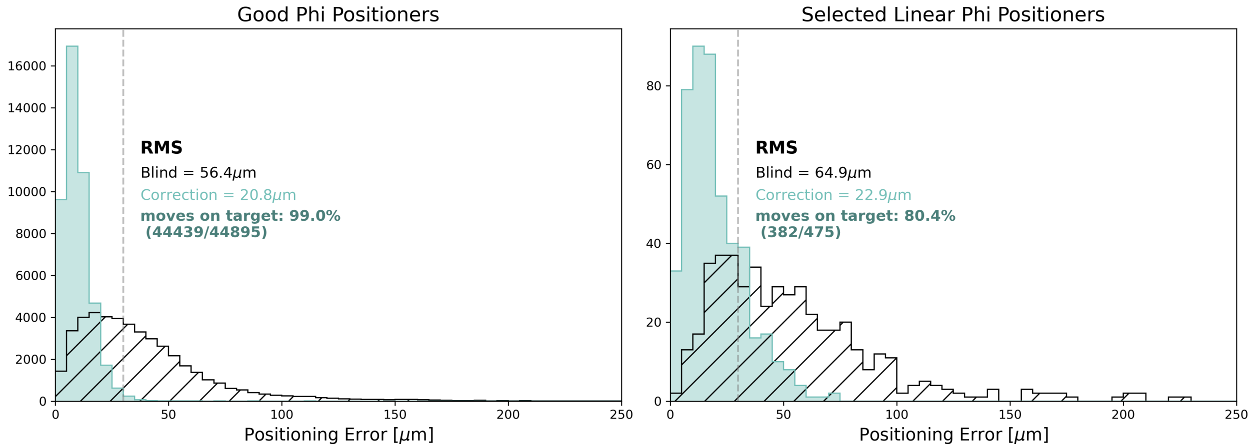

Figure 3.22: Positioning accuracy for a 100-point XY test run on petal0. The errors for the four confirmed linear phi positioners on petal0 are shown in the right plot, with the blind move shown as the black hatched histogram and the correction move is shown as the solid green histogram. The left plot shows the errors for the good phi positioners where 99% of the moves were on target.

Exposure ID	Number of Move Sequences	Applied Scale Factors
232265	50	A
232268	100	B
232451	50	C
232453	100	C
232455	20	C

Table 3.4: Details for the 5 XY tests run at KPNO in March. The exposure ID, number of move sequences, and the applied scale factors are listed in each column. Exposure ID 232455 was meant to be a 100-point test but had to be stopped early due to incoming bad weather.

KPNO

The XY tests at Kitt Peak are still ongoing. To date, we've run multiple XY tests to estimate and add scale factors, however we started by only testing linear phi positioners on two of the ten petals - petal 3 and petal 7. These two petals were chosen because they had the highest number of confirmed linear phi positioners, 95 of which were used for testing.

In March of 2024, we ran five XY tests: two 50-point, two 100-point, and one 100-point that had to be stopped after just 20 moves due to incoming bad weather. These tests are listed in table 3.4. There were three sets of scales used during the five XY tests: A, B, and C. Scales A were estimated from the arc tests run at KPNO discussed in section 3.6.2. For positioners that became linear phi after the arc tests, we applied a scale factor of 1.0. Scales B were estimated from the data taken in the first 50-point XY test using the model described at the beginning of this section. Scales C were estimated from the data taken in the first 100-point XY test (where scales B were applied). Many of the scale factors had converged for the majority of positioners, so we decided to keep scales C for the remaining XY tests. There were some positioners that did not perform well during these tests and their scale factors remained at 1.0. These positioners are not eligible to be returned to service. We show the distribution of scale factors for each positioner in figure 3.23. This figure shows the average of the clockwise and counter-clockwise scale factors for each positioner, ordered according to the value for scales C.

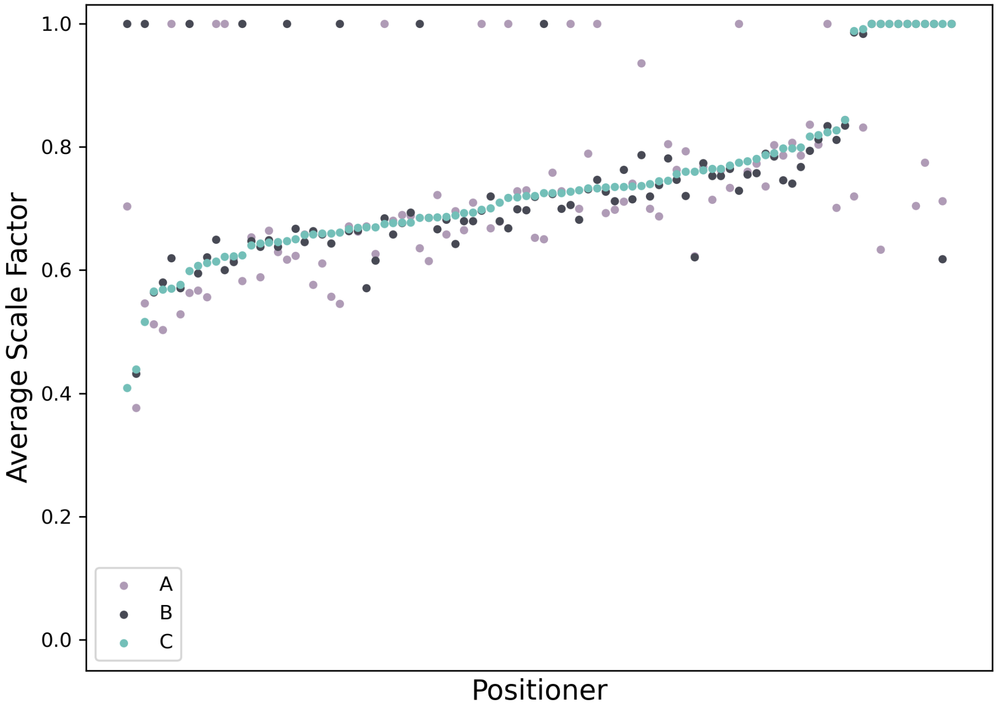

Figure 3.23: Average of the clockwise and counter-clockwise scale factors for the three different sets, A, B, and C, for the five XY tests run at KPNO. The scale factors are ordered by the value for scales C. Due to poor performance, some positioners had their scale factors set to 1.0 for all tests.

We classify the linear phi positioners with the data from the 100-point XY test (exposure ID 232453 in table 3.4) according to the requirements listed in table 3.3. A "grade A" positioner must have a positioning error of less than 200 μm for at least 95% of its blind moves and an error of less than 30 μm for at least 80% of its correction moves. We show these selection cuts in figure 3.24. Of the 95 positioners, 43 meet the grade A selection criteria (shown as green points in the upper left quadrant of the figure). The lower left quadrant are positioners that are "grade B1" as they meet the blind move requirement but not the correction move requirement. These are positioners that could be considered for return to service since they are unlikely to cause any collisions in the blind move. 4 of the 95 positioners fall into this grade (shown as the orange x's in the figure). The upper right quadrant are positioners that are considered "grade B2" as they meet the correction move requirement but not the blind move requirement. These positioners would not be considered for return to service since their blind move errors are too large and they would be more likely to cause collisions. 11 of the 95 positioners fall into this category. The lower right quadrant is "grade C" positioners which will not be returned to service. 32 of the 95 positioners fall into this category. These are shown as black x's in the figure, though all but one fall outside the limits of the plot. There are a non-negligible number of positioners that are in grade C due to their scale factors not converging by this XY test. We believe that with another 1-2 iterations of applying and measuring scale factors we will be able to bring approximately 20 positioners into the grade A category. These tests were performed during the July 2024 engineering shutdown and are discussed later in this section.

We visually inspected results of the 43 positioners meeting the grade A requirement and decided to remove two positioners from this list. These positioners performed reasonably well during the first four XY tests, however on the fifth XY test they each had multiple failed move attempts. We plan to include these two positioners in the next round of testing to see if they recover, as the fifth XY test had the least amount of moves of all the XY tests.

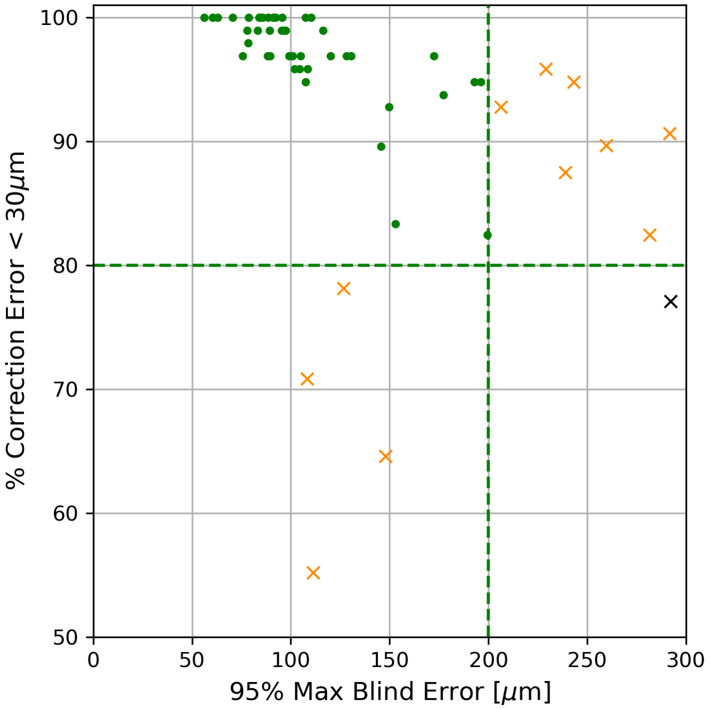

Figure 3.24: Selection of linear phi positioners following the grading cuts given in table 3.3. Grade A positioners are shown as the green dots. For these positioners, 95% of blind move errors must be less than 200 μm and a the correction move error must be less than 30μm 80% of the time. They were visually inspected to create the final sample of 41 positioners that will be returned to service. The orange x's represent the grade B positioners, and the black x's represent the grade C positioners.

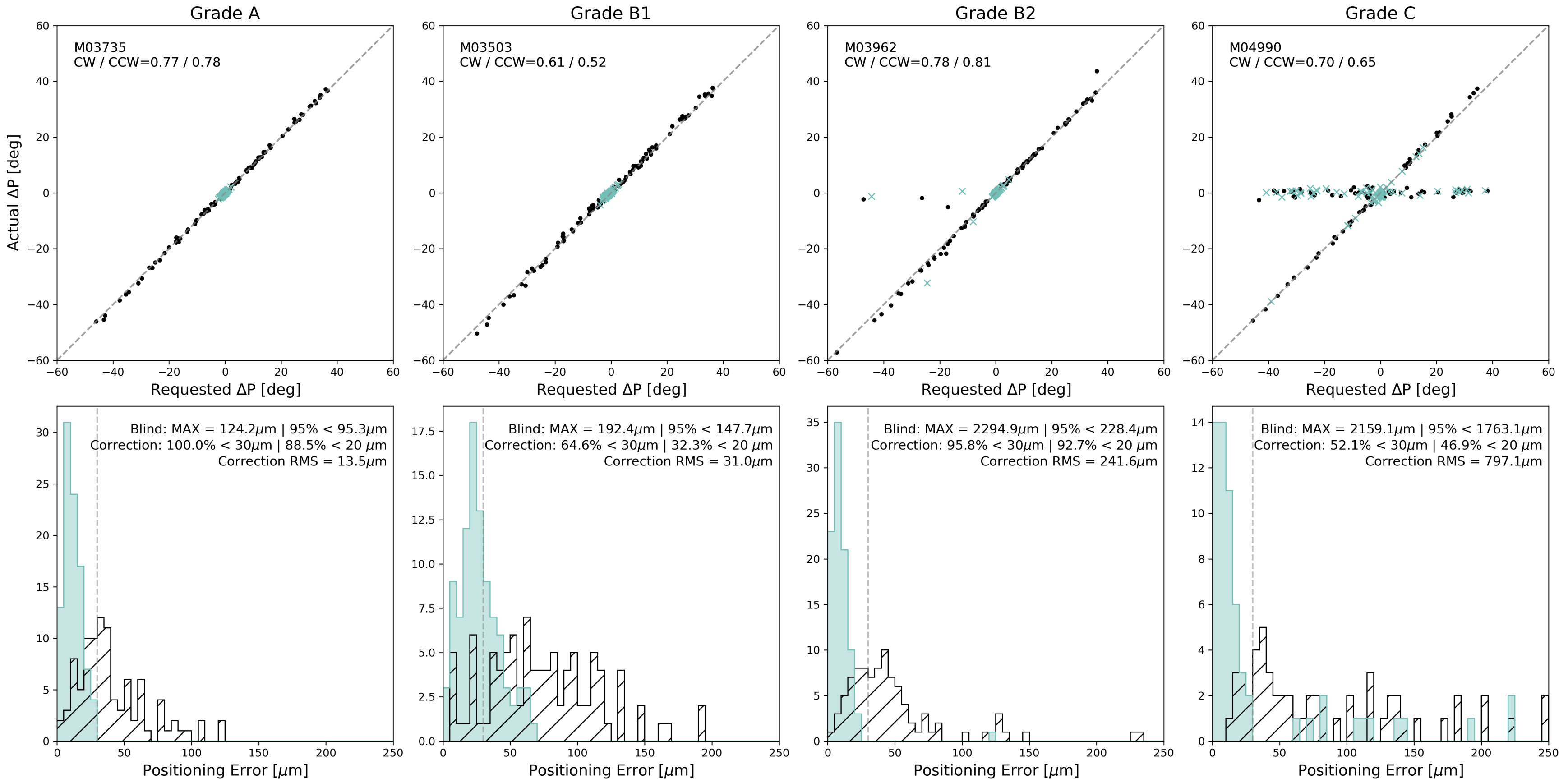

Figure 3.25: Results from the 100-point XY test (exposure ID 232453) showing an example of each grade of positioner. The top row shows the requested move vs the actual move for the blind move (black points) and the correction move (green x's). The applied scale factors are listed for each positioner. The bottom row shows the positioning error for the blind move (black hatch) and the correction move (solid green). The blind and correction move errors are given for each positioner. The left column shows an example of a grade A positioner, the middle column a grade B positioner, and the right column a grade C positioner.

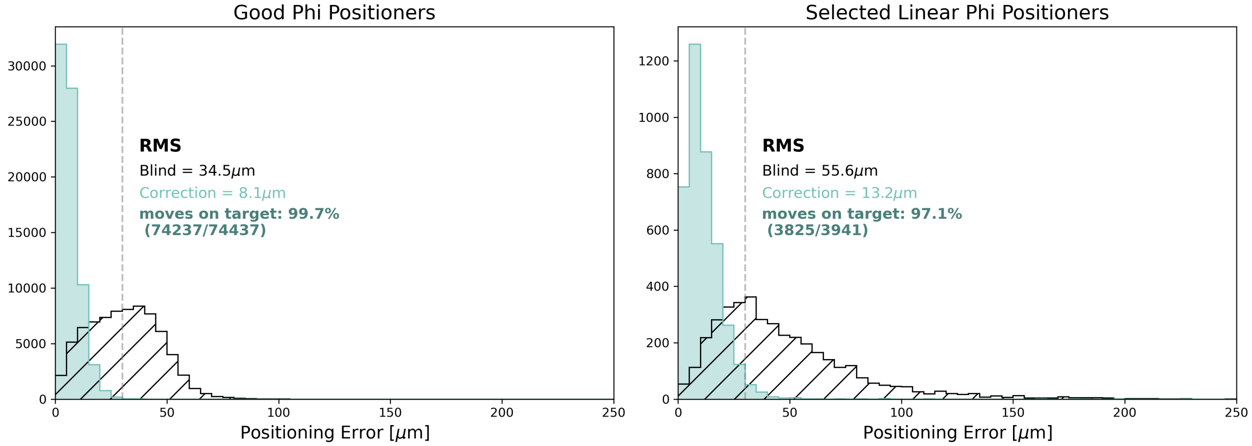

Figure 3.26: Positioning accuracy for the 100-point XY test using the best estimate of scale factors (scales C) for the good phi positioners (left panel) and the 41 selected linear phi positioners (right panel) that will be returned to operations. The positioning error for the blind move is shown in the black hatched histogram and the correction move is shown in the solid green histogram. The linear phi positioners have errors only 1.5 times larger than the good phi positioners, with a correction move RMS of 13.2μm compared to 8.1μm, respectively.

We show example move data for each grade in figure 3.25. The left column shows M03735 which has a blind move error of 95.5μm and a correction move RMS of 13.5μm. This positioner was one of the 41 selected and was partially returned to service in June of 2024. The second column shows M03503 which was classified as grade B1. This positioner has a blind move error of 148μm and a correction move RMS of 31μm. Though it meets the requirement for the blind move, it only achieved a positioning error of $< 30\mu$m for 64% of correction moves. Discussions are still taking place on whether this is acceptable for science operations. If this positioner was returned to service only 64% of its light collected would be usable for science, however that is 64% more than is being used now. The third column shows a grade B2 positioner, M03962. 95.8% of it's correction moves were within 30 μm, however due to a few bad moves it did not meet the blind move error requirement. The right column shows an example of a grade C positioner, M04990. Many of this positioner's moves, both in the blind and correction, did not move at all which creates a cross-like pattern in the requested vs actual move plot. As a result, the positioning errors for both the blind and correction move are much larger than the requirement.

The linear phi positioners have a positioning error roughly 1.5 times larger than the good phi positioners. We plot the positioning accuracy for the 100-point XY test (expid 232453) for the 896 good phi positioners (left panel) and the selected 41 linear phi positioners (right panel) on petals 3 and 7 in figure 3.26. The blind move is shown in the hatched histogram, and for the linear phi positioners has an RMS of 55.6μm compared to 34.5μm for the good phi positioners. The correction move is shown in the green solid histogram and has an RMS of 13.2μm for the linear phi positioners and 8.1μm for the good positioners. The linear phi positioners were on target (correction moves $< 30\mu$m) 97.1% compared to 99.7% for the good phi positioners.

The selected 41 linear phi positioners were returned to service in the focal plane on June 23, 2024. They were first positioned for science exposures on June 25, 2024 and ran for three nights until the morning of June 28, 2024. We discuss the behavior of the positioners for each of the three nights in the sections below.

June 25

All 41 positioners were run for science observations on June 25. There were 5 positioners that moved poorly and were disabled for observations the following two nights. These 5 positioners were all on Petal 3. Move requests for the blind and correction moves for one of the disabled positioners, M03656, are shown in figure 3.27. As shown, this positioner was requested to move numerous times but did not. The positioning errors for the 36 positioners that performed well is shown in the top left panel of figure 3.28. The blind move is shown in the black hatched histogram and the correction move in the solid green histogram. 35.4% of the correction moves were under the 30 μm cutoff to be considered on target for science. This is considerably different than the 97% of moves that were on target during the XY test shown in figure 3.26.

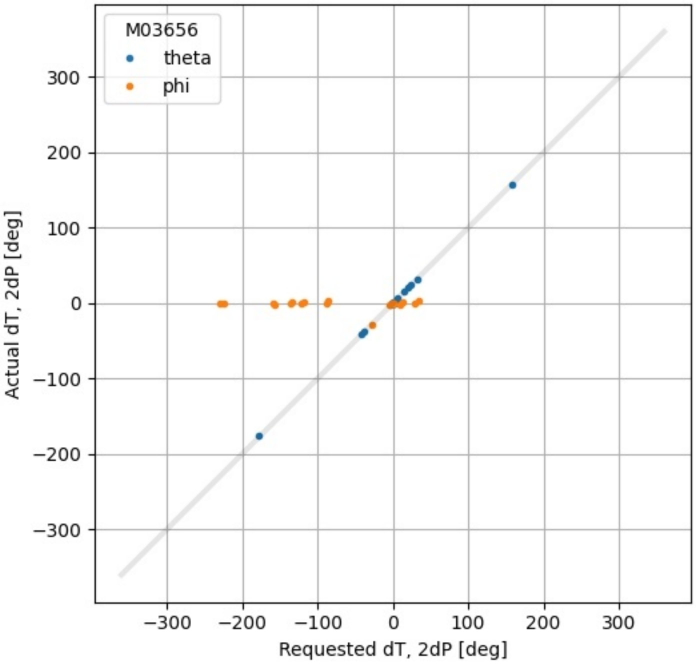

Figure 3.27: An example of a poorly performing linear phi positioner during the night of June 25th, M03656. As shown in the orange points, this positioner had many move requests in phi, but did not move for the majority of them. This positioner was disabled the following morning.

June 26

The night of June 26 therefore started with 36 positioners: the selected 41 minus the 5 that were disabled from the prior night of observing. Another 5 positioners performed poorly and were disabled the following morning. These 5 positioners are also located on Petal 3, bringing the total to 10 disabled positioners. Petal 3 only had 11 of the 41 recovered linear phi positioners. It is unclear why the poorly performing positioners only appeared on Petal 3. There was another linear phi positioner on Petal 7 that was disabled due to a collision error with a disabled neighbor. The positioning errors for the remaining 30 linear phi positioners is shown in the top right panel of figure 3.28. The number of moves that were on target increased to 50%, a 15% increase from the previous night.

There were also numerous errors from the anti-collision software on the night of June 26, causing the positioning sequence to abort and as a result the previous exposure (being saved at the time of positioning) was also lost. The issue of saving exposures during a positioning loop failure has since been fixed, however, though a fix is in place, the error with anti-collision is still not fully understood. On four exposures anti-collision claimed that it could not resolve collisions between different pairs of positioners. Initially, this was thought be due to a bug in the code during the XY tests that expanded each linear phi positioner's keepout zone (the "bubble" around each positioner that other positioners are not allowed to enter). However, the error from anti-collision persisted even after the expanded keepouts were fixed. This error was not seen when testing on petal0 at LBL even when we had confirmed collisions in some early tests. It is now thought that the error occurs when a neighboring positioner is disabled, though this is still under investigation.

June 27

The last night of observations, June 27, had 30 of the 41 linear phi positioners enabled at the start of the night. After another anti-collision about halfway through the night, it was decided to disable all linear phi positioners that had a disabled neighbor. Not all of the linear phi positioners with disabled neighbors experienced the anti-collision errors. In fact, one of the better performing linear phi positioners, M03609, had 4 disabled neighbors and had RMS positioning errors of 170 μm for the blind move and 21 μm for the correction move with 88% of its correction moves being on target. 20 of the 30 positioners had at least one disabled neighbor, leaving only 10 positioners for the remainder of the night.

The positioning errors for both sets of positioners are shown in the bottom row of figure 3.28. The set of 20 positioners ("20240627a" in figure 3.28) that were enabled for the first half of the night were on target 67% of the time, while the set of 10 positioners ("20240627b" in figure 3.28) that were enabled the entire night were on target 71% of the time. Though much improved over the three nights, this is still significantly different than the accuracy seen during the XY tests.

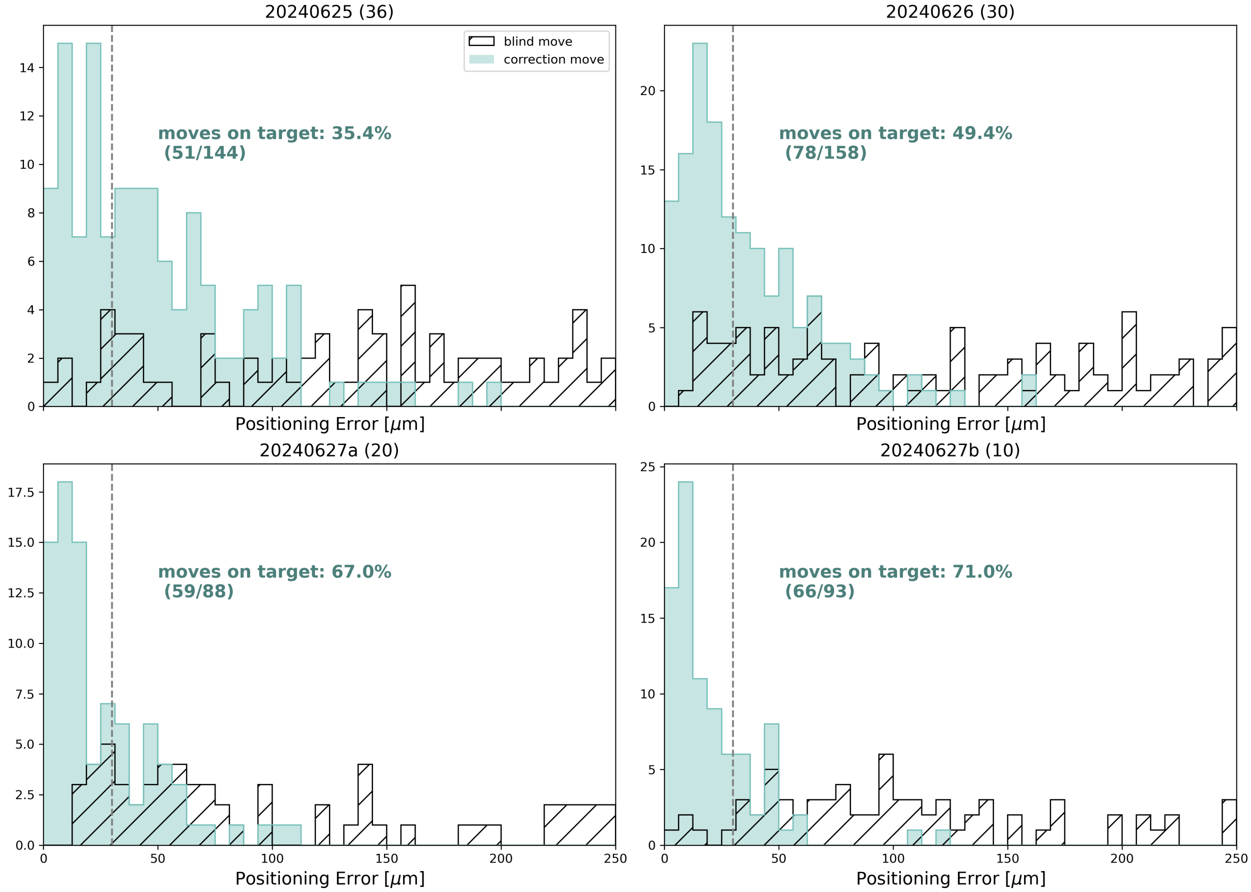

Figure 3.28: Positioning errors from the selected linear phi positioners during the 3 nights of main survey operations in June. The number of positioners that were included in the error calculation is given at the top of each plot - not included are the positioners that were disabled at the end of each night. The night of June 27th, 2024 is split into two categories. Category A (lower left) is for positioners that were only enabled for the first half of the night. Category B (lower right) shows the positioners that were enabled the entire night.

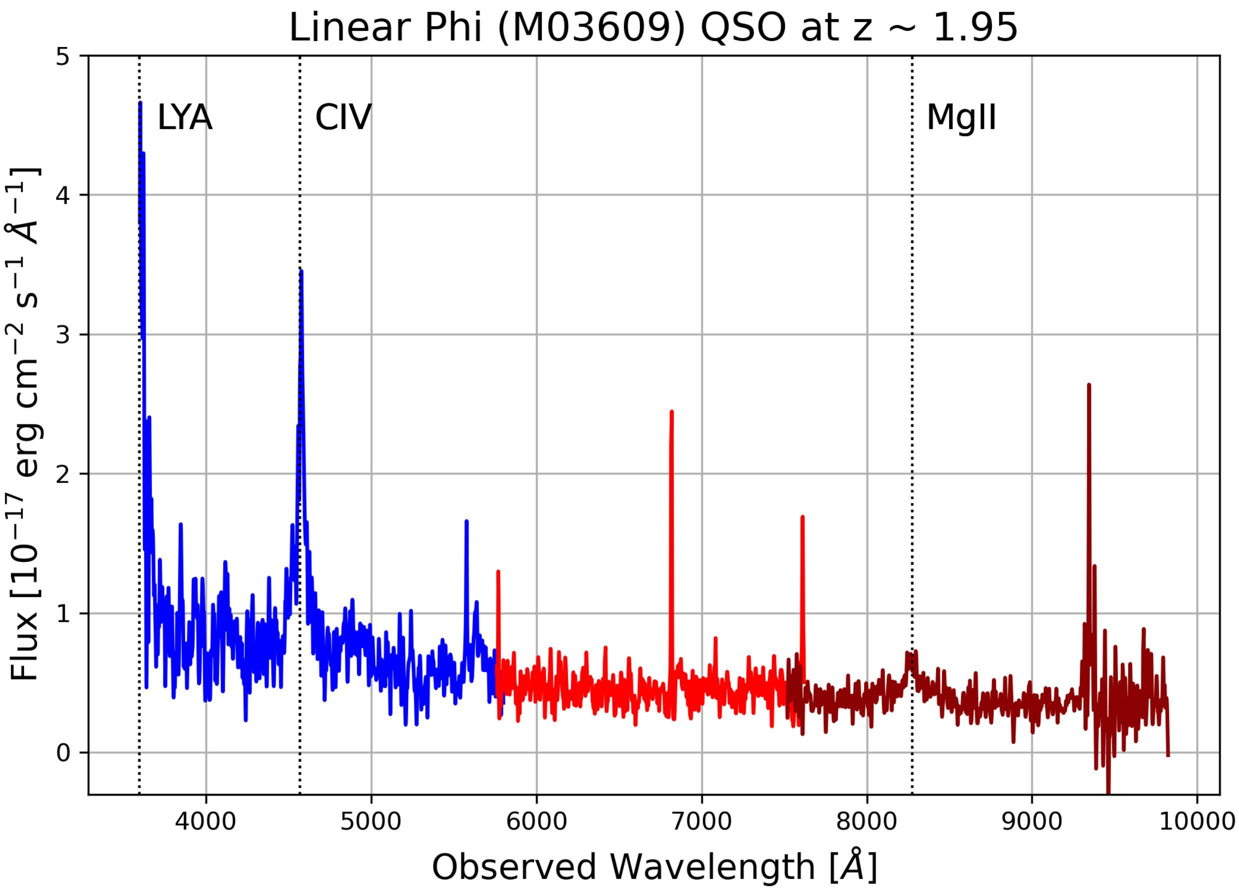

Figure 3.29: Quasar spectrum captured using a linear phi positioner from data collected on the night of June 26th, 2024. This spectrum is flux calibrated. The prominent Lyα, CIV, and MgII emission lines are highlighted and the redshift is estimated to be $z \sim 1.95$.

Nevertheless, over 250 spectra were collected from the linear phi positioners across the three nights. An example of a quasar spectrum from one of the linear phi positioners, M03609, collected on June 26 is shown in figure 3.29. This spectra is calibrated by the pipeline, the data from the three different arms is still separate (blue, red, and infrared) and noise has not been subtracted. The data has been smoothed to minimize the impact of the noise. Three prominent emission lines, Lyα, C IV, and MgII are labeled. The redshift of this quasar was calculated (not by the pipeline) to be $z \sim 1.95$.

July 2024 XY Tests

During the engineering time in July 2024, we ran three XY tests on 314 confirmed linear phi positioners: one 25-point, one 50-point, and one 100-point. Each XY test was run with an updated set of scale factors. We grade the positioners according to the results from the 100-point XY test, following the requirements given in table 3.3. We show the selection results in figure 3.30. 213 positioners meet the initial requirements, but it was decided to relax the correction move requirement to 70%. This adds an additional 15 positioners which are not at risk of causing any collisions since their blind move errors are within the requirement, bringing the total recovered positioners to 228 or roughly 72% of the linear phi positioners. During the course of the XY tests there were 28 positioners that were disabled due to poor performance. An additional 37 positioners did not meet the requirements, however 5 of these would likely be returned to service with a scale factor adjustment.

We show the positioning errors for the blind and correction moves during the 100-point XY test in figure 3.31. The right panel shows the errors for the 228 linear phi positioners during the test, where 90.9% of moves were on target. The RMS for the blind and correction moves is comparable for the good phi positioners and the linear phi positioners. These results are extremely encouraging and discussions are taking place to determine the timeline for returning these positioners back to service.

3.7 Conclusions and Future Tests

To date, we have partially recovered 41 linear phi positioners on petals 3 and 7 from the DESI focal plane. During testing, these 41 positioners had a positioning error 1.5 times larger than the ∼900 good phi positioners on these two petals. The positioning accuracy improved each night during the three nights these positioners were included in observations,

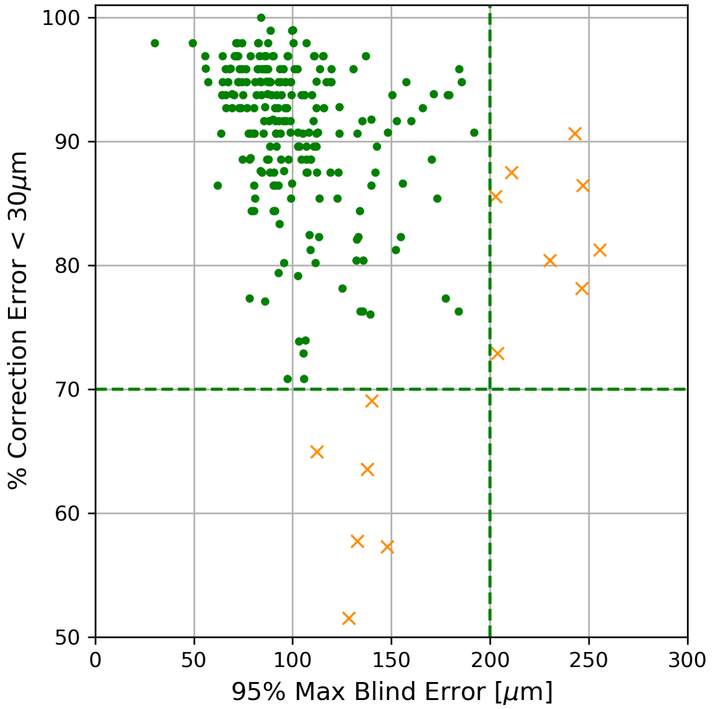

Figure 3.30: Selection of linear phi positioners following the XY tests performed in July 2024. This selection follows the same requirements given in table 3.3, except that the correction move requirement has been reduced from 80% to 70%.

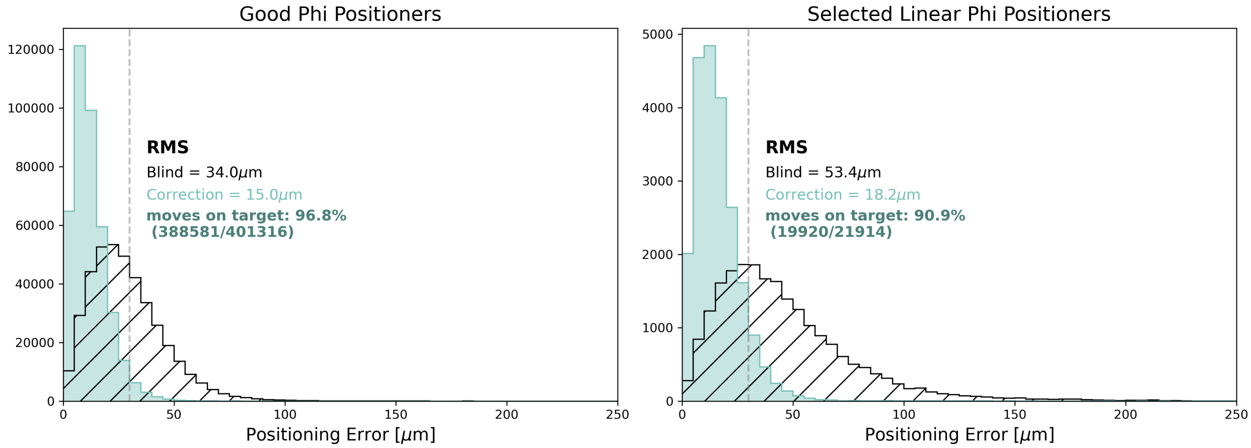

Figure 3.31: Positioning accuracy for the 228 selected linear phi positioners during the 100-point XY test. The blind move errors are show in the black hatched histogram and the correction move errors are shown in the green histogram. The left plot shows the positioning errors for the 4,665 good phi positioners during the test and the right plot shows the errors for the selected linear phi positioners. Just under 91% of correction moves were within the 30 μm cutoff (dashed grey line).

though the accuracy each night was significantly different than it was during testing.

During the next round of testing, we measured updated scale factors for the other positioners on petals 3 and 7 that were classified as grade B or C during this first round of tests. These positioners did not meet the grade A requirement during the initial round of tests as their scale factors had not converged by the time we were applying "scales C" to moves. After this round of testing, 11 additional positioners were selected from petals 3 and 7.

We ran three XY tests on the linear phi positioners in the remaining 8 petals on the DESI focal plane. There are approximately 500 linear phi and theta positioners on those petals, roughly half of which are linear phi. Based on the results from the 100-point XY test, we will recover a total of 228 linear phi positioners across the entire focal plane, corresponding to roughly 72% of the linear phi positioners. During the 100-point XY test, these positioners were on target just under 91% of the time. Discussions are taking place to determine when these positioners will be returned to nightly operations. This could occur as early as August.

We have also started plans to test the linear theta positioners at LBL on the test stand and on petal0. Preliminary results show that they behave similarly to the linear phi's at the default motor speed of 9900 RPM, however the parameter space has not been sufficiently explored to say with confidence that they will perform as well as the phi's at speed_100. We have already started testing and plan to continue testing linear thetas on the LBL test stand to explore this parameter space. If we can determine an operational speed we will migrate testing to petal0, where the code is already in place.

Should the recovery efforts for the linear phi positioners on the remaining 8 DESI petals fail, we would at least recover the 41 from petals 3 and 7. This would bring the total linear phi and theta positioners down to 559 from 600. Since the start of the main survey, we've seen an onset rate of approximately one new linear device per week, as shown in figure 3.6. If we assume that the 1 per week rate holds until the main survey ends in 2026 and that the 228 recovered positioners remain in operation, there will be 491 total linear phi and theta devices at the end of the survey. However, it is clear from the figure that since at least January 2024 the rate has decreased to less than 1 per week. This is most important for the planned DESI-1b extension and future DESI-II surveys. DESI-1b will run for 2.5 years after the 5 year DESI survey ends in mid-2026, ending in 2028. DESI-II is planned to begin in early 2029 and run for 6 years until 2034. If the 1 per week rate increases or continues through DESI-II, there could be serious implications to survey planning and strategy.

3.8 Appendix A

The following figures show the results of testing the various ramp speeds (listed in table 3.2) for the four linear phi positioners at LBL. Each set of plots corresponds to a different speed, given in the title. Each row corresponds to a linear phi positioner. The left and middle columns show the results of the move tests in the clockwise (CW) and counter-clockwise (CCW) directions for the moves when no scale factor was applied (blue points) and the moves when a scale factor correction was applied (orange points). The measured scale factor is given in the legend for each direction as well as the number of moves. The right column shows the measured positioning error (requested - measured) and lists the RMS and the maximum for each positioner. These numbers are also reported in figure 3.15.

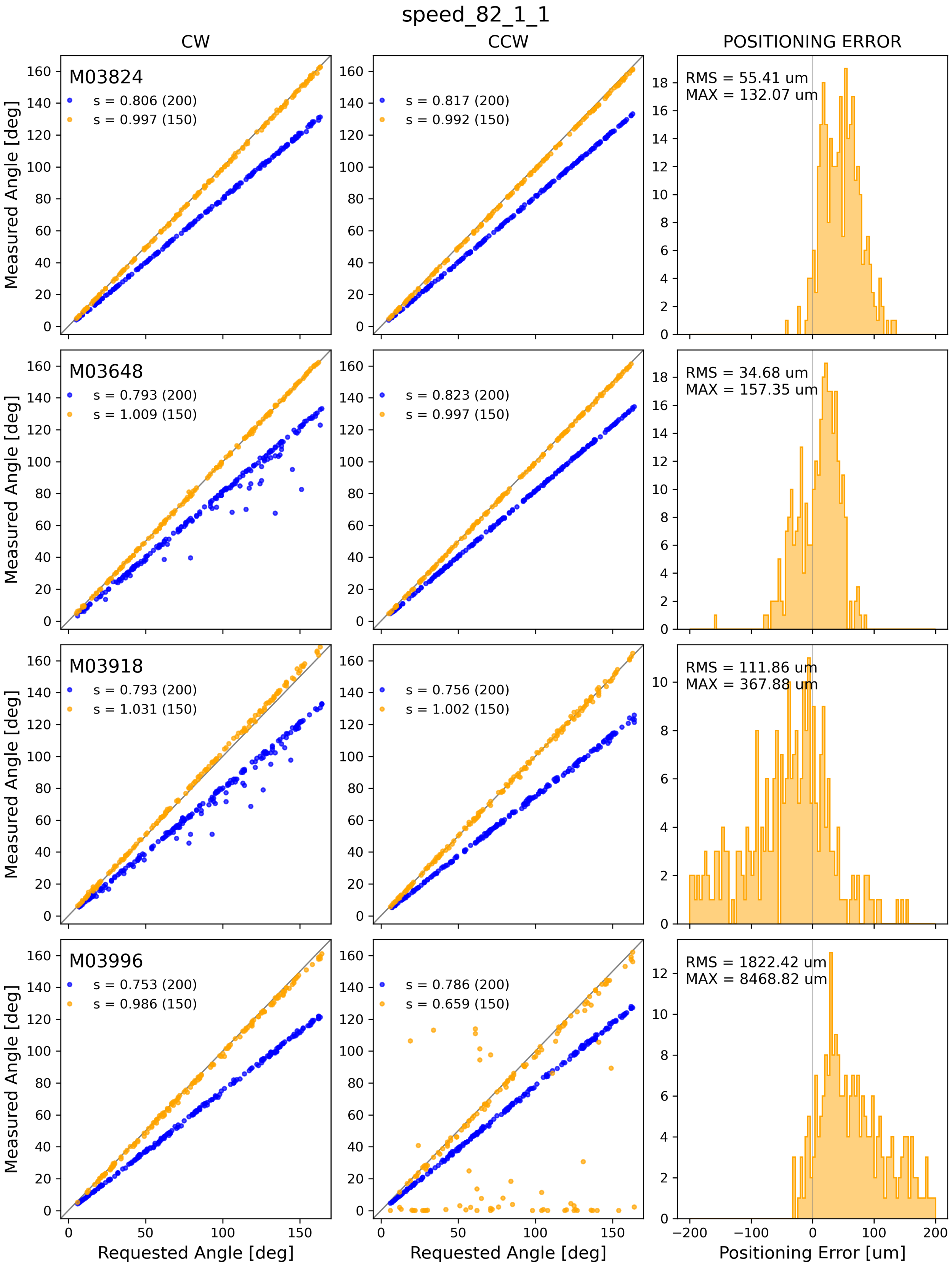

Figure 3.32: speed_82_1_1: 24,600 RPM, 1.009 degree ramp up and ramp down.

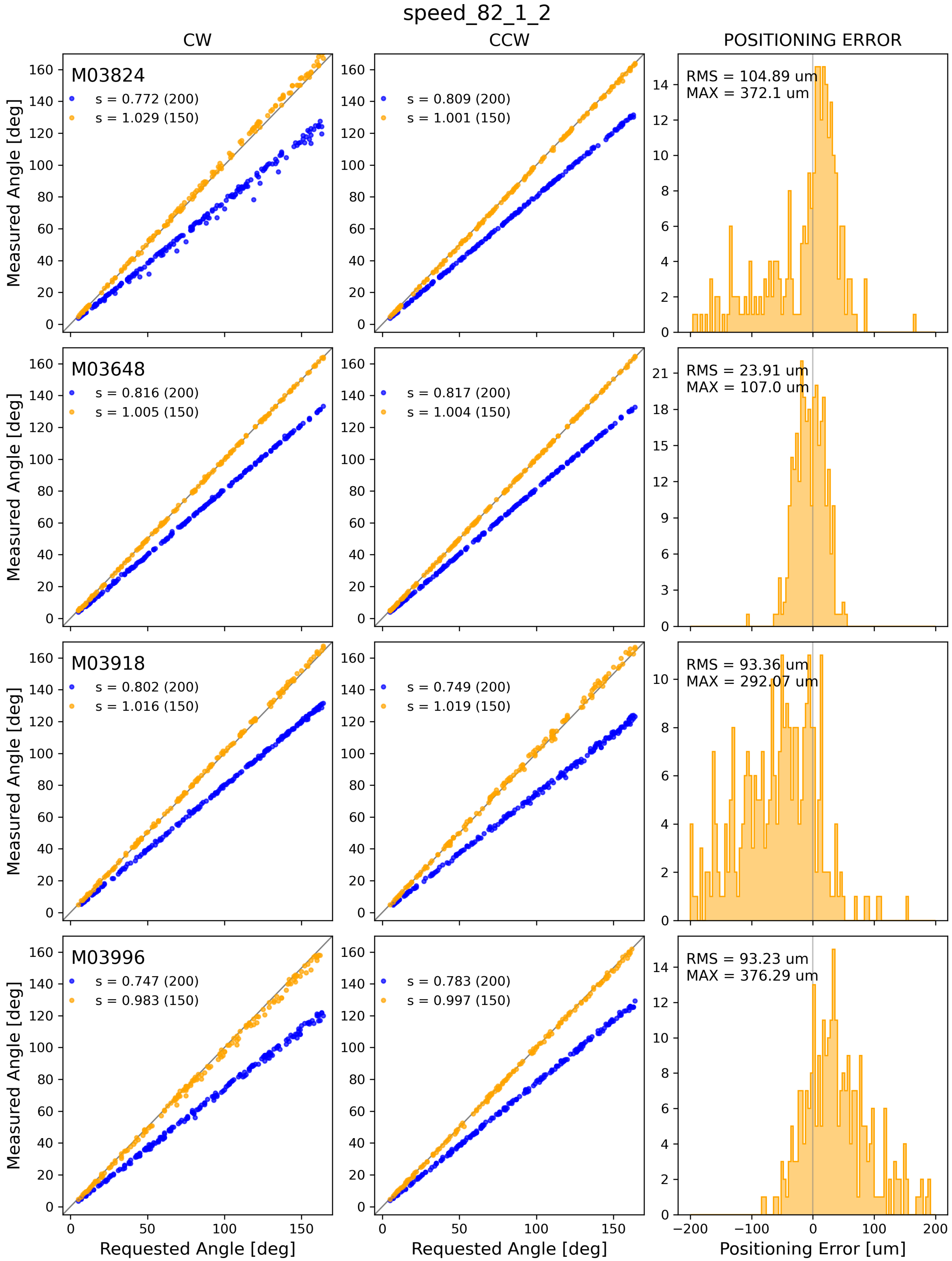

Figure 3.33: speed_82_1_2: 24,600 RPM, 1.009 degree ramp up, 2.017 degree ramp down.

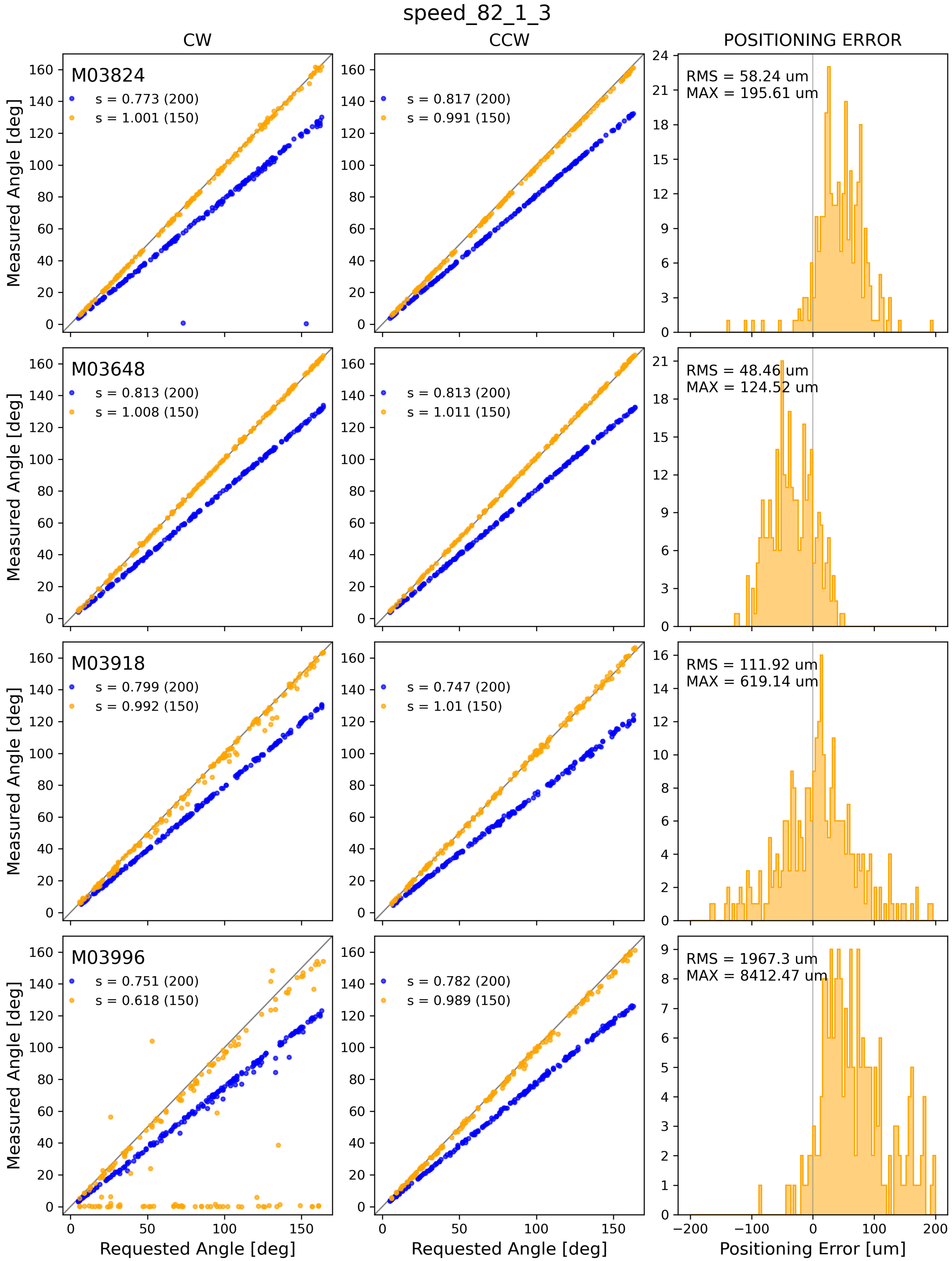

Figure 3.34: speed_82_1_3: 24,600 RPM, 1.009 degree ramp up, 3.026 degree ramp down.

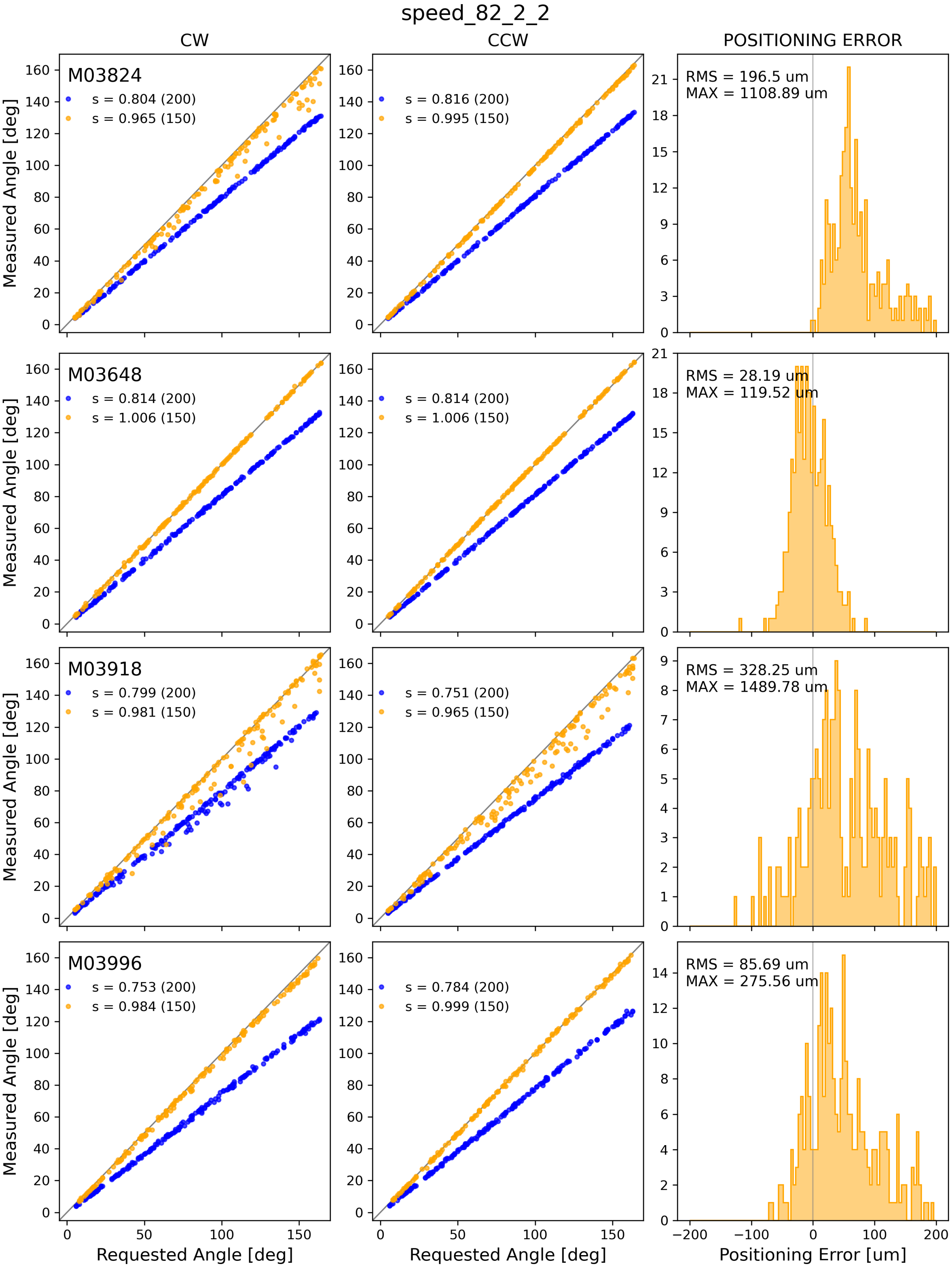

Figure 3.35: speed_82_2_2: 24,600 RPM, 2.017 degree ramp up and ramp down.

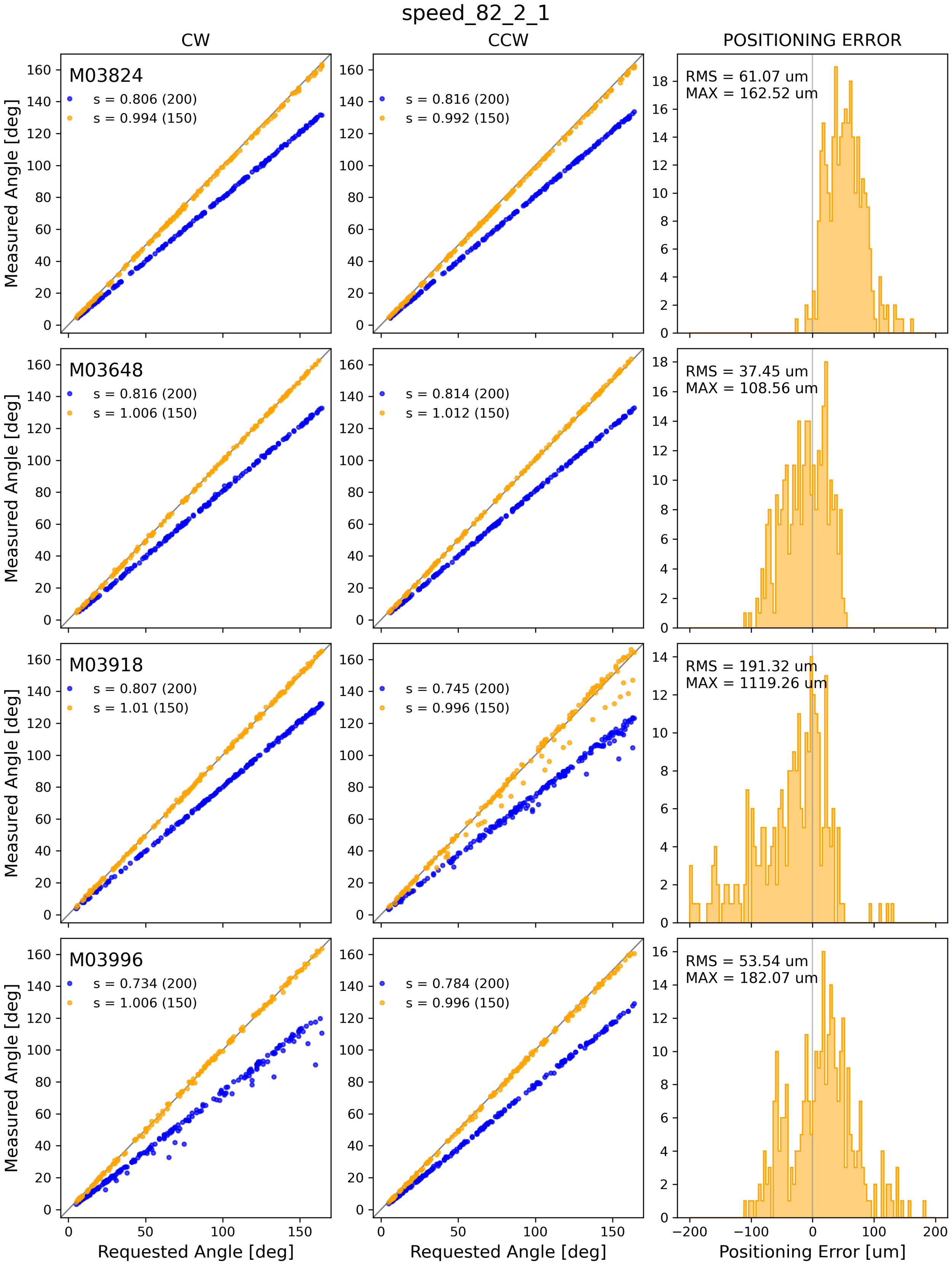

Figure 3.36: speed_82_2_1: 24,600 RPM, 2.017 degree ramp up, 1.009 degree ramp down.

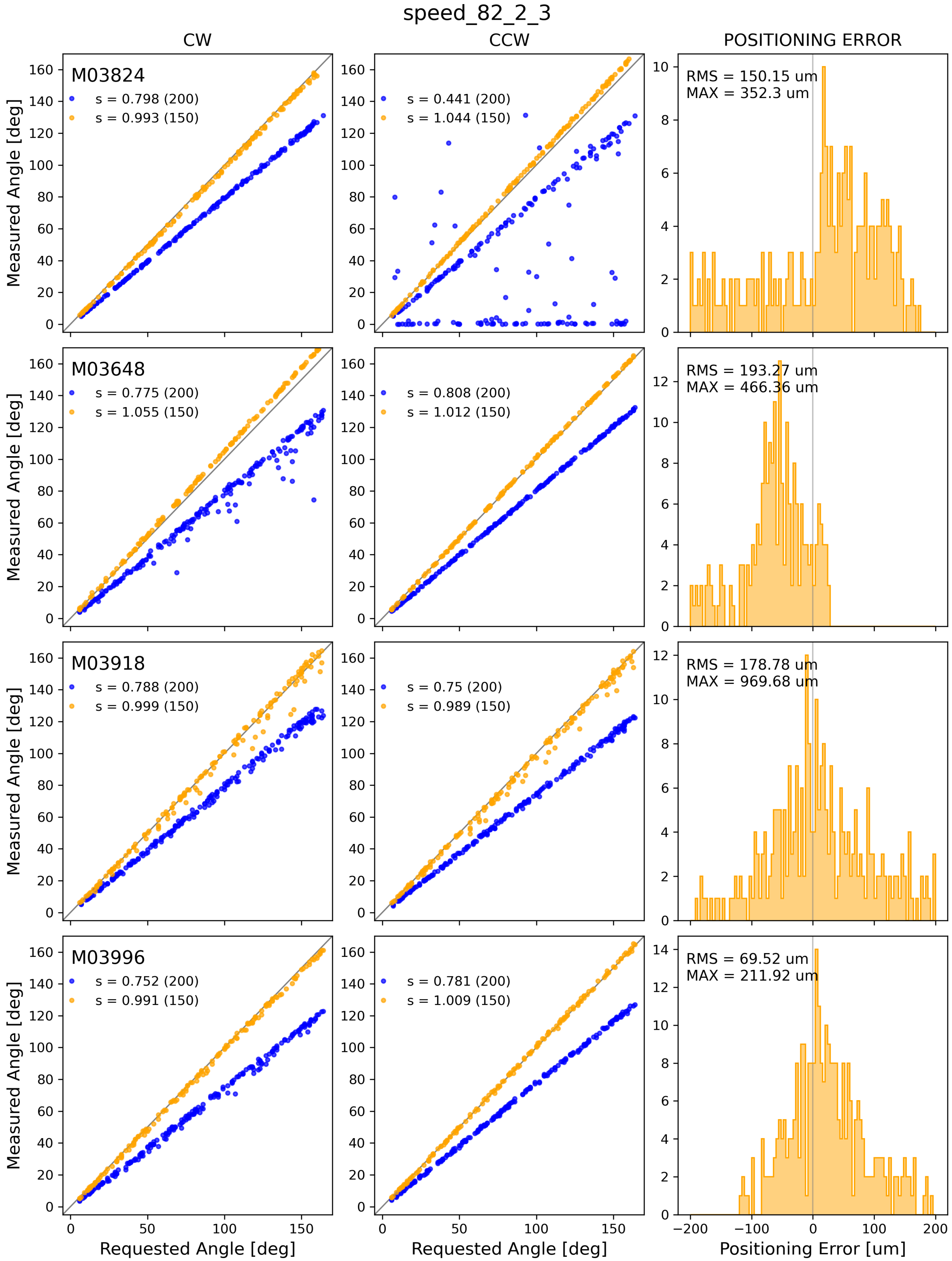

Figure 3.37: speed_82_2_3: 24,600 RPM, 2.017 degree ramp up, 3.026 degree ramp down.

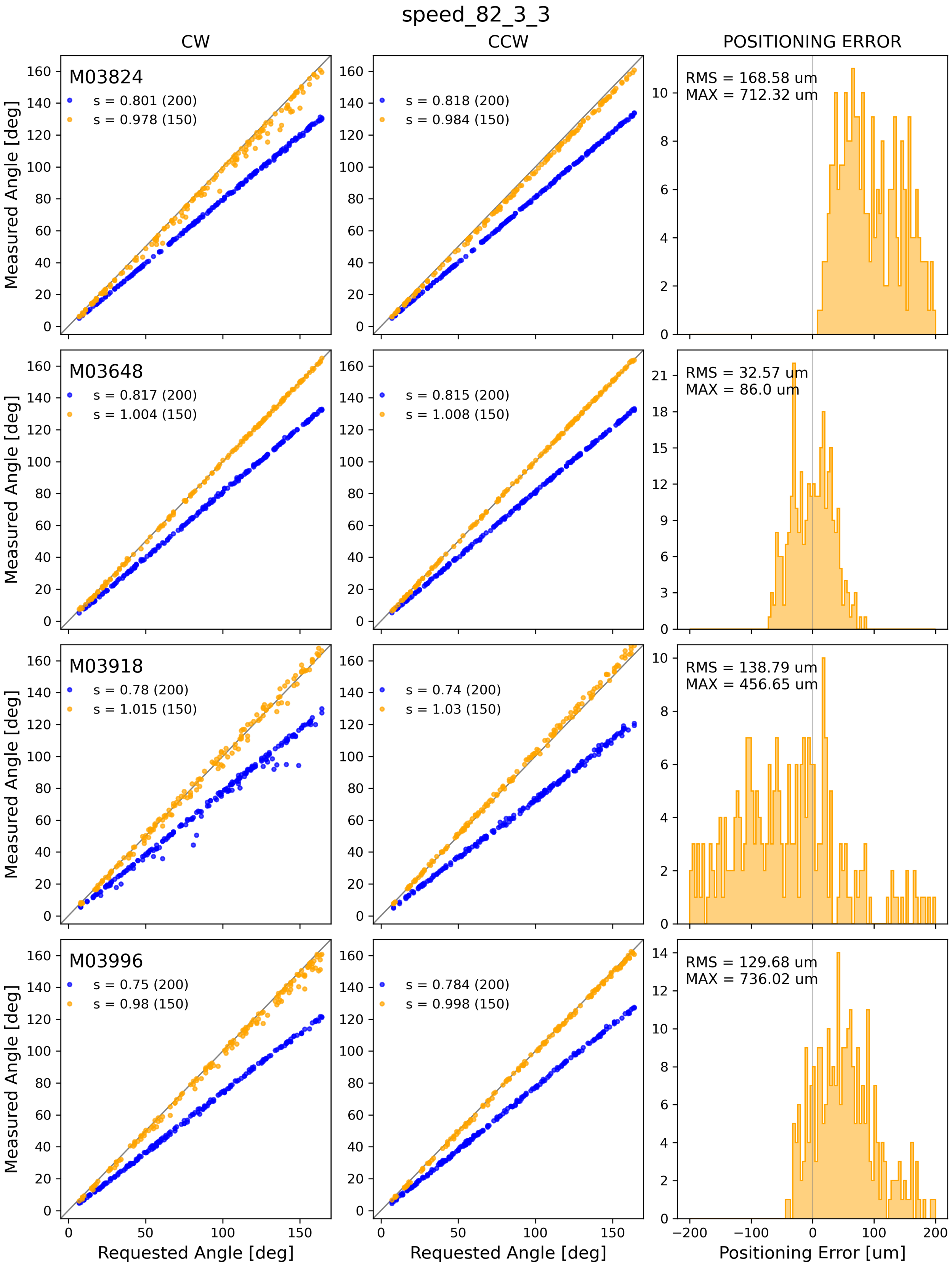

Figure 3.38: speed_82_1_3: 24,600 RPM, 3.026 degree ramp up and ramp down.

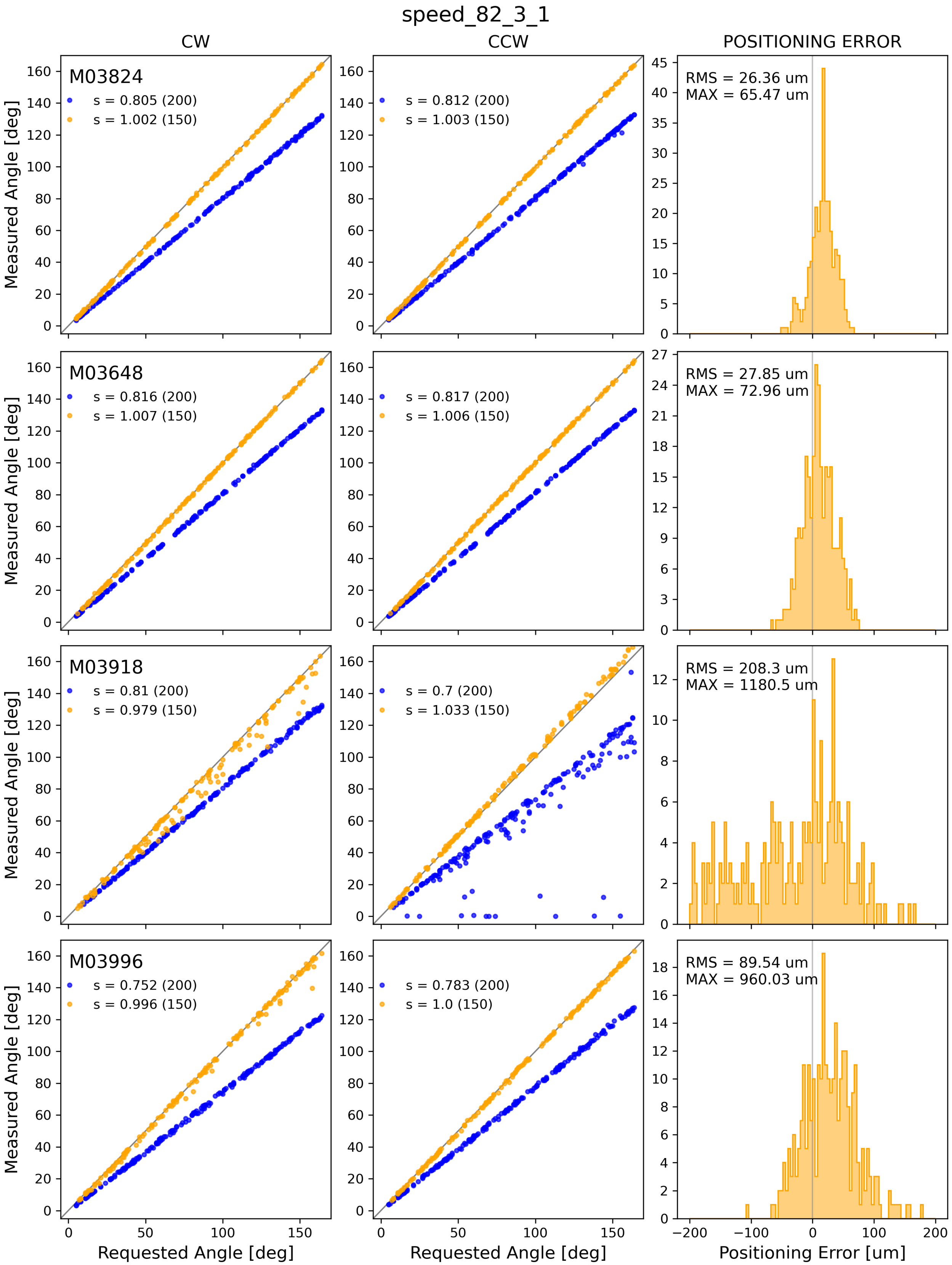

Figure 3.39: speed_82_1_3: 24,600 RPM, 3.026 degree ramp up, 1.009 degree ramp down.

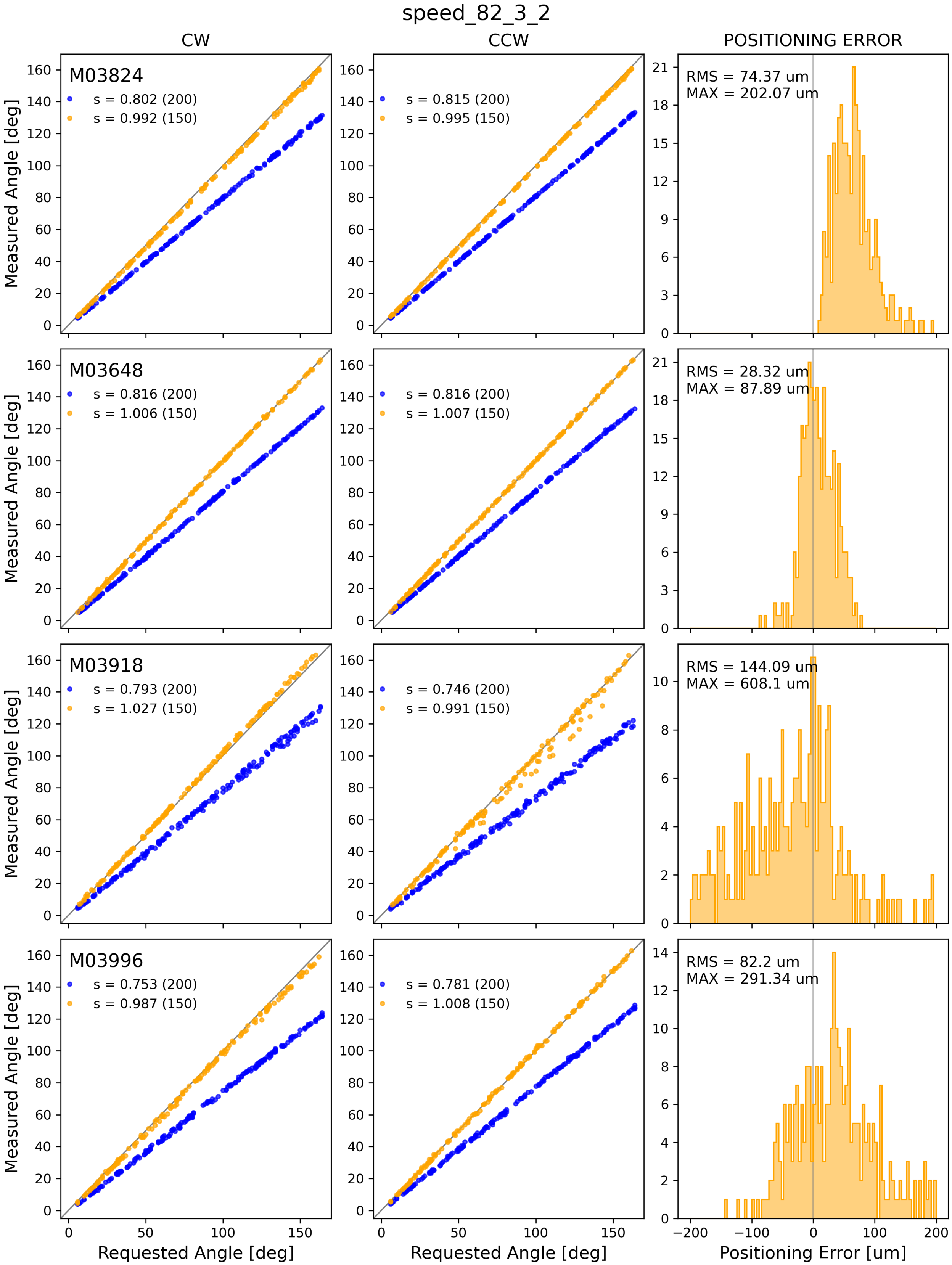

Figure 3.40: speed_82_1_3: 24,600 RPM, 3.026 degree ramp up, 2.017 degree ramp down.

Chapter 4

Impact of Systematic Redshift Errors on the Cross-correlation of the Lyman-α Forest with Quasars at Small Scales Using DESI Early Data

4.1 Introduction

The Dark Energy Spectroscopic Instrument (DESI) [30, 36, 37] saw its first light in October 2019 and began its main survey in May of 2021. Prior to the main survey, DESI collected spectra in its Survey Validation (SV) [31] phase between December 2020 and May 2021, which make up the data for the Early Data Release (EDR) [32]. The EDR consists of approximately 1.7 million unique spectral objects among which 90,000 are quasars. Over the course of 5 years, DESI will collect spectra from 40 million extragalactic objects, with approximately 3 million of those spectra coming from quasars [31, 32].

Quasars, or quasi-stellar objects (QSO), offer access to the highest extragalactic redshifts that can be observed and measured by DESI. Indeed, they are among the most luminous sources in the universe and as such they have been used for many years to study the large-scale structure of the universe as well as probing the expansion of the universe using Baryon Acoustic Oscillations (BAO) [19, 27, 43, 64, 81, 103]. The BAO scale, a standard ruler once normalized to the sound horizon r_d, allows for constraints on cosmological parameters [5, 25].

At high redshifts ($z > 2.0$), in order to study the large-scale matter distribution, DESI is not only utilizing quasar positions, but also the Lyman-α forest in their spectra. The Lyman-α forest is created when the light of a distant quasar passes through and is absorbed by intervening neutral Hydrogen gas in the intergalactic medium (IGM). The light from the quasar is redshifted as it travels and once it is redshifted to the wavelength of the Lyman-α transition (1215.67 Å), it will be absorbed by the neutral hydrogen in the IGM. This occurs anytime the light is redshift to the Lyman-α transition, thus creating the "forest". Using both quasars and the Lyman-α forest as tracers, it is possible to measure the BAO scale to high precision. This was already done by the eBOSS collaboration [43]. DESI recently also measured 3D correlations with quasars and the Lyman-α forest using EDR data [56], though the results on BAO were not reported. Beyond BAO, high-redshift quasar spectra are also used, for example to measure the 1D power spectrum (P1D) of the Lyman-α forest [70, 87], or to study metals in the intergalactic medium [71].

In order to get the high precision needed for the cosmological measurements with BAO and P1D, the redshifts that DESI measures for each quasar spectrum need to be extremely precise. While the redshift measurement of the majority of DESI galaxies, which rely on the presence of narrow emission lines and spectral features, is indeed very precise, this is not the case for quasars whose emission lines are essentially broad, and complex. There are therefore many factors that can cause errors on redshift measurements. Quasars that have Broad Absorption Line (BAL) features tend to have larger errors on redshift since the BAL features tend to affect the absorption blueward of the emission line centers. The resulting emission line asymmetry can shift the redshift estimate [49, 54]. Additionally, quasar emission line profiles can vary from quasar to quasar, and can be shifted from the systemic redshift. This is especially true for high-ionization, broad emission lines like CIV, which can be blueshifted a few hundred km s^{-1} from low-ionization, broad emission lines like MgII which are often closer to the systemic redshift [55, 99]. Emission lines can also be broadened, and even asymmetric, for example Lyman-α absorption in the IGM can cause an asymmetry in the line profile [55, 88].

After the spectra are collected and processed by the DESI spectroscopic pipeline [59], they are classified and the redshifts are estimated by the redshift fitter code adopted by the DESI collaboration, Redrock [9]. Redrock is both a redshift fitter and classifier, and fits to pre-computed Principal Component Analysis (PCA) templates to spectra to determine the most probable class of the object (galaxy, quasar, star) and the best-fit redshift. The quasar spectral templates used by Redrock for EDR were adopted from eBOSS and are described in [17]. They were developed using a small number of spectra, and can not fully account for the variability of spectral features in quasar spectra. The performance of these templates on DESI EDR quasars is discussed in [6] and [18].

It was reported in [18] that there is a redshift-dependent bias in the eBOSS quasar templates likely stemming from the improper correction of the Lyman-α forest optical depth which introduces suppression in the forest that increases with redshift. This bias is present in the quasar catalogs used in this work since the eBOSS templates were used to produced the EDR redshifts. In section 4.6, we discuss mitigating this bias by accounting for the mean transmission of Lyman-α in the spectral templates used for redshift estimation.

We can utilize the Lyman-α forest-quasar cross-correlation to constrain quasar redshift errors due to its asymmetry along the line of sight. When measuring the cross-correlation as a function of the parallel and perpendicular components of the line of sight separation ($r_\parallel$ and

$r_\perp$, respectively), a positive offset from $r_\parallel = 0$, meaning the cross-correlation is shifted to a higher redshift than that of the quasar, indicates that quasar redshifts are being underestimated. As shown in [108], quasar redshift errors smear the BAO peak in the radial direction and cause unphysical correlations for small separations in $r_\perp$ that increase with increasing redshift errors. However, [108] also found that the position of the BAO peak is resilient to effects from quasar redshift errors.

In this work we measure and study the Lyman-α forest-quasar cross-correlation, focusing on scales less than $80\,h^{-1}$ Mpc. We begin in section 4.2, where we present and describe the sample of quasars and Lyman-α forests used in this analysis. We describe the method used to measure and fit the correlations in section 4.3. In section 4.4, we discuss validating our method with mocks. We present the cross-correlation and baseline fit results in section 4.5.1, we explore any redshift evolution of the redshift error parameter in section 4.5.2, and the impact of Broad Absorption Line regions in section 4.5.3. We address the redshift dependent bias on the quasar templates in section 4.6. Finally, we conclude in section 4.7 with a summary of this work and suggestions for future studies.

4.2 Data Sample

The data used in this paper consists of quasars from the DESI EDR [32] as well as data from the first two months of main survey observations (M2). The combination of EDR and M2 is hereafter referred to as EDR+M2. The data products from EDR are described in [32] and [59], and the spectra are publicly available [1]. The spectra from M2 will be publicly available with the year 1 data release. We present the quasar sample in 4.2.1 and the Lyman-α forest sample in 4.2.2.

---

[1] `https://data.desi.lbl.gov/public/edr/`

4.2.1 Quasar Sample

The quasar catalog was constructed following the logic in section 6.2 of [23], specifically figure 9. We briefly describe the method here.

The quasar catalog is produced using Redrock [9] and the two afterburner algorithms: a broad Magnesium II (MgII) line finder and a machine-learning based classifier QuasarNET [20, 48, 57]. Objects are first run through Redrock to determine both the class of the object (galaxy, quasar, star) and the best-fit redshift. Objects that are classified galaxy are then run through the MgII algorithm. If the MgII algorithm finds significant broad MgII emission, then their classification is changed to QSO and the redshift from Redrock remains unchanged. Any remaining objects are then run through QuasarNET. If QuasarNET classifies an object as QSO, Redrock is re-run for that object with the QuasarNET redshift as a prior. If neither of the three algorithms classify an object as QSO, then it is not included in the catalog. While the redshifts from QuasarNET are included in the catalog (as value-added content), the official redshift for each object comes from Redrock.

To finalize our catalog, we select only the objects that were targeted as quasars, using the classifications provided by the DESI target-selection pipeline [80]. Some of these objects were observed multiple times during EDR and M2 and therefore have multiple entries, but we want to keep only one observation per object in the quasar catalog. To select the best observation for the duplicated quasars, we first remove those that have a redshift warning flags set (i.e, those with a bad fit). If there are still repeat observations of the same quasar at this point, we select the observation with the highest TSNR2_LYA value. TSNR2_LYA, which is defined in section 4.14 of [59], is a measure related to the signal to noise ratio in the blue part of spectra for a given observation. We also remove any BAL quasars that were identified by the BALFinder [58] as having their absorption index (AI) > 0.

After these cuts, a total of 290,506 quasars are present in the quasar catalog. However, only

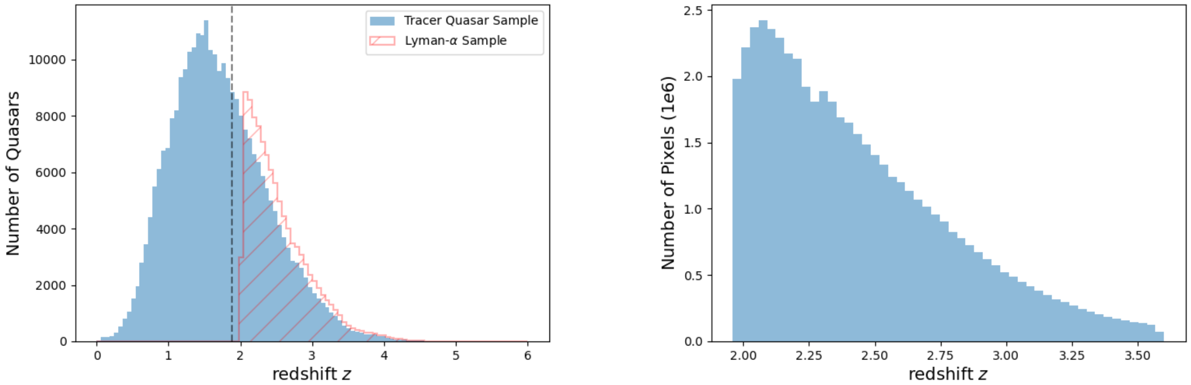

(a) Redshift distribution for the tracer quasar sample (without BALs) used in this paper. The red hatched histogram represents the Lyman-α forest sample. The dashed grey line represents the lower bound on the tracer quasar sample, $z = 1.88$.

(b) Redshift distribution of Lyman-α forest pixels output during the continuum fitting process for the baseline analysis.

Figure 4.1: Redshift and Lyman-α forest pixel distributions for the tracer quasar and Lyman-α forest samples used in this work.

the 106,861 quasars with redshift $z > 1.88$ will be included in the cross-correlation discussed in section 4.3.2. We refer to these quasars as tracer quasars or the tracer quasar catalog. Figure 4.1a shows the redshift distribution of the entire quasar sample with the dashed grey line representing this cutoff for the tracer quasar sample. The red hatched histogram shows the redshift distribution for the Lyman-α sample discussed in the next section.

4.2.2 Lyman-α Forest Sample

We use the same Lyman-α forest sample as described in [86]. We will briefly describe the sample here, but refer the reader to [86] for a more detailed description.

We define the Lyman-α forest as the region between the Lyman-β and Lyman-α emission lines at 1025.7 Å and 1215.67 Å, respectively. To reduce any contamination from the wings of those emission lines, we reduce the rest-frame wavelength range of all the Lyman-α forests to

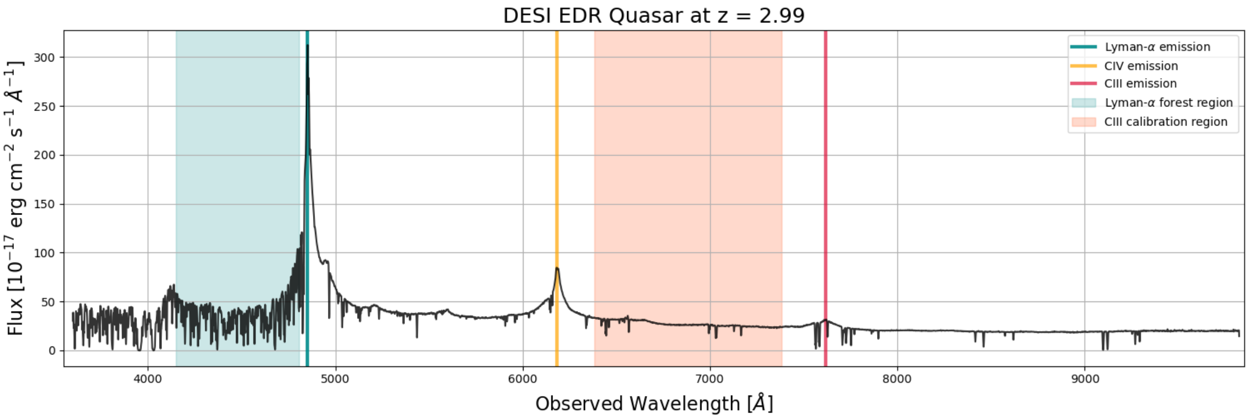

Figure 4.2: An example of a quasar spectrum from DESI EDR at redshift 2.99 and TARGETID = 39633362754732929. The observed Lyman-α emission line is shown in teal, CIV in orange and CIII] in red. The orange shaded region is the CIII calibration region, and the Lyman-α forest region is shaded in teal, both are used in the continuum fitting process in section 4.3.1. Redward of the Lyman-α emission are some absorption lines, likely from various metals.

1040 Å ¡ λ ¡ 1205 Å. An example quasar spectrum highlighting the Lyman-α forest is shown in figure 4.2. Other features highlighted are the CIV and semi-forbidden CIII emission lines. The region between these lines shaded in orange is used during the calibration step of the continuum fitting process discussed in section 4.3.1 and in [86].

The Lyman-α forest sample is created from the same quasar catalog described in section 4.2.1, but the BAL quasars are not excluded. We set a limit on the observed wavelength range of the Lyman-α forest between 3600 Å and 5772 Å. The lower limit is set to the lowest wavelength measured by the blue DESI spectrographs [59] and corresponds to a minimum Lyman-α pixel redshift of $z = 1.96$, meaning the lowest redshift a quasar can have is $z = 2.02$. The upper limit is set by the small number of high redshift quasars in EDR+M2. This limit corresponds to a maximum quasar redshift of $z = 4.29$ (with a corresponding maximum Lyman-α pixel redshift of $z = 3.75$).

With these redshift cuts, there are 109,900 valid Lyman-α forests from the quasar catalog. Prior to fitting the continuum (described in section 4.3.1), we first mask regions of the spectra that are contaminated. This contamination can come from sky lines, galactic absorption, BALs, and Damped Lyman Alpha (DLA) regions. We mask any DLA regions identified with the DLAFinder [109] and BAL regions identified with the BALFinder [58] of the quasar spectra. For the sky lines and galactic absorption, we mask four areas of the spectra: sky lines from [5570.5, 5586.7] Å; and the Ca H, and K lines from the Milky Way from [3967.3, 3971.0] Å and [3933.0, 3935.8] Å, respectively. We also perform a calibration using the CIII between 1600 ¡ λ_{RF} [Å] ¡ 1850, which is shaded in orange in figure 4.2. This calibration step follows the same process described in section 4.3.1 and in [86]. We require each forest to have a minimum length of 40 Å. Forests that are too short (don't have enough pixels), have low signal (¡ 0), or have problems fitting the continuum (negative continuum) will be rejected during the calibration and continuum fitting process (section 4.3.1). After these rejections, the final Lyman-α sample has 88,511 forests. Figure 4.1b shows the redshift distribution of Lyman-α pixels in the sample.

4.3 Method

We measure and model the cross-correlation of the Lyman-α forest with quasars following the method in [43, 56] and for the continuum fitting process we follow the method in [86]. We will briefly discuss the method for this analysis starting with the continuum fitting in section 4.3.1, calculating the cross-correlation function in section 4.3.2, the distortion and covariance matrices in section 4.3.3, and the model in section 4.3.4. We perform the calculations in sections 4.3.1-4.3.3 using picca[2], and we perform the modeling in section 4.3.4 using vega.[3]

---

[2] `https://github.com/igmhub/picca/`

[3] `https://github.com/andreicuceu/vega`

4.3.1 Measuring the Flux Transmission Field

We follow the method in [86] to measure the flux transmission field for the Lyman-α sample. We will briefly describe the method here but refer the reader to [86] for a more detailed description.

In this work, we adopt the same 0.8 Å linear pixel size used by the DESI spectroscopic pipeline [59] and other Lyman-α forest analyses using DESI EDR+M2 data [56, 86]. Previous analyses in eBOSS used logarithmic pixels [43]. We follow the method described in [86].

For each forest in each line of sight, q, we calculate the flux transmission field δ_{q} as a function of observed wavelength:

$$\delta_{\mathrm{q}}(\lambda) = \frac{f_{\mathrm{q}}(\lambda)}{\overline{F}(\lambda) C_{\mathrm{q}}(\lambda)} - 1. \tag{4.1}$$

Here, $f_{\mathrm{q}}(\lambda)$ is the observed flux, $C_{\mathrm{q}}(\lambda)$ is the unabsorbed quasar continuum, and $\overline{F}(\lambda)$ is the mean transmitted flux at a specific wavelength. To measure each delta field, we estimate the mean expected flux, $\overline{F}(\lambda) C_{\mathrm{q}}(\lambda)$, which is the product of the terms in the denominator in eq. 4.1. We assume it can be expressed according to:

$$\overline{F}(\lambda) C_{\mathrm{q}}(\lambda) = \overline{C}(\lambda_{\mathrm{RF}}) \left(a_{\mathrm{q}} + b_{\mathrm{q}} \frac{\Lambda - \Lambda_{\mathrm{min}}}{\Lambda_{\mathrm{max}} - \Lambda_{\mathrm{min}}} \right), \tag{4.2}$$

where $\Lambda \equiv \log \lambda$, $\overline{C}(\lambda_{\mathrm{RF}})$ is the estimate of the mean continuum for the considered quasar sample, and a_{q}, b_{q} are per-quasar parameters.

The estimated variance of the flux σ_{q}^2 depends on the noise from the DESI spectroscopic pipeline and the intrinsic variance of the Lyman-α forest (σ_{LSS}^2) and we model it as

$$\frac{\sigma_{\mathrm{q}}^2(\lambda)}{(\overline{F} C_{\mathrm{q}}(\lambda))^2} = \eta(\lambda) \tilde{\sigma}_{\mathrm{pip,q}}^2 + \sigma_{\mathrm{LSS}}^2, \tag{4.3}$$

where $\tilde{\sigma}_{\mathrm{pip,q}} = \sigma_{\mathrm{pip,q}}/\overline{F}C_{\mathrm{q}}(\lambda)$ and $\sigma_{\mathrm{pip,q}}$ is the spectroscopic pipeline estimate of the flux uncertainties. It is further modified by the correction, $\eta(\lambda)$, which accounts for inaccuracies in the spectroscopic pipeline noise estimation. In DESI $\eta(\lambda)$ ranges between 0.97 and 1.05 between 3600 Å and 5772 Å, respectively, and is generally close to 1 due to first performing a calibration using the CIII region. The mean continuum $\overline{C}(\lambda_{\mathrm{RF}})$, the function $\eta(\lambda)$, $\sigma_{\mathrm{LSS}}(\lambda)$, and the quasar parameters, a_{q} and b_{q}, are fit in an iterative process and stable values are obtained after about 5 iterations.

4.3.2 The Lyman-α Forest-Quasar Cross-Correlation

In this work we study the Lyman-α forest-quasar cross-correlation function. We require the use of the Lyman-α auto-correlation function to constrain some of the fit parameters (discussed in section 4.5). We use the Lyman-α forest auto-correlation results from [56] and, when necessary (in sections 4.4 and 4.5.3), run the auto-correlation following the method in [56]. The results of the cross-correlation are presented in section 4.5.1.

The separation between two tracers is determined both parallel and perpendicular to the line of sight, with $\vec{r} = (r_{\parallel}, r_{\perp})$. For two tracers i and j with redshift z_i and z_j, that are offset by an observed opening angle $\Delta\theta$, the comoving separation can be computed as

$$r_{\parallel} = [D_{\mathrm{c}}(z_{\mathrm{i}}) - D_{\mathrm{c}}(z_{\mathrm{j}})] \cos\left(\frac{\Delta\theta}{2}\right), \tag{4.4a}$$

$$r_{\perp} = [D_{\mathrm{m}}(z_{\mathrm{i}}) + D_{\mathrm{m}}(z_{\mathrm{j}})] \sin\left(\frac{\Delta\theta}{2}\right), \tag{4.4b}$$

where $D_{\mathrm{c}}(z) = c\int_0^z dz/H(z)$ is the comoving distance, D_{m} is the angular comoving distance, and $H(z)$ is the Hubble function. To use the comoving distance we have to assume a fiducial cosmology and we adopt the flat ΛCDM cosmology of Planck Collaboration et al. (2018) [85]. With this cosmology we have $D_{\mathrm{c}} = D_{\mathrm{m}}$. In the above equations, the two tracers are either two Lyman-α pixels for the auto-correlation or a Lyman-α pixel and a quasar for the cross-correlation. The redshift of a Lyman-α pixel is calculated as $z_{\mathrm{i}} = \lambda_{\mathrm{obs}}/\lambda_{\mathrm{Ly}\alpha} - 1$, where $\lambda_{\mathrm{Ly}\alpha} = 1215.67$ Å and the quasar redshift is given from the tracer quasar catalog described in section 4.2.1.

The cross-correlation of the Lyman-α forest with quasars is defined as

$$\xi(\vec{r}_{\mathrm{A}}) = \langle \delta_{\mathrm{Q}}(\vec{x})\delta(\vec{x} + \vec{r}_{\mathrm{A}})\rangle \approx \langle \delta(\vec{x}_{\mathrm{Q}} + \vec{r}_{\mathrm{A}})\rangle, \tag{4.5}$$

where $\delta_{\mathrm{Q}}(\vec{x})$ is the fluctuation of the number density in quasars, and $\vec{r} = (r_{\parallel}, r_{\perp})$ (with $r^2 = r_{\parallel}^2 + r_{\perp}^2$) for bin A. If we assume that quasars are shot-noise dominated, then the cross-correlation is just the average Lyman-α transmission around quasars at $\vec{x}_{\mathrm{Q}}$ [52].

For the Lyman-α-quasar cross-correlation we use the same estimator as previous studies [43, 50, 56]:

$$\xi_{\mathrm{A}} = \frac{\sum_{(\mathrm{i,j})\in \mathrm{A}} w_{\mathrm{i}} w_{\mathrm{j}} \delta_{\mathrm{i}}}{\sum_{(\mathrm{i,j})\in \mathrm{A}} w_{\mathrm{i}} w_{\mathrm{j}}}, \tag{4.6}$$

where i indexes a Lyman-α pixel and j a quasar, and δ_{i} is the flux transmission for the Lyman-α pixel defined in eq. 4.1. The weights w are defined in [56] and proportional to $(1+z)^{\gamma-1}$, where $\gamma = 1.44$ for quasars and 2.9 for a Lyman-α pixel. The sums are over all quasar-pixel pairs with separations that are within the bounds of bin A, with the exception of Lyman-α pixels from their own background quasar which are excluded. The bounds of bin A are defined in comoving coordinates and are determined based on the selected bin width.

The correlation is binned along and across the line of sight, but the cross-correlation itself is not symmetric (i.e, you can't swap indices i and j for δ_i in eq. 4.6). We define a positive separation along the line of sight when the quasar is in front of the Lyman-α pixel ($z_{qso} < z_{Ly\alpha}$) and likewise define a negative separation along the line of sight when the quasar is behind the Lyman-α pixel ($z_{qso} > z_{Ly\alpha}$). This asymmetry in the cross-correlation is what allows us to study systematic quasar redshift errors.

In this work we are studying small-scale effects on the cross-correlation, so we do not need to extend to large values of $r_\parallel$ and $r_\perp$, unlike the studies of BAO and the full-scale correlations in [43, 56]. We instead use a maximum separation of $80\,h^{-1}\,\mathrm{Mpc}$ in both $r_\parallel$ and $r_\perp$. For the cross-correlation, this corresponds to a minimum tracer quasar redshift of $z = 1.88$ given the minimum Lyman-α pixel redshift of $z = 1.96$ given in section 4.2.2.

Since our maximum separation in this study is $80\,h^{-1}\,\mathrm{Mpc}$, for the cross-correlation we restrict $r_\parallel \in [-80, 80]\ h^{-1}$ Mpc and $r_\perp \in [0, 80]\ h^{-1}$ Mpc. Previous measurements of 3D correlations to study BAO with eBOSS or DESI [43, 56] used a bin width of $4\,h^{-1}\,\mathrm{Mpc}$. Here, the focus of this paper is to measure a small-scale effect, we use a bin width of $1\,h^{-1}\,\mathrm{Mpc}$, along both transverse and longitudinal separations. This gives us 80 bins across the line of sight, 160 bins along the line of sight, and N = 80 × 160 = 12800 bins in total. We validate our choice to use a $1\,h^{-1}\,\mathrm{Mpc}$ bin width with mock data in section 4.4.

4.3.3 The Distortion and Covariance Matrices

We follow the same method as in [56] to estimate the covariance matrix for the cross-correlation. The covariance matrix is estimated by splitting the sky into s regions (according to HEALPix pixels) and then computing their weighted covariance. Assuming that correlations between regions are negligible, the covariance is written as

$$C_{\mathrm{AB}} = \frac{1}{W_{\mathrm{A}} W_{\mathrm{B}}} \sum_{\mathrm{s}} W_{\mathrm{A}}^{\mathrm{s}} W_{\mathrm{B}}^{\mathrm{s}} [\xi_{\mathrm{A}}^{\mathrm{s}} \xi_{\mathrm{B}}^{\mathrm{s}} - \xi_{\mathrm{A}} \xi_{\mathrm{B}}], \tag{4.7}$$

where A and B are two different bins of the correlation function ξ, $W = \sum_{\mathrm{s}} W^{\mathrm{s}}$, W^{s} is the summed weight for one of the regions s, and $\xi_{\mathrm{A}} = \sum_{\mathrm{s}} W^{\mathrm{s}}_{\mathrm{A}} \xi^{\mathrm{s}}_{\mathrm{A}} / W_{\mathrm{A}}$.

The covariance matrix is dominated by the diagonal elements (the variance) of the matrix. The estimates of off-diagonal elements are noisy, so they are modeled as a function of the difference of separation along the line of sight ($\Delta r_{\parallel} = |r^{\mathrm{A}}_{\parallel} - r^{\mathrm{B}}_{\parallel}|$) and across the line of sight ($\Delta r_{\perp} = |r^{\mathrm{A}}_{\perp} - r^{\mathrm{B}}_{\perp}|$) and then smoothed [43]. Correlation coefficients that have the same $\Delta r_{\parallel}, \Delta r_{\perp}$ are averaged.

Using the Lyman-α forest when estimating the quasar continuum biases the estimates of the delta field in eq. 4.1 because the measured delta for a given pixel is a combination of the absorption signals located at other pixels. This produces a distortion in the correlation functions that occurs throughout, but mainly appear for small $r_{\perp}$. The biases arise because

1. fitting the quasar parameters a_{q} and b_{q} biases the mean δ_{q} toward 0, and
2. fitting the mean transmitted flux, $\overline{F}$, biases the mean δ at each observed wavelength, $\overline{\delta(\lambda)}$, toward 0.

These effects can be modeled by transformations to $\delta_{\mathrm{q}}(\lambda)$. With the assumption that these transformations to δ_{q} are linear, the correlation function is distorted by a distortion matrix, $D_{\mathrm{AA'}}$, such that

$$\xi^{\mathrm{distorted}}_{\mathrm{A}} = \sum_{\mathrm{A'}} D_{\mathrm{AA'}} \xi^{\mathrm{true}}_{\mathrm{A'}}. \tag{4.8}$$

For the cross-correlation, the distortion matrix is calculated as

$$D^{\mathrm{cross}}_{\mathrm{AA'}} = \frac{\sum_{(\mathrm{i,k}) \in \mathrm{A}} w_{\mathrm{i}} \sum_{(\mathrm{j,k}) \in \mathrm{A'}} \eta_{\mathrm{ij}}}{\sum_{(\mathrm{i,k}) \in \mathrm{A}} w_{\mathrm{i}}}, \tag{4.9}$$

where η is the projection due to the distortion that occurs during the continuum fitting process and is defined in equation 3.3 of [56], and the weights w are defined in eq. 4.6.

When fitting the data, (described in section 4.3.4), the physical model of the correlation function is multiplied by the distortion matrix.

4.3.4 The Model of the Lyman-α Forest-Quasar Cross-correlation

This section presents the theoretical model for the auto- and cross-correlations. Though this work focuses on the cross-correlation, the auto-correlation is necessary to include during the fitting process as it helps break degeneracies between parameters.

In this model, the expected measured (distorted) cross-correlation in the $(r_{\parallel},\, r_{\perp})$ bin A is related to the theoretical (true) correlation by the distortion matrix as shown in eq. 4.8. The theoretical cross-correlation, $\xi^{\mathrm{qf,th}}$, can be broken down into the sum of its components:

$$\xi^{\mathrm{qf,th}} = \xi^{\mathrm{Ly}\alpha\times\mathrm{QSO}} + \sum_{\mathrm{a}} \xi^{\mathrm{QSO}\times\mathrm{a}} + \xi^{\mathrm{TP}}. \tag{4.10}$$

Here, the first term gives the contribution from the cross-correlation between the Lyman-α forest and quasars, the second term gives the contribution from the cross-correlation between quasars and other absorbers, like metals and high column density systems (HCDs), in the Lyman-α region, and the last term gives the contributions from the transverse proximity (TP) effect, which is the effect of radiation from the quasar on the nearby surrounding gas. We describe these terms in depth throughout this section and the parameters of this model are described in table 4.5.

The Lyman-α-QSO contribution to the correlation function is derived from the Fourier transform of the tracer biased power spectrum, $P(\mathbf{k}, z)$, which is written as

$$P(\mathbf{k}, z) = b_{\mathrm{i}}(z) b_{\mathrm{j}}(z)(1 + \beta_{\mathrm{i}}\mu_{\mathrm{k}}^2)(1 + \beta_{\mathrm{j}}\mu_{\mathrm{k}}^2) P_{\mathrm{QL}}(\mathbf{k}, z) F_{\mathrm{NL}}(\mathbf{k}) G(\mathbf{k}), \tag{4.11}$$

where $\mathbf{k}$ is the wavenumber with modulus k and $\mu_{\mathrm{k}} = k_{\parallel}/k$. The bias and linear redshift-space distortion parameters, $b_{\mathrm{i,j}}(z)$ and $\beta_{\mathrm{i,j}}$, are for tracer i or j. G is a correction that accounts for the averaging of the correlation function binning and F_{NL} accounts for the non-linear effects on small scales (large $\mathbf{k}$). P_{QL} is the quasi-linear matter power spectrum defined in eq. 4.16. For the auto-correlation, $i = j$ and the only tracer is Lyman-α absorption. In this work, we are concerned with the cross-correlation, $i \neq j$ and the two tracers are Lyman-α absorption and quasars.

In eq. 4.11, the bias b and redshift-space distortion β parameters for each tracer i, j appear with the standard Kaiser factor: $b_{\mathrm{i,j}}(z)(1+\beta_{\mathrm{i,j}}\mu_{\mathrm{k}}^2)$ [68]. The fit of the cross-correlation is only sensitive to the product of the quasar and Lyman-α biases. The quasar bias b_{q} is redshift dependent and is given by

$$b_{\mathrm{q}}(z) = b_{\mathrm{q}}(z_{\mathrm{eff}}) \left(\frac{1+z}{1+z_{\mathrm{eff}}} \right)^{\gamma_{\mathrm{q}}}, \tag{4.12}$$

where z_{eff} is the effective redshift of the sample and $\gamma_{\mathrm{q}} = 1.44$ [41]. Following the analysis of [56] we allow b_{q} to remain free in the fit. On the other hand, the quasar redshift-space distortion (RSD) parameter, β_{q}, is not a free parameter. It is related to the quasar bias b_{q} by:

$$\beta_{\mathrm{q}} = \frac{f}{b_{\mathrm{q}}}, \tag{4.13}$$

where $f = 0.9703$ is the linear growth rate of structure in our fiducial cosmology. We then derive the value of β_{q} from the result of b_{q}.

We assume that the Lyman-α bias parameter, $b_{\mathrm{Ly\alpha}}$, is redshift dependent but use the approximation that the Lyman-α RSD parameter, $\beta_{\mathrm{Ly\alpha}}$, is redshift independent. Following

[56], $b_{\mathrm{Ly}\alpha}$ is given by

$$b_{\mathrm{Ly}\alpha}(z) = b_{\mathrm{Ly}\alpha}(z_{\mathrm{eff}}) \left(\frac{1+z}{1+z_{\mathrm{eff}}} \right)^{\gamma_{\mathrm{Ly}\alpha}}, \tag{4.14}$$

with $\gamma_{\mathrm{Ly}\alpha} = 2.9$ [79]. We allow $b_{\mathrm{Ly}\alpha}$ and $\beta_{\mathrm{Ly}\alpha}$ to remain free in the fit.

The Lyman-α absorption contains contributions from both the inter-galactic medium (IGM) and high-column-density (HCD) systems. HCD absorbers, such as Damped Lyman Alpha, trace the underlying density field. When these HCD systems are correctly identified and the appropriate parts of the absorption region are properly masked and modeled, they will have no effect on the measured correlation functions. However, if these systems are left unidentified, they will affect the measured correlation function as a broadening/smearing in the radial direction. Following the method in [51], this effect introduces a $k_{\parallel}$ dependence to the effective bias and can be modeled as

$$\begin{aligned} b'_{\mathrm{Ly}\alpha} &= b_{\mathrm{Ly}\alpha} + b_{\mathrm{HCD}} F_{\mathrm{HCD}}(k_{\parallel}), \\ b'_{\mathrm{Ly}\alpha}\beta'_{\mathrm{Ly}\alpha} &= b_{\mathrm{Ly}\alpha}\beta_{\mathrm{Ly}\alpha} + b_{\mathrm{HCD}}\beta_{\mathrm{HCD}} F_{\mathrm{HCD}}(k_{\parallel}), \end{aligned} \tag{4.15}$$

where $(b_{\mathrm{Ly}\alpha}, \beta_{\mathrm{Ly}\alpha})$ and $(b_{\mathrm{HCD}}, \beta_{\mathrm{HCD}})$ are the bias and redshift space distortion parameters associated with the IGM and HCD systems. Following [43], we use $F_{\mathrm{HCD}} = \exp(-L_{\mathrm{HCD}} k_{\parallel})$, which is approximated from the results in [93]. L_{HCD} is the length scale for unmasked HCDs, and is degenerate with other parameters. For this work, we fix $L_{\mathrm{HCD}} = 10\,h^{-1}\,\mathrm{Mpc}$ and allow b_{HCD} to be free in the fit. We fix $\beta_{\mathrm{HCD}} = 0.5$.

While this work focuses on comoving separations smaller than the BAO scale, for consistency with other analyses [34, 56], we model the quasi-linear matter power spectrum, $P_{\mathrm{QL}}(\mathbf{k}, z)$, as the sum of a smooth and peak components with an empirical anisotropic damping applied to the BAO peak component:

$$P_{\rm QL}(\mathbf{k}, z) = P_{\rm sm}(k, z) + A_{\rm peak} \exp\left[-\frac{k_\parallel^2\Sigma_\parallel^2 + k_\perp^2\Sigma_\perp^2}{2}\right] P_{\rm peak}(k, z). \tag{4.16}$$

$P_{\rm sm}$ in eq. 4.16 is derived from the linear power spectrum $P_{\rm L}(k, z)$ via the side-band technique described in [74]. The redshift dependent linear power spectrum, $P_{\rm L}$, is derived from CAMB [77], and we then define $P_{\rm peak} = P_{\rm L} - P_{\rm sm}$. The BAO peak is affected by non-linear broadening [44] and is corrected for by introducing the parameters $(\Sigma_\parallel, \Sigma_\perp)$. $\Sigma_\parallel$ is related to $\Sigma_\perp$ and the growth rate such that

$$\frac{\Sigma_\parallel}{\Sigma_\perp} = 1 + f, \tag{4.17}$$

where $f = 0.9703$ is the linear growth rate of structure in our fiducial cosmology. Given that we do not fit the BAO peak in this work, we fix $(A_{\rm peak},\ \Sigma_\parallel,\ \Sigma_\perp) = (1,\ 6.37\,h^{-1}\,\rm Mpc,\ 3.24\,h^{-1}\,\rm Mpc)$ [56].

$F_{\rm NL}$ in equation 4.11 corrects for additional effects at small scales. In the auto-correlation these are thermal broadening, peculiar velocities, and nonlinear growth structure, parameterized according to equation 3.6 in [8]. For the cross-correlation the most important small-scale correction is due to quasar velocities and the precision of quasar redshift measurements. Following [42, 56], we model this using the Lorentz-damping form:

$$F_{\rm NL}^{\rm cross}(k_\parallel) = \frac{1}{\sqrt{1 + (k_\parallel \sigma_{\rm v})^2}}, \tag{4.18}$$

where $\sigma_{\rm v}$ is a free parameter that describes the precision of quasar redshift measurements. Alternative models for $F_{\rm NL}$ use a Gaussian form.

The last term in eq. 4.11, $G(\mathbf{k})$, accounts for the effects of the binning of the correlation function on the $(r_\parallel, r_\perp)$ separation grid. Assuming the distribution in each bin is homogeneous, and following the method used in [12],

$$G(\mathbf{k}) = \text{sinc}\left(\frac{R_{\parallel}k_{\parallel}}{2}\right)\text{sinc}\left(\frac{R_{\perp}k_{\perp}}{2}\right), \tag{4.19}$$

where $R_{\parallel}$ and $R_{\perp}$ are the scales of the smoothing, i.e, are the radial and transverse widths of the bins, respectively. In this work we focus on bin widths of $1\,h^{-1}$ Mpc for both $R_{\parallel}$ and $R_{\perp}$, but validate the choice between $1\,h^{-1}$ Mpc and $4\,h^{-1}$ Mpc in section 4.4.

The next component that contributes to the model cross-correlation in eq. 4.10 is the sum over the non-Lyman-α absorbers, or metals. The power spectrum for the cross-correlation with metals has the same form as that used for the Lyman-α-quasar cross-correlation, though it is simplified by neglecting the effect of HCDs. Because there is little absorption by metals, it is further simplified by not separating the smooth and peak components. It is however, more complicated due to the fact that the ($r_{\parallel}$, $r_{\perp}$) bins in the correlation correspond to an observed $(\Delta\theta, \Delta\lambda)$ calculated assuming that the absorption is due to the Lyman-α transition.

This causes a shift in the model correlation function, and the contribution of each absorber is maximized in the ($r_{\parallel}$, $r_{\perp}$) bin that corresponds to vanishing physical separation. For Lyman-α absorption this corresponds to ($r_{\parallel}$, $r_{\perp}$) = (0,0). For the other absorbers, this maximum occurs at $r_{\perp} = 0$ and $r_{\parallel} \approx \frac{c}{H(z)}(1+z)(\lambda_{\mathrm{m}} - \lambda_{\mathrm{Ly}\alpha})/\overline{\lambda}$, where $\overline{\lambda}$ is the mean value between the Lyα and metal absorption [56]. The values of the $r_{\parallel}$ separations for the metal absorbers considered in this work are given in table 4.1.

The shifted-model correlation function is calculated with respect to the unshifted-model correlation function, ξ^{mn}, for each absorber pair (m, n) by introducing a metal matrix M_{AB} as in [16]:

$$\xi^{\mathrm{mn}}_{\mathrm{A}} \longrightarrow \sum_{\mathrm{B}} M_{\mathrm{AB}}\xi^{\mathrm{mn}}(r_{\parallel}(B), r_{\perp}(B)), \tag{4.20}$$

Transition	$\lambda_{\rm m}$ [Å]	$\lambda_{\rm m}/\lambda_{\rm Ly\alpha}$	Lyman-α-m $r_{\parallel}$ [h^{-1} Mpc]
SiII(1260)	1260.4	1.036	+104
SiIII(1207)	1206.5	0.992	-22
SiII(1193)	1193.3	0.981	-55
SiII(1190)	1190.4	0.979	-62

Table 4.1: Metal transitions seen in the IGM and that are also present in the Lyman-α forest-quasar cross correlation for $r_{\parallel} \in [-80, 80]$ h^{-1} Mpc. The second column gives the rest-frame wavelength of the transition in Angstroms. The third column is the ratio between the wavelengths of the metal transition and the Lyman-α transition (1215.67 Å). The last column gives the error in comoving distance when a metal absorption is incorrectly assumed to be Lyman-α absorption at $z = 0$.

where $M_{\rm AB}$, the metal matrix, is defined as

$$M_{\rm AB} = \frac{1}{W_{\rm A}} \sum_{\rm (m,n)\in A,(m,n)\in B} w_{\rm m} w_{\rm n}. \tag{4.21}$$

Here, $W_{\rm A} = \sum_{\rm (m,n)\in A} w_{\rm m} w_{\rm n}$ and $w_{\rm m}, w_{\rm n}$ are the weights for each absorber and are redshift dependent such that $w \propto (1+z)^{\gamma}$. $(m,n) \in A$ refers to separations calculated using the reconstructed redshift of the absorber pair and $(m,n) \in B$ refers to separations computed using the redshifts $z_{\rm m}$ and $z_{\rm n}$ of the absorber pair (m,n).

In the fits to the data each metal species has its own individual bias parameters (b, β). Since the correlations are only visible in $(r_{\parallel},\, r_{\perp})$ bins that correspond to small physical separations and the amplitudes for the SiII and SiIII metal species are determined by the excess correlations, we do not have enough signal to determine the (b, β) parameters separately. As in previous works ([42, 43]), we fix $\beta = 0.5$ for all metal species. Since we are using the auto-correlation from [56] we include correlations from the four metal species given in table 4.1 in the correlations.

The last term in eq. 4.10 is due to the transverse proximity effect. In the area surrounding a quasar, there is significantly less Lyman-α absorption because the radiation emitted from the quasar dominates over the UV background and increases the ionization fraction of the surrounding gas, thus making it more transparent to Lyman-α photons. The Lyman-α absorption of a background quasar will decrease in strength at the redshift of the foreground quasar when the Lyman-α forest is close to the quasar line of sight. This will therefore affect the correlation between quasars and the Lyman-α forest. As in [56], we model this effect in the correlation with

$$\xi^{\mathrm{TP}} = \frac{\xi_0^{\mathrm{TP}}}{r^2} \exp\left[\frac{-r}{\lambda_{\mathrm{UV}}}\right], \tag{4.22}$$

where r is the comoving separation in units of h^{-1} Mpc, λ_{UV} =300 h^{-1} Mpc [94], and ξ_0^{TP} is an amplitude that will be fit.

Systematic errors on the measurement of the quasar redshift can cause a shift in the model estimation of the correlation function in $r_\parallel$. To account for this, we allow for a shift of the absorber-quasar separation in the $r_\parallel$ direction

$$\Delta r_\parallel = r_{\parallel,\mathrm{true}} - r_{\parallel,\mathrm{measured}}. \tag{4.23}$$

The shift is mostly due to systematic quasar redshift errors. However, any asymmetries in $r_\parallel$ will also affect $\Delta r_\parallel$. The model of the cross-correlation function is not symmetric about $r_\parallel$ due to the contribution of metal absorptions and the variation of mean redshift with $r_\parallel$. The continuum-fitting distortion also introduces an asymmetry in $r_\parallel$. [75] has showed that while $\Delta r_\parallel$ is sensitive to relativistic effects, they are small. We do not model any relativistic effects in this work as [15] showed that they are partially degenerate with $\Delta r_\parallel$.

4.4 Validation with Mock Data

To ensure that the choice of bin width does not introduce any biases to our analysis, and especially to the two redshift error parameters $\Delta r_\parallel$ and σ_{v}, we run our tests using mock data for three different cross-correlation bin widths: $1\,h^{-1}\,\mathrm{Mpc}$, $2\,h^{-1}\,\mathrm{Mpc}$, and $4\,h^{-1}\,\mathrm{Mpc}$. We follow the same method described in section 4.3, however we do not need to perform the calibration step on mock data (section 4.3.1). For the cross-correlation, we still restrict $r_{\parallel}$, $r_{\perp} \in [-80, 80]\,h^{-1}\,\mathrm{Mpc}$. For the $2\,h^{-1}\,\mathrm{Mpc}$ bin width, this gives 80 bins along the line of sight, 40 bins across the line of sight and N = 3,200 bins in total. For the $4\,h^{-1}\,\mathrm{Mpc}$ bin width, this gives 40 bins along the line of sight, 20 bins across the line of sight, and N = 800 bins in total. Since the auto-correlation doesn't help to constrain redshift errors we choose to follow the setup from [56] as we use the auto-correlations from [56] in section 4.5. The free and fixed parameters are described in table 4.5 in appendix 4.8.

In this work we use the mocks described in [60]. There are 10 realizations of Saclay [47] mocks that contain signal from the Lyman-α forest as well as contamination from DLAs, BALs, and metals, which most closely resembles the data from EDR+M2. Like in our baseline analysis, we mask the BAL and DLA regions during the continuum fitting process, and we remove any BAL quasars from the tracer quasar catalog. Each mock has approximately 118,000 objects in the catalog after BAL removal.

We present the results of the cross-correlation and best-fit model for each mock for two $r_{\perp}$ slices ($r_{\perp} \in$ [4,8] h^{-1} Mpc and $r_{\perp} \in$ [20,32] h^{-1} Mpc) in figure 4.3. The data and model are averaged across the $r_{\perp}$ slices for each mock. There are 4 times fewer points in the bottom row of figure 4.3 compared to the top row due to the bin width being 4 times larger. There is a bump in the correlations around $r_{\parallel} \approx -60\,h^{-1}\,\mathrm{Mpc}$ that likely corresponds to the effects from SiII λ1193 and λ1190 metal lines, which appear in the correlations as given in table 4.1. This bump is not as prominent in the larger $r_{\perp}$ slices as the metals have the largest effect at $r_{\perp} = 0$. There does not appear to be a shift from 0 in $r_{\parallel}$, as the center of the peaks corresponds with the dashed grey line at $r_{\parallel} = 0$.

The two parameters of interest in our model that describe redshift errors are $\Delta r_{\parallel}$ and σ_{v}. $\Delta r_{\parallel}$ describes the shift of the cross-correlation due to systematic redshift errors in quasars along

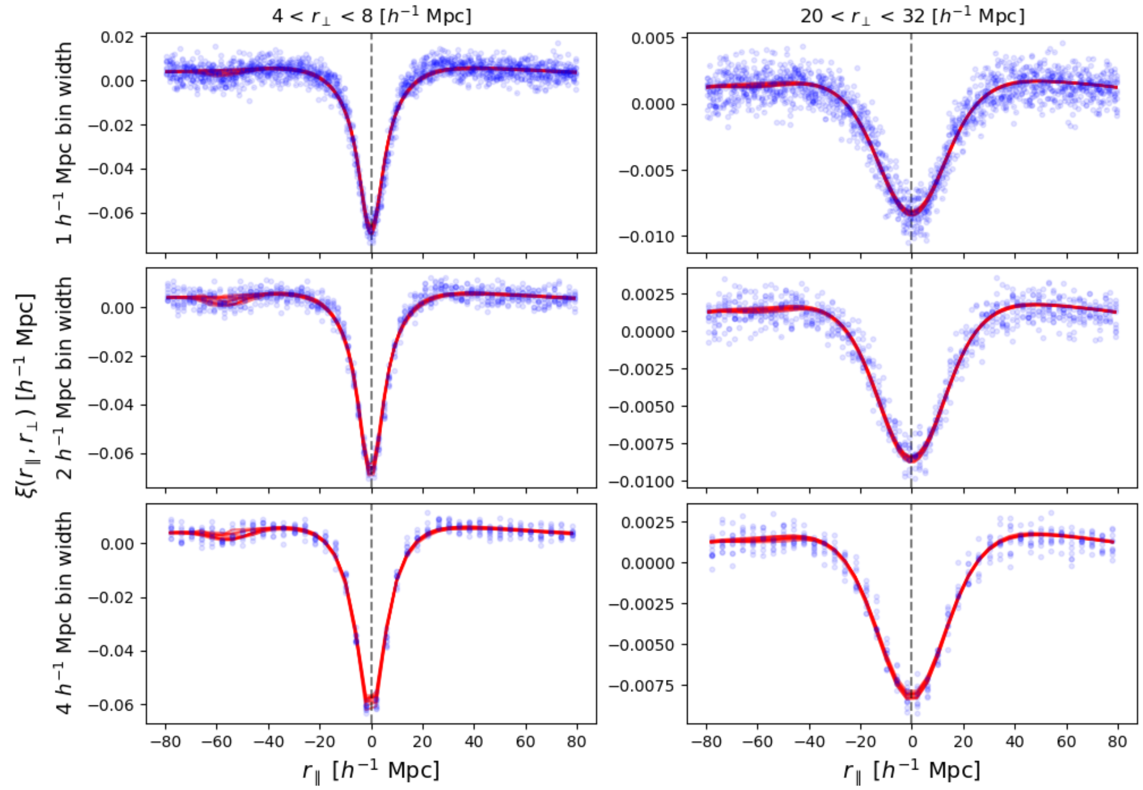

Figure 4.3: Results for 10 different realizations of mocks comparing the correlation function to the best-fit model. The data (blue points) and model (red lines) are averaged across $r_\perp \in [4,8]$ (left column) and $r_\perp \in [20,32]$ (right column). We compare the different bin widths studied in this analysis with $1\,h^{-1}$ Mpc on the top row, $2\,h^{-1}$ Mpc in the middle, and $4\,h^{-1}$ Mpc on the bottom row. The dashed grey line represents $r_\parallel = 0$.

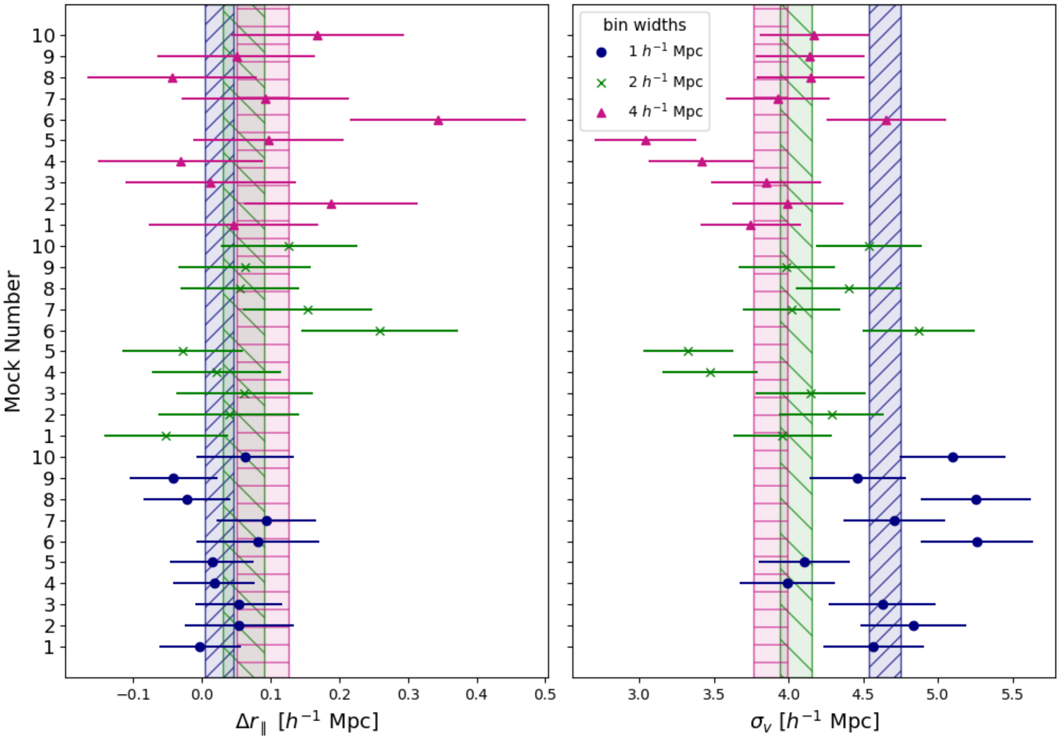

Figure 4.4: Results for 10 different realizations of mocks comparing the redshift error parameters, $\Delta r_{\parallel}$ (left) and σ_{v} (right) for the three different bin widths being studied: $1\,h^{-1}$ Mpc (blue dots), $2\,h^{-1}$ Mpc (green x's), and $4\,h^{-1}$ Mpc (pink triangles). The hatched shaded regions are showing the weighted average value + error for all 10 mocks.

the $r_\parallel$ direction. σ_v measures the radial velocity smearing due to random redshift errors and non-linear velocities. This is often represented as the rms velocity dispersion from a Lorentz damping factor [42, 82]. Here, a smaller value for σ_v means the redshift measurements are more accurate.

The mocks studied here do not have any systematic errors added to the quasar redshift so we expect $\Delta r_\parallel \sim 0$. The true value of σ_v is known and we do not expect it to be 0, as the mocks include non-linear effects. The results for these parameters for each mock and each bin width tested are shown in figure 4.4. The weighted average across all mocks is shown by the hatched shaded regions. For the $1\,h^{-1}\,\mathrm{Mpc}$ bin width: $\Delta r_\parallel = 0.039 \pm 0.021\ h^{-1}$ Mpc and $\sigma_\mathrm{v} = 4.64 \pm 0.11\ h^{-1}$ Mpc. For the $2\,h^{-1}\,\mathrm{Mpc}$ bin width: $\Delta r_\parallel = 0.079 \pm 0.030\ h^{-1}$ Mpc and $\sigma_\mathrm{v} = 4.05 \pm 0.11\ h^{-1}$ Mpc. For the $4\,h^{-1}\,\mathrm{Mpc}$ bin width: $\Delta r_\parallel = 0.10 \pm 0.04\ h^{-1}$ Mpc and $\sigma_\mathrm{v} = 3.88 \pm 0.11\ h^{-1}$ Mpc. The χ^2 values averaged over all mocks are 1.023 for the $1\,h^{-1}\,\mathrm{Mpc}$ bin width, 1.022 for the $2\,h^{-1}\,\mathrm{Mpc}$ bin width, and 1.009 for the $4\,h^{-1}\,\mathrm{Mpc}$ bin width, which all indicate a good fit.

Results for $\Delta r_\parallel$ with different bin widths are in good agreement with each other. They are also consistent with the true value of $\Delta r_\parallel = 0$, although we cannot rule out a small systematic uncertainty as large as $0.1\,h^{-1}\,\mathrm{Mpc}$. The results for σ_v are not consistent across the different bin widths. This is likely because the true value of σ_v in the mocks is too small to measure with the $4\,h^{-1}\,\mathrm{Mpc}$ bin width. The mocks have a resolution of $2.5\,h^{-1}\,\mathrm{Mpc}$ - which means we would need to additionally model the effect of resolution for the 1 and $2\,h^{-1}\,\mathrm{Mpc}$ bin widths. To test that we can recover the true value for σ_v, regardless of bin width, we add Gaussian random errors with $\sigma = 10\,h^{-1}\,\mathrm{Mpc}$ to the redshifts in the quasar catalogs. We then perform the continuum fitting process and calculate and fit the correlations for each mock. We take the weighted average across all 10 mocks and find $\sigma_\mathrm{v} = 12.93 \pm 0.25\ h^{-1}$ Mpc, $12.12 \pm 0.25\ h^{-1}$ Mpc, and $11.14 \pm 0.24\ h^{-1}$ Mpc for the 1, 2, and $4\,h^{-1}\,\mathrm{Mpc}$ bins, respectively. The increased values show that we can recover the correct value for σ_v.

Overall, the $1\,h^{-1}\,\mathrm{Mpc}$ bin widths do not appear to cause any biases in $\Delta r_{\parallel}$ larger than $0.1\,h^{-1}\,\mathrm{Mpc}$ when compared with the $2\,h^{-1}\,\mathrm{Mpc}$ and $4\,h^{-1}\,\mathrm{Mpc}$ bin widths. Since the larger $4\,h^{-1}\,\mathrm{Mpc}$ bins will smooth out any small-scale features from systematic redshift errors, we will present results on the EDR+M2 data in section 4.5 using a $1\,h^{-1}\,\mathrm{Mpc}$ bin width.

4.5 Results

In this section we present the results of this analysis using the auto-correlation from [56] and the cross-correlation measured from the data described in section 4.2 and using the methodology described in section 4.3. When necessary, we re-run the auto-correlation following the method in [56]. We present the cross-correlation and best-fit model for the baseline configuration in section 4.5.1. The baseline configuration masks both BAL and DLA regions of the quasar spectra during the continuum fitting process, and BALs are removed from the tracer quasar catalog. We explore the dependence on quasar redshift in section 4.5.2 and we discuss the effect of including and using updated redshifts for BALs in section 4.5.3. All correlations and fits are calculated and measured using a $1\,h^{-1}\,\mathrm{Mpc}$ bin width. Again, in this study we adopt the flat ΛCDM cosmology of Planck2018 [85].

4.5.1 Cross-correlation and Baseline Fit Results

The measured Lyman-α forest and quasar cross-correlation and the result for the baseline fit are presented in figure 4.5. We show the average of the correlation and model in each $r_{\perp}$ slice listed. The correlations have a lower amplitude for larger $r_{\perp}$ slices and therefore appear noisier. The model for the baseline fit is calculated jointly using the auto- and cross-correlations and has 13 free parameters. The values for the fixed parameters used in this model are presented in table 4.5 in Appendix 4.8.

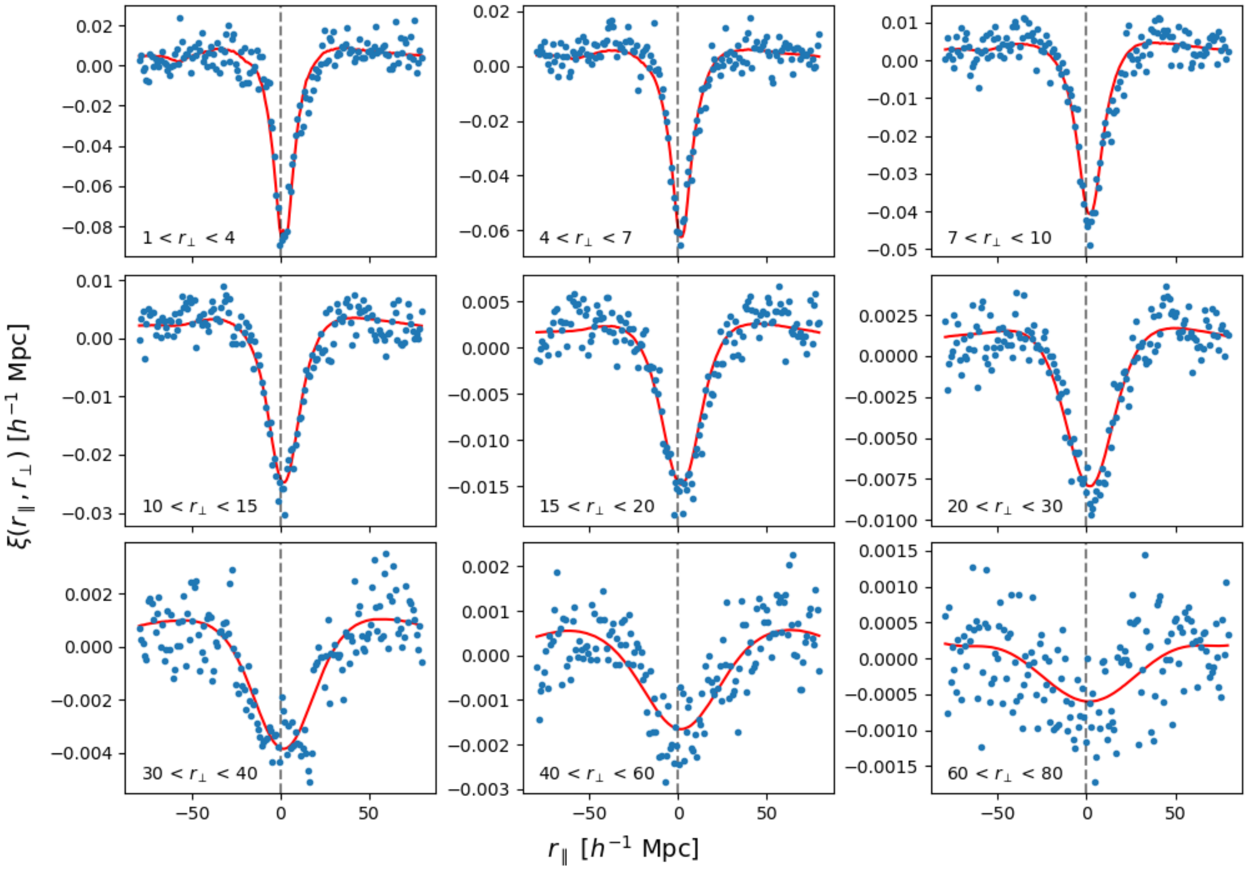

Figure 4.5: Measured Lyman-α forest and quasar cross-correlation (blue points) and resulting best-fit model for the baseline fit (red line). Both the correlation and the model are averaged in slices of $r_\perp$ and the $r_\perp$ slices (in h^{-1} Mpc) are shown in the lower left of each subplot. The dashed grey line represents $r_\parallel = 0$. Seen in all $r_\perp$ slices is a shift of the correlation and model in the positive $r_\parallel$ direction, which is consistent with our results for $\Delta r_\parallel$.

Parameter	Baseline	BAL	ZBAL
No. quasars	106,861	128,026	127,989
$b_{\mathrm{Ly}\alpha}$	-0.106 ± -0.023	-0.053 ± 0.011	-0.048 ± 0.009
$\beta_{\mathrm{Ly}\alpha}$	1.8 ± 0.4	3.7 ± 0.7	4.0 ± 0.7
$10^3 b_{\eta,\mathrm{SiII(1190)}}$	-2.8 ± 0.9	-2.6 ± 0.8	-2.1 ± 1.0
$10^3 b_{\eta,\mathrm{SiII(1193)}}$	-0.3 ± 1.0	-0.0 ± 1.3	-0.0 ± 1.0
$10^3 b_{\eta,\mathrm{SiIII(1207)}}$	-2.6 ± 0.9	-1.9 ± 0.9	-1.2 ± 0.9
$10^3 b_{\eta,\mathrm{SiII(1260)}}$	-2.7 ± 1.2	-3.9 ± 1.6	-4.9 ± 1.7
b_{HCD}	-0.051 ± 0.008	-0.054 ± 0.010	-0.052 ± 0.011
b_{q}	3.1 ± 0.4	4.1 ± 0.4	4.4 ± 0.5
$\Delta r_{\parallel}$ (h^{-1}Mpc)	-1.94 ± 0.15	-1.84 ± 0.13	-1.90 ± 0.11
σ_{v} (h^{-1}Mpc)	5.8 ± 0.5	7.3 ± 0.6	7.0 ± 0.6
ξ_0^{TP}	0.29 ± 0.05	0.08 ± 0.024	0.082 ± 0.023
$10^4 A_{\mathrm{inst}}$	2.28 ± 0.31	1.95 ± 0.27	1.90 ± 0.27
χ^2	1.036	1.042	1.037
z_{eff}	2.34	2.34	2.35

Table 4.2: Results of the fits for the baseline, BAL, and the ZBAL configurations. The number of quasars above $z = 1.88$ in each catalog is given. In all fits the BAO parameters are fixed at 1.0. The rest of the parameters are allowed to float in each fit and are described in 4.5 in appendix 4.8. Each fit has 11,644 data bins, 13 free parameters and we also list the effective redshift, z_{eff}. Since each fit is a joint fit of the auto- and cross-correlations, we list the χ^2 value given for the joint fit.

We present the results of the baseline fit in the first column in table 4.2. The baseline fit has a joint χ^2 value that corresponds to essentially zero probability. This is likely due to our model failing at small scale separations. We re-fit our model, increasing the minimum separation to $5\,h^{-1}$ Mpc and $10\,h^{-1}$ Mpc to check the results of the χ^2 values. We found a very minimal improvement in χ^2 values and a worsening of $\Delta r_{\parallel}$ values. We therefore decide to keep the minimum separation in our fit at $0\,h^{-1}$ Mpc and leave for future studies any further tests of the model on χ^2 values.

We find $\Delta r_{\parallel} = -1.94 \pm 0.15$ h^{-1} Mpc and $\sigma_{\mathrm{v}} = 5.8 \pm 0.5$ h^{-1} Mpc. Comparing these results to table 1 of [56], we find that σ_{v} is within 1.0σ from the value reported in [56]. Our result for $\Delta r_{\parallel}$ is also consistent within 1.5σ with [56], while our fit value for ξ_0^{TP} is 2.0σ with respect to the results reported in [56]. These differences are likely due to our smaller bin width, and the different ranges in $r_{\parallel}$ and $r_{\perp}$ used.

A negative value for $\Delta r_{\parallel}$ means the measured cross-correlation is shifted in the positive $r_{\parallel}$ direction, which is seen in all 9 $r_{\perp}$ slices in figure 4.5. Based on our definition of a positive separation, i.e, when the quasar is in front of the Lyman-α pixel, this indicates that the estimated quasar redshifts are less than the true quasar redshifts.

Our initial thought for this discrepancy is the disappearance of the MgII emission line from quasar spectra above redshift $z \approx 2.5$. The MgII line, a reliable indicator of systemic redshift [50, 61], is located beyond the observable range of the DESI spectrographs at these redshifts. We therefore rely on the high ionization broad lines, which often display significant velocity shifting [99], to obtain redshift estimates at $z > 2.5$. This is also suggested by [23], who report a "kink" at $z \sim 2.5$ when comparing the redshift estimates from DESI to those from SDSS (their figure 16). However, this is unlikely the cause of the "kink" due to the observable range of the BOSS spectrographs being very similar to DESI [104], as eBOSS would lose access to the MgII line at similar redshifts to DESI.

The apparent underestimation of DESI redshifts persisted when updating the quasar templates in Redrock for processing the DESI year one quasar sample [18]. In section 4.6, we discuss the improvements in redshift performance for DESI year 1 data at $z > 2$ when using an updated version of Redrock and quasar templates that properly model Lyman-α optical depth.

4.5.2 Dependence on Quasar Redshift

We test and study here the evolution and dependence of the parameters $\Delta r_{\parallel}$ and σ_{v} on quasar redshift to investigate more in depth the cause of the measured biases. We split the tracer quasar sample described in section 4.2 into four redshift bins: z1: $z \leq 2.2$, z2: $2.2 < z \leq 2.5$, z3: $2.5 < z \leq 2.8$, and z4: $z > 2.8$. As a reminder, quasars with redshift $z < 1.88$ will not contribute to the correlation as the separation will be larger than our

Parameter	z1	z2	z3	z4
No. quasars	41,688	27,958	17,407	19,808
Redshift range	$z \leq 2.2$	$2.2 < z \leq 2.5$	$2.5 < z \leq 2.8$	$z > 2.8$
$b_{\mathrm{Ly}\alpha}$	-0.085 ± 0.010	-0.117 ± 0.009	-0.160 ± 0.011	-0.216 ± 0.015
$\beta_{\mathrm{Ly}\alpha}$	1.77 ± 0.21	1.63 ± 0.17	1.48 ± 0.16	1.45 ± 0.15
$10^3 b_{\eta,\mathrm{SiII(1190)}}$	-3.6 ± 1.0	-2.6 ± 1.0	-3.2 ± 1.1	-3.4 ± 1.2
$10^3 b_{\eta,\mathrm{SiII(1193)}}$	-0.9 ± 0.9	-1.3 ± 1.0	-1.4 ± 1.1	-1.5 ± 1.2
$10^3 b_{\eta,\mathrm{SiIII(1207)}}$	-3.9 ± 0.9	-2.6 ± 0.9	-3.8 ± 1.0	-4.2 ± 1.2
$10^3 b_{\eta,\mathrm{SiII(1260)}}$	-2.8 ± 1.1	-2.6 ± 1.1	-2.9 ± 1.2	-3.1 ± 1.3
b_{HCD}	-0.037 ± 0.007	-0.049 ± 0.008	-0.053 ± 0.011	-0.067 ± 0.015
b_{q}	2.73 ± 0.29	2.88 ± 0.14	3.20 ± 0.23	4.1 ± 0.5
$\Delta r_{\parallel}$ (h^{-1}Mpc)	-1.07 ± 0.17	-1.99 ± 0.13	-3.5 ± 0.4	-3.4 ± 1.0
σ_{v} (h^{-1}Mpc)	5.4 ± 0.7	5.5 ± 0.6	6.3 ± 1.0	8.1 ± 1.8
ξ_0^{TP}	0.13 ± 0.04	0.18 ± 0.04	0.51 ± 0.13	0.8 ± 0.4
A_{inst}	2.29 ± 0.29	2.38 ± 0.27	2.42 ± 0.27	2.42 ± 0.27
χ^2_{JOINT}	1.033	1.030	1.030	1.053
z_{eff}	2.09	2.33	2.62	2.99

Table 4.3: Results of the fits for the four redshift evolution bins. The number of quasars in each bin is given, along with the redshift range of each bin. In all fits the BAO parameters are fixed at 1.0. The rest of the parameters are allowed to float in each fit and are described in table 4.5 in appendix 4.8. Each fit has 11,644 data bins, 13 free parameters and we also list the effective redshift, z_{eff}. Since each fit is a joint fit of the auto- and cross-correlations, we list the χ^2 value given for the joint fit.

maximum separation of $80\,h^{-1}$ Mpc. We use the same sample of Lyman-α forests as the baseline, but we create new quasar catalogs with approximately 41,000 objects in the first catalog, 28,000 objects in the second, 17,000 objects in the third, and 19,000 objects in the fourth. We then re-calculate the cross-correlation and fit for each redshift bin following the methods in section 4.3. Since the auto-correlation only depends on the Lyman-α forest sample, we do not need to re-compute it and can use the auto-correlation from [56] for each redshift bin when computing the joint fit.

The fit results for each redshift bin are given in table 4.3. Each fit has the same configuration as the baseline fit presented in the first column of table 4.2. We plot these results vs the average redshift in each bin in figure 4.6, highlighting the baseline value in the shaded region. We find a strong evolution with redshift for $\Delta r_{\parallel}$ with the value becoming more negative as the average redshift of the bin increases for the first three bins. However, the fourth redshift bin does not clearly follow this trend. Though this bin does not have the least amount of quasars, the quasars in this bin are at a higher redshift and are generally fainter and have lower signal to noise. The fit for this redshift bin is also the worst of the four with a $\chi^2 = 1.053$, which corresponds to near-zero probability given the 11,631 degrees of freedom in the fit. Despite this, the overall trend indicates that the quasar redshifts are being underestimated by a larger amount as the quasar redshift increases, which is consistent with the quasar templates not accounting for the Lyman-α forest optical depth. If the loss of the MgII emission line in the quasar spectra was the dominant contribution to the redshift errors, we would expect a sudden jump in $\Delta r_{\|}$ and $\sigma_{\rm v}$ as a function of z around $z = 2.5$. Such a feature is not observed, so the loss of MgII is unlikely to be the culprit.

The measured evolution of $\sigma_{\rm v}$ as a function of z is much less striking than that of $\Delta r_{\|}$. Still, there is an indication for a mild increase of $\sigma_{\rm v}$ for higher redshift quasars, consistent with less precision in the measured redshift.

4.5.3 Impact of BALs and Updating BAL Quasar Redshifts

BAL systems can impact the shape of quasar emission lines and introduce shifts in the estimated quasar redshift, up to several hundred km s^{-1} [49]. BAL quasars often have larger redshift errors compared to quasars with no BAL features because the BAL features impact the blue side of emission lines [54]. This is true in DESI, where Redrock tends to overestimate redshifts for BAL quasars [54]. The current pipeline used for most Lyman-α studies, picca, has the option to mask out BAL regions during the continuum fitting process, but does not update the quasar redshift when these masks are applied so any systematic errors on the quasar redshift will still be present. [49] shows that when BAL regions of a quasar spectrum are masked and new redshifts are obtained, those new redshifts shift by 240

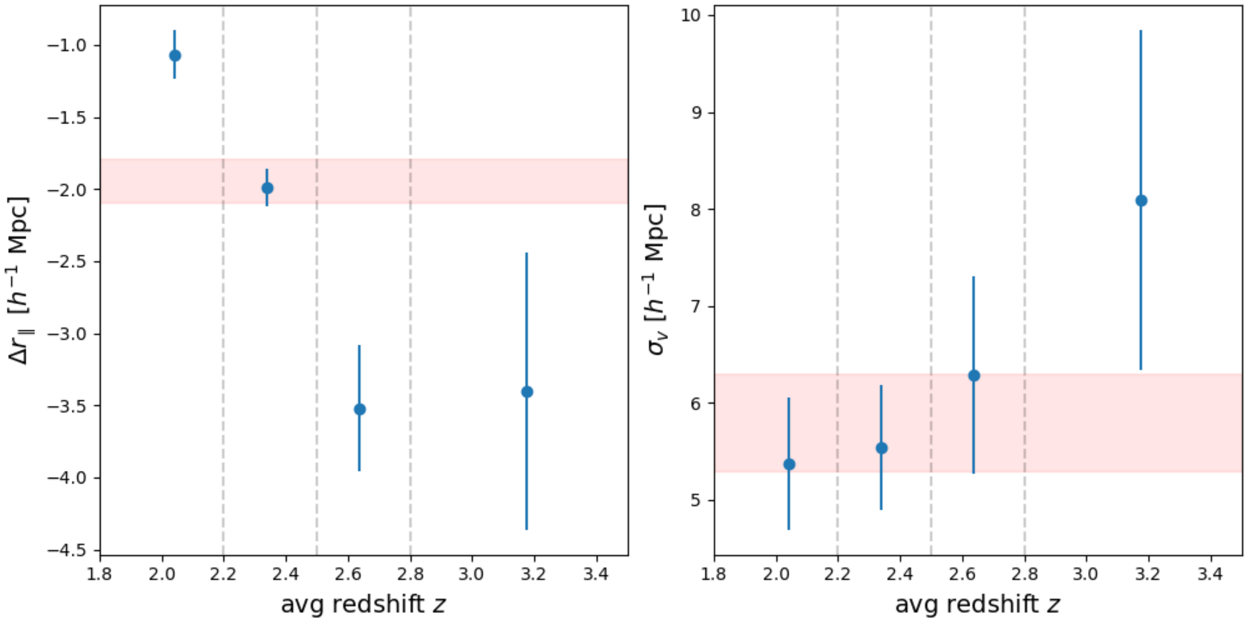

Figure 4.6: Evolution of $\Delta r_{\parallel}$ and σ_{v} with redshift for four different redshift bins (blue points). The bin edges at z = 2.2, 2.5, and 2.8 are marked by the dashed grey lines. The red shaded region denotes the baseline value for each parameter: $\Delta r_{\parallel} = -1.94 \pm 0.15\ h^{-1}$ Mpc and $\sigma_{\mathrm{v}} = 5.8 \pm 0.5\ h^{-1}$ Mpc.

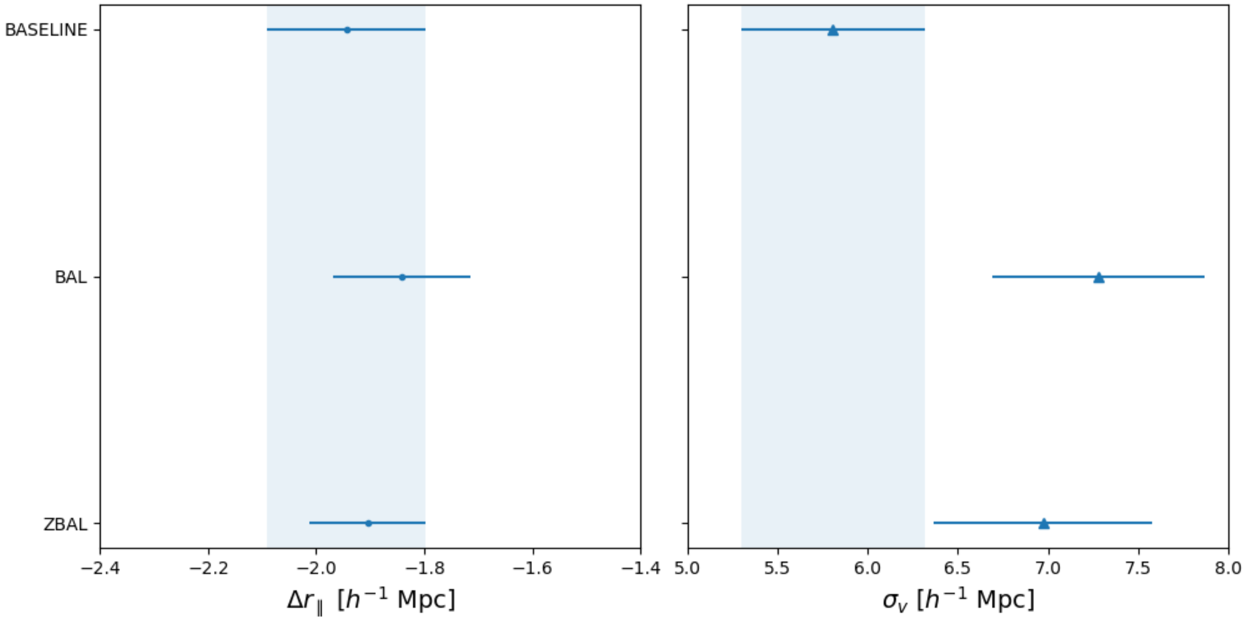

Figure 4.7: Results on $\Delta r_{\parallel}$ (left, blue points) and σ_{v} (right, blue triangles) for the four different configurations presented in this work: baseline, BAL, and ZBAL. The shaded area represents the value of the parameters from the baseline fit.

km s^{-1} on average. We explore in this section the effect of including the BAL quasars in the tracer catalog as well as using the updated BAL redshifts from [49] once the BAL regions of the quasar spectra are masked.

We first test if including BAL quasars in the tracer quasar catalog will have an effect on $\Delta r_{\parallel}$ or σ_{v}. For this test we use the same Lyman-α forest sample as [86] which is the same as our baseline. The tracer quasar catalog is the same as described in section 4.2.1 except the BALs are not removed. It consists of 128,026 quasars with redshift $z > 1.88$. We use the auto-correlation from [56] and follow the same method described in section 4.3 to measure and fit the cross-correlation. We find $\Delta r_{\parallel} = -1.84 \pm 0.13$ h^{-1} Mpc and $\sigma_{\mathrm{v}} = 7.3 \pm 0.6$ h^{-1} Mpc. These results, along with those from the baseline configuration, are shown in figure 4.7 and presented in table 4.2 in the BAL column. The shift of $\Delta r_{\parallel}$ in the positive direction would seem to indicate that including BAL quasars in the tracer catalog reduces the quasar redshift errors. However, this is actually due to BAL quasars typically having overestimated redshifts, as the BAL features tend to impact the blue side of the emission lines [54]. Any overestimation of quasar redshifts would shift $\Delta r_{\parallel}$ in the positive direction. This is the opposite of what we observe when the BAL quasars are excluded, where the shift in $\Delta r_{\parallel}$ is negative due to the underestimation of redshifts. It is likely that the inclusion of the BAL quasars partially compensates for the negative shift.

To test if updating the BAL quasar redshifts after the BAL regions are masked improves the $\Delta r_{\parallel}$ parameter, we use the quasar catalog from [49]. This is the same catalog as described above, but with updated redshifts for the BAL quasars, of which 28,185 BAL quasars have an updated redshift. Because the redshifts are updated, we can no longer use the Lyman-α forest sample described in [86]. We follow the method in [86] and in section 4.3 for the continuum fitting process and our final Lyman-α sample consists of 88,432 forests. We use the tracer catalog with updated redshifts and follow the method described in section 4.3 to measure and fit the correlations. We can no longer use the auto-correlation from [56], so we measure those following the method in [56]. The results are shown in figure 4.7 and in table 4.2 in the ZBAL column. We find $\Delta r_{\parallel} = -1.90 \pm 0.11 \ \ h^{-1}$ Mpc and $\sigma_{\rm v} = 7.0 \pm 0.6 \ \ h^{-1}$ Mpc. The value of $\Delta r_{\parallel}$ has shifted in the negative direction and is now equal (0.35σ) to the baseline value. This negative shift is consistent with what is found in [49], which found that the redshifts of BAL quasars after masking were shifted to the blue.

This shows that BAL quasars can affect the correlations when they are included in the tracer catalog and their redshifts are not updated after the BAL regions are masked. When the redshifts are updated the inclusion of BAL quasars in the tracer catalog has no effect.

4.6 Addressing the Redshift Dependency

The redshift dependency in $\Delta r_{\parallel}$ is also reported in the year one quasar sample by [18], who suggest the bias could be mitigated through proper modeling of the mean transmission of Lyman-α in the spectral templates used for redshift estimation. We define the mean transmitted flux fraction, $\overline{F}$, as

$$\overline{F}(z) = e^{-\tau_{\rm eff,\alpha}(z)}, \tag{4.24}$$

where

$$\tau_{\rm eff,\alpha} = \tau_0 (1+z)^{\gamma} \tag{4.25}$$

is the effective optical depth of the Lyman-α transition, $\tau_0 = (5.54 \pm 0.64) \times 10^{-3}$ and $\gamma = 3.182 \pm 0.074$ [69]. $\overline{F}$ depends on $\tau_{\rm eff,\alpha}$ at $z = \frac{\lambda_{\rm obs} - \lambda_{\rm Ly\alpha}}{\lambda_{\rm Ly\alpha}}$ according to eq. 4.24. $\tau_{\rm eff,\alpha}$ evolves with redshift, as parameterized by eq. 4.25 [e.g., 21, 69, 72], implying greater overall flux suppression in the Lyman-α forest region of quasar spectra at higher redshifts. The BOSS quasar templates used for EDR and the DESI year 1 quasar templates were derived from samples of quasar spectra that were not corrected for the optical depth of Lyman-α photons. On the other hand, a real-time correction for this flux suppression was being applied in Redrock during redshift fitting, leading to an over-suppression of template flux relative to what was expected at $\lambda_{\mathrm{RF}} < 1215.67$Å. This resulted in a bias that increases with the amount of suppression (i.e. redshift) at $z > 2$.

We update the DESI year one quasar templates with the Lyman-α effective optical depth model from [69] and test whether the observed redshift bias is mitigated. The year one quasar templates consist of two eigenspectra sets which are trained to classify separate, yet overlapping redshift ranges: $0.05 < z < 1.6$ and $1.4 < z < 7.0$, dubbed LOZ and HIZ, respectively. As the Lyman-α forest is only observed in DESI quasar spectra with $z > 1.95$, only the HIZ templates require modification. A new version of the HIZ templates are derived from the same sample as in [18], but the individual spectra are corrected for suppression from Lyman-α effective optical depth at $\lambda_{RF} < 1215.67$Å. The Lyman-α optical depth model in Redrock was then updated accordingly.[4] Our updated HIZ templates can be found on Github.[5]

We use the updated HIZ templates with modified Redrock to refine the redshifts of the DESI year 1 quasar sample at $z > 1.6$. This redshift is defined by the upper limit of the redshift coverage for the LOZ templates, though we note substantial impact is only expected at $z > 1.95$. We impose a prior of $\Delta v = \pm 3000$ km s^{-1} from the original redshift estimate, as the HIZ redshifts have been shown to be approximately correct within a few tens to hundreds of km s^{-1}, on average. Approximately 850,000 objects had a change in redshift when using the updated HIZ templates, and we show the distribution of those changes in figure 4.8.

To test that the redshift bias shown in $\Delta r_{\parallel}$ is mitigated we perform our analysis again using the updated quasar templates. We use the year 1 Lyman-α forest sample and tracer

---

[4] `https://github.com/desihub/redrock/releases/tag/0.17.9`

[5] `https://github.com/desihub/redrock-templates/releases/tag/0.8.1`

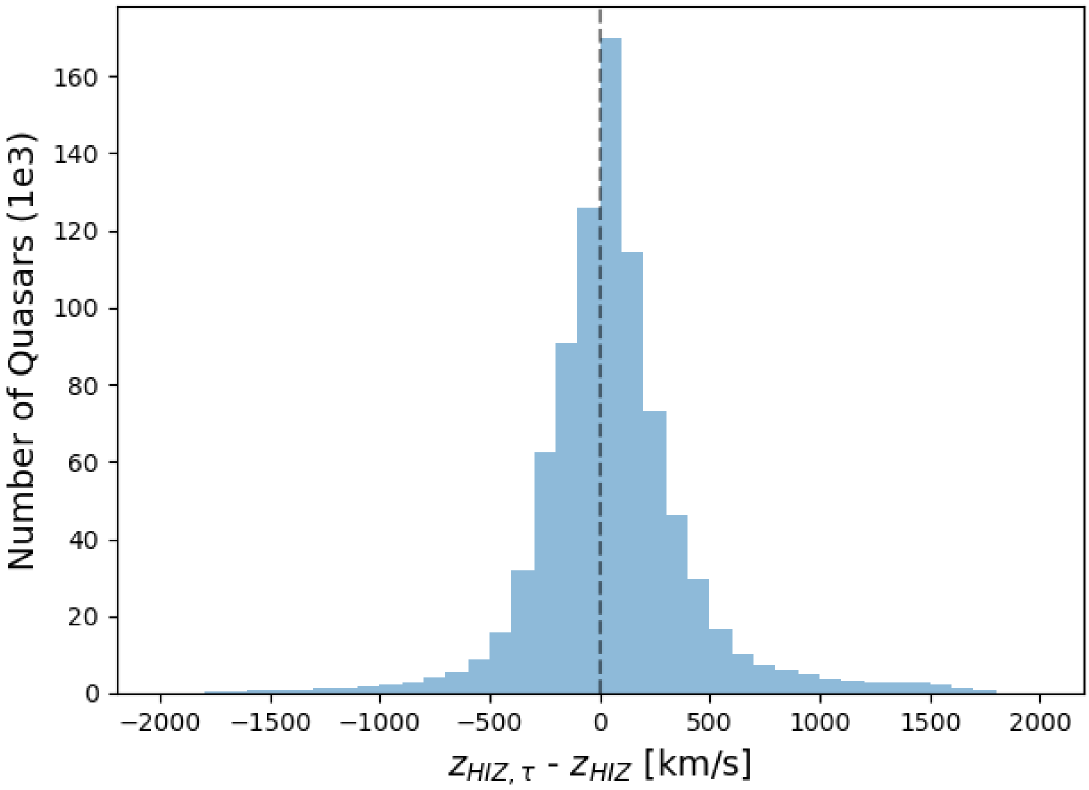

Figure 4.8: Distribution of the difference in redshift (in km s^{-1}) for the quasars in the year 1 catalog between the redshifts measured with the updated HIZ templates ($z_{\mathrm{HIZ},\tau}$) versus the redshifts measured from the templates without the Lyman-α optical depth correction (z_{HIZ}).

Parameter	baseline	z1	z2	z3	z4
No. quasars	510,501	201,290	138,364	82,710	88,137
Redshift range	-	$z \leq 2.2$	$2.2 < z \leq 2.5$	$2.5 < z \leq 2.8$	$z > 2.8$
$b_{\mathrm{Ly}\alpha}$	-0.0543 ± 0.0035	-0.049 ± 0.005	-0.055 ± 0.005	-0.060 ± 0.006	-0.162 ± 0.020
$\beta_{\mathrm{Ly}\alpha}$	3.78 ± 0.26	3.3 ± 0.4	3.8 ± 0.4	4.5 ± 0.5	2.01 ± 0.28
$10^3 b_{\eta,\mathrm{SiII(1190)}}$	-2.5 ± 0.4	-2.6 ± 0.4	-2.8 ± 0.4	-3.9 ± 0.5	-3.4 ± 0.5
$10^3 b_{\eta,\mathrm{SiII(1193)}}$	-1.34 ± 0.35	-1.3 ± 0.4	-2.2 ± 0.4	-2.0 ± 0.5	-2.2 ± 0.5
$10^3 b_{\eta,\mathrm{SiIII(1207)}}$	-4.50 ± 0.31	-5.0 ± 0.4	-5.0 ± 0.4	-6.0 ± 0.5	-5.4 ± 0.5
$10^3 b_{\eta,\mathrm{SiII(1260)}}$	-3.1 ± 0.6	-2.9 ± 0.5	-3.2 ± 0.6	-3.8 ± 0.7	-3.2 ± 0.6
b_{HCD}	-0.0574 ± 0.0034	-0.0491 ± 0.0029	-0.061 ± 0.004	-0.082 ± 0.005	-0.089 ± 0.006
b_{q}	3.97 ± 0.10	3.35 ± 0.13	3.99 ± 0.13	4.73 ± 0.17	4.35 ± 0.23
$\Delta r_{\parallel}$ (h^{-1}Mpc)	-0.08 ± 0.04	-0.01 ± 0.06	-0.16 ± 0.07	-0.09 ± 0.08	-0.11 ± 0.13
σ_{v} (h^{-1}Mpc)	5.21 ± 0.17	4.79 ± 0.25	5.35 ± 0.25	5.45 ± 0.35	3.46 ± 0.35
ξ_0^{TP}	0.074 ± 0.008	0.066 ± 0.013	0.061 ± 0.014	0.114 ± 0.023	0.52 ± 0.09
$10^4 A_{\mathrm{inst}}$	1.33 ± 0.09	1.4 ± 0.1	1.36 ± 0.10	1.35 ± 0.10	1.51 ± 0.10
χ^2_{JOINT}	1.027	1.025	1.022	0.999	0.995
z_{eff}	2.32	2.09	2.33	2.61	2.98

Table 4.4: Results of the fits using the updated quasar templates for the new baseline and four redshift bins. The number of quasars in each bin is given, along with the redshift range of each bin where applicable. The free parameters are the same as described in section 4.5. In all fits the BAO parameters are fixed at 1.0. Each fit has 11,644 data bins, 13 free parameters and we also list the effective redshift, z_{eff}. Since each fit is a joint fit of the auto- and cross-correlations, we list the χ^2 value given for the joint fit.

quasar catalog from [34]. To be consistent with our baseline analysis we remove any BAL quasars from the tracer catalog. There are 510,000 quasars in the tracer catalog with redshift $z > 1.88$. We also split the tracer quasar sample to test for any evolution with redshift with the same cuts as in section 4.5.2: $z = 2.2$, 2.5, and 2.8. We measure and fit the correlations using the same method described in section 4.3, and we show the results in table 4.4 and figure 4.9.

We find $\Delta r_{\parallel} = -0.08 \pm 0.04$ h^{-1} Mpc and $\sigma_{\mathrm{v}} = 5.21 \pm 0.17$ h^{-1} Mpc, which are shown as the red shaded region in figure 4.9. When testing for any evolution on $\Delta r_{\parallel}$ with redshift we find that the bias on $\Delta r_{\parallel}$ has been resolved. For the four redshift bins we find $\Delta r_{\parallel}$ [h^{-1}Mpc] $= -0.01 \pm 0.06$, -0.16 ± 0.07, -0.09 ± 0.08, and -0.11 ± 0.13, respectively. The results for σ_{v} also suggest a better precision on the measured redshifts. We find σ_{v} [h^{-1}Mpc] $= 4.79 \pm 0.25$, 5.35 ± 0.25, 5.45 ± 0.35, and 3.46 ± 0.35 for the four redshift bins, respectively.

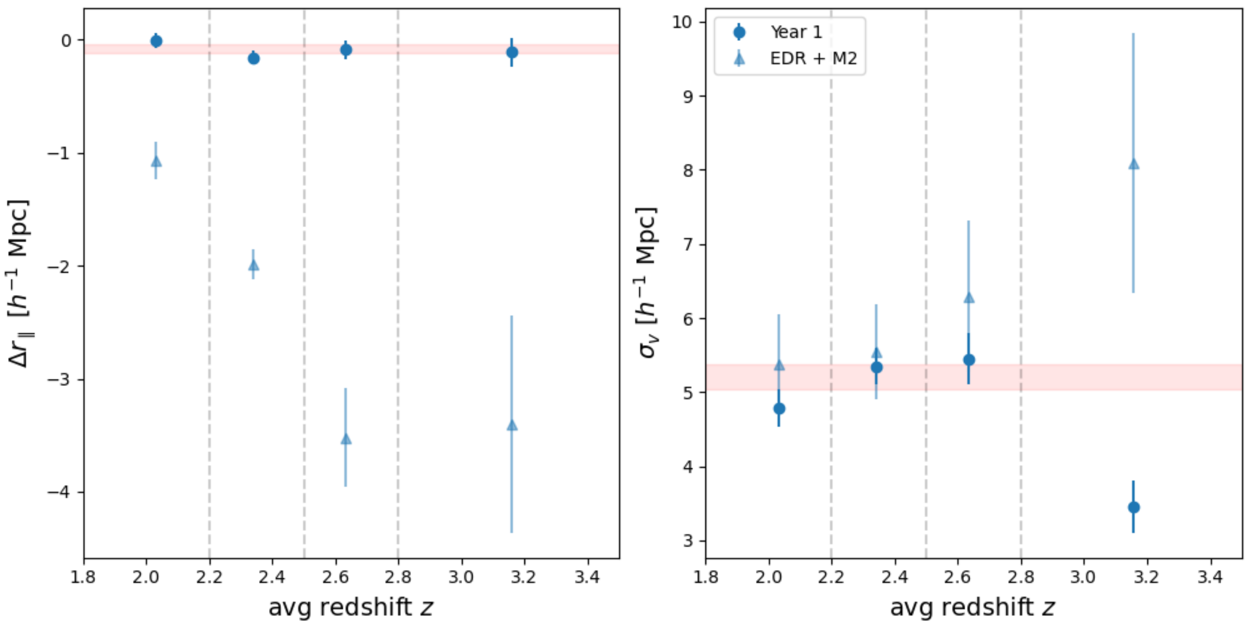

Figure 4.9: Evolution of $\Delta r_\parallel$ and σ_v with redshift using the updated quasar templates for the four different redshift bins (blue points). The results with the old templates are shown in light blue triangles for comparison. The bin edges at z = 2.2, 2.5, and 2.8 are marked by the dashed grey lines. The red shaded region denotes the baseline value for each parameter: $\Delta r_\parallel = -0.08 \pm 0.04\ h^{-1}$ Mpc and $\sigma_\mathrm{v} = 5.21 \pm 0.17\ h^{-1}$ Mpc.

Our updated HIZ templates and Redrock code have corrected the bias that was found using previous versions of the quasar templates and Redrock. The updated templates and Redrock will provide the redshifts for the DESI year one Lyman-α cosmology studies [34]. The redshifts will be publicly released with the year one quasar sample.

4.7 Summary

We present here the study of the impact of quasar redshift errors on the 3D Lyman-α forest-quasar cross-correlation. Using EDR+M2 data, the Lyman-α forest sample from [86], and the auto-correlation from [56], we compute the cross-correlation using a 1 h^{-1} Mpc bin width up to 80 h^{-1} Mpc in the $r_\parallel$ and $r_\perp$ directions. We validate our choice to use a 1 h^{-1} Mpc bin width with mock data. Our model has 13 free parameters, of which $\Delta r_\parallel$ and σ_v are used to quantify any systematic quasar redshift errors.

In our baseline fit we find $\Delta r_{\parallel} = -1.94 \pm 0.15$ h^{-1} Mpc (-205 ± 15 km s^{-1}) and $\sigma_{\mathrm{v}} = 5.8 \pm 0.5$ h^{-1} Mpc (610 ± 50 km s^{-1}), which indicates that the EDR+M2 quasar redshifts are underestimated. It was reported in [18] that there is a redshift-dependent bias in the eBOSS quasar templates that likely stems from the improper correction of the Lyman-α forest optical depth. This introduces suppression in the Lyman-α forest that increases with redshift. We confirm that this bias is present in the EDR+M2 sample by measuring and fitting the cross-correlation when the tracer quasar catalog is cut into four redshift bins with boundaries at $z = 2.2$, 2.5, and 2.8. We find $\Delta r_{\parallel}$ [h^{-1} Mpc] $= -1.07 \pm 0.17$, -1.99 ± 0.13, -3.5 ± 0.4, and -3.4 ± 1.0 for the four bins, respectively. This shows a redshift-dependent bias that increases with redshift.

New HIZ quasar templates were derived that corrected for the suppression from the Lyman-α effective optical depth. A modified version of Redrock was run with these new templates to update the DESI Year 1 quasar sample at $z > 1.6$. We then repeat our analysis with the new Year 1 quasar redshifts to confirm that the bias in $\Delta r_{\parallel}$ is resolved. We find $\Delta r_{\parallel} = -0.08 \pm 0.04$ h^{-1} Mpc (-9.0 ± 4.0 km s^{-1}) and $\sigma_{\mathrm{v}} = 5.21 \pm 0.17$ h^{-1} Mpc (-548 ± 17 km s^{-1}) when repeating the analysis on the entire year 1 quasar sample. We again split the catalog into four redshift bins with boundaries at $z = 2.2$, 2.5, and 2.8 and we find $\Delta r_{\parallel}$ [h^{-1} Mpc] $= -0.01 \pm 0.06$, -0.16 ± 0.07, -0.09 ± 0.08, and -0.11 ± 0.13 for the four redshift bins, respectively.

We have shown that our updated HIZ quasar templates have mitigated the redshift bias on $\Delta r_{\parallel}$. These templates will be used to provide redshifts for the DESI year 1 quasar sample and those redshifts will be used for the Year 1 analyses.

4.8 Appendix A: Fit Parameters

Parameter	Value	Description
$\alpha_\parallel, \alpha_\perp$	1.0	BAO peak position parameters
A_{peak}	1.0	BAO amplitude (eq. 4.16)
b_{q}	floating	Quasar bias parameter (eq. 4.12)
β_{q}	0.323	Quasar RSD parameter (derived) (eq. 4.13)
α_{q}	1.44	Redshift evolution parameter for b_{q} (eq. 4.12)
$b_{\text{Ly}\alpha}$	floating	Lyman-α absorber bias parameter (eq. 4.14)
$\beta_{\text{Ly}\alpha}$	floating	Lyman-α absorber RSD parameter (eq. 4.15)
α_{Lya}	2.9	Redshift evolution parameter for b_{Lya} (eq. 4.12)
b_{HCD}	floating	Bias parameter from unidentified HCD systems (eq. 4.15)
β_{HCD}	floating	RSD parameter from unidentified HCD systems (eq. 4.15)
L_{HCD}	$10\,h^{-1}\,\text{Mpc}$	Length scale from unidentified HCD systems (eq. 4.15)
b_{m}	floating	Bias parameters for the metal species listed in table 4.1
β_{m}	0.5	RSD parameters for the metal species listed in table 4.1
α_{m}	1.0	Redshift evolution parameter for metal biases b_{m}
σ_{v}	floating	Quasar non-linear velocity and precision (eq. 4.18)
$\Delta r_\parallel$	floating	The systematic offset in quasar redshift (eq. 4.23)
f	0.9703	Linear growth rate of structure (eq. 4.17)
$\Sigma = (\Sigma_\parallel, \Sigma_\perp)$	$(6.37, 3.26)\ h^{-1}$ Mpc	Non-linear broadening of the BAO peak (eq. 4.16)
$\mathbf{R} = (R_\parallel, R_\perp)$	$(1, 1)\ h^{-1}$ Mpc	Smoothing parameters for the binning of the correlation (eq. 4.19)
ξ_0^{TP}	floating	Transverse proximity effect (eq. 4.22)
$a_{\text{UV}}, t_{\text{UV}}$	0	Quasar radiation and anisotropy lifetime (eq. 4.22)
λ_{UV}	$300\,h^{-1}\,\text{Mpc}$	Mean free path of UV photons (eq. 4.22)
A_{inst}	floating	Instrumental systematics parameter (equation 4.11 in [56])

Table 4.5: Parameters of the joint fit of the Lyman-α forest auto- and cross-correlations. The second column gives the value for each fixed parameter or if it is floating in the fit. The third column provides a brief description of each parameter and also a reference to the relevant equation. All biases b refer to the bias calculated at the effective redshift ($z_{\text{eff}} = 2.34$ for the baseline fit).

Chapter 5

Conclusions

The upcoming decade will bring exciting results to the field of cosmology. With only a year's worth of data, DESI has already made measurements that suggest dark energy might not be constant in our cosmological model. The inclusion of future DESI datasets, as well as data from Rubin Observatory's LSST will confirm this measurement. The extension to the DESI survey, DESI-ext, looks to increase the precision on this measurement. Future proposed surveys, like DESI-2 and the Stage-V experiment Spec-S5, both look to further our understanding of the nature of dark energy.

While the future is certainly exciting, this thesis focuses on improvements to the current DESI survey. Approximately 12% of the robotic fiber positioners on the DESI focal plane are unusable due to their behavior. This number is increasing at a rate of roughly 1 positioner per week. Chapter 3 focused on mitigation strategies for the positioners displaying linear phi behavior. I found that by increasing the speed of the phi motors, applying a scale factor correction to each move request, and enforcing all moves to follow the back and forth move algorithm discussed in section 3.5, the linear phi positioners could position with an accuracy approximately 1.5 times larger than the good phi positioners.

This was first tested on two DESI petals (94 positioners) in March of 2024. At this time, 41 positioners were selected to be returned to service and were first operated for science exposures in June of 2024. While their performance improved each night, it did not reach the same level that was achieved during the testing in March. It is now believed that the linear phi positioners need a warm up before being positioned for science exposures. There was also an issue with the anti-collision software not being able to resolve moves due to the back and forth move algorithm. This will be fixed before these positioners are returned to nightly operations.

In July of 2024, tests on 314 linear phi positioners on the entire DESI focal plane were performed, including the same positioners tested in March. These tests showed that 228 positioners, or roughly 72% of the linear phi positioners, are eligible to be returned to service. This is scheduled to happen by the end of the 2024 calendar year.

If all 228 positioners remain in operation until the end of the main survey (assuming the 1 per week rate holds), the DESI main survey will finish with 491 disabled positioners.

Chapter 4 of this thesis focuses on improvements to quasar redshifts and the impact that errors have on the Lyman-α forest analysis. The Lyman-α forest-quasar cross-correlation is a powerful tool for measuring quasar redshift errors. The model used has 13 free parameters, of which $\Delta r_{\parallel}$ and $\sigma_{\rm v}$ are used to quantify any quasar redshift errors. For the DESI EDR dataset, I found from the cross-correlation that $\Delta r_{\parallel} = -1.94 \pm 0.15\ h^{-1}$ Mpc (205 km s^{-1}), which suggests that the quasar redshifts are being underestimated. I explored this further, by cutting the quasar catalog into four redshift bins and found a redshift-dependent bias that increases with redshift.

The root cause of this bias came from the high redshift quasar templates that did not properly account for the suppression from the Lyman-α effective optical depth. New templates were derived and new redshifts were estimated for the DESI Year 1 quasar sample at $z > 1.6$. I then repeated the analysis and found that the bias in $\Delta r_{\parallel}$ is resolved. I found $\Delta r_{\parallel} = -0.08 \pm 0.04$ h^{-1} Mpc (-9.0 ± 4.0 km s^{-1}), which is consistent with zero.

These new templates were used to provide redshifts for the DESI year 1 quasar sample and those redshifts were used for the year 1 analyses. The templates will be used for future DESI datasets as well.

Bibliography

[1] "e2v Model CCD 230-42 Datasheet." `http://www.e2v.com/resources/account/download-datasheet/3828`.

[2] "Preliminary Project Execution Plan." `https://science.osti.gov/-/media/hep/pdf/files/Project-Status/LSST-CD-0-MNS-Extract--20121107.pdf`, 2012.

[3] "Pathways to Innovation and Discovery in Particle Physics: Report of the 2023 Particle Physics Project Prioritization Panel." `https://www.usparticlephysics.org/2023-p5-report/`, 2024.

[4] S. Alam, M. Ata, S. Bailey, F. Beutler, D. Bizyaev, J. A. Blazek et al., *The clustering of galaxies in the completed SDSS-III Baryon Oscillation Spectroscopic Survey: cosmological analysis of the DR12 galaxy sample*, Mon. Not. Roy. Astron. Soc. **470** (2017) 2617 [`1607.03155`].

[5] S. Alam, M. Aubert, S. Avila, C. Balland, J. E. Bautista, M. A. Bershady et al., *Completed SDSS-IV extended Baryon Oscillation Spectroscopic Survey: Cosmological implications from two decades of spectroscopic surveys at the Apache Point Observatory*, Phys. Rev. **D 103** (2021) 083533 [`2007.08991`].

[6] D. M. Alexander, T. M. Davis, E. Chaussidon, V. A. Fawcett, A. X. Gonzalez-Morales, T.-W. Lan et al., *The DESI Survey Validation: Results from Visual Inspection of the Quasar Survey Spectra*, *AJ* **165** (2023) 124 [`2208.08517`].

[7] Apache Point Observatory, "Sloan Digital Sky Survey Plate Plugging Time Lapse." `https://www.youtube.com/watch?v=i6ZOUDWRwtg`.

[8] A. Arinyo-i-Prats, J. Miralda-Escudé, M. Viel and R. Cen, *The non-linear power spectrum of the Lyman alpha forest*, *JCAP* **2015** (2015) 017 [`1506.04519`].

[9] S. Bailey et al., *Redrock: Spectroscopic Classification and Redshift Fitting for the Dark Energy Spectroscopic Instrument*, *in preparation* (2024) .

[10] A. Bault and DESI Collaboration, *Mitigation and Recovery of the Linear Phi Positioners in the Dark Energy Spectroscopic Instrument*, *in preparation* (2025) .

[11] A. Bault, D. Kirkby, J. Guy, A. Brodzeller, J. Aguilar, S. Ahlen et al., *Impact of Systematic Redshift Errors on the Cross-correlation of the Lyman-α Forest with*

Quasars at Small Scales Using DESI Early Data, *arXiv e-prints* (2024) arXiv:2402.18009 [`2402.18009`].

[12] J. E. Bautista, N. G. Busca, J. Guy, J. Rich, M. Blomqvist, H. du Mas des Bourboux et al., *Measurement of baryon acoustic oscillation correlations at* $z = 2.3$ *with SDSS DR12 Ly*α*-Forests*, Astron. Astrophys. **603** (2017) A12 [`1702.00176`].

[13] F. Beutler, C. Blake, M. Colless, D. H. Jones, L. Staveley-Smith, L. Campbell et al., *The 6dF Galaxy Survey: baryon acoustic oscillations and the local Hubble constant*, Mon. Not. Roy. Astron. Soc. **416** (2011) 3017 [`1106.3366`].

[14] C. Blake, S. Brough, M. Colless, C. Contreras, W. Couch, S. Croom et al., *The WiggleZ Dark Energy Survey: joint measurements of the expansion and growth history at z ¡ 1*, Mon. Not. Roy. Astron. Soc. **425** (2012) 405 [`1204.3674`].

[15] M. Blomqvist, H. du Mas des Bourboux, N. G. Busca, V. de Sainte Agathe, J. Rich, C. Balland et al., *Baryon acoustic oscillations from the cross-correlation of Ly*α *absorption and quasars in eBOSS DR14*, Astron. Astrophys. **629** (2019) A86 [`1904.03430`].

[16] M. Blomqvist, M. M. Pieri, H. du Mas des Bourboux, N. G. Busca, A. Slosar, J. E. Bautista et al., *The triply-ionized carbon forest from eBOSS: cosmological correlations with quasars in SDSS-IV DR14*, *JCAP* **2018** (2018) 029 [`1801.01852`].

[17] A. S. Bolton, D. J. Schlegel, É. Aubourg, S. Bailey, V. Bhardwaj, J. R. Brownstein et al., *Spectral Classification and Redshift Measurement for the SDSS-III Baryon Oscillation Spectroscopic Survey*, *AJ* **144** (2012) 144 [`1207.7326`].

[18] A. Brodzeller, K. Dawson, S. Bailey, J. Yu, A. J. Ross, A. Bault et al., *Performance of the Quasar Spectral Templates for the Dark Energy Spectroscopic Instrument*, *AJ* **166** (2023) 66 [`2305.10426`].

[19] N. G. Busca, T. Delubac, J. Rich, S. Bailey, A. Font-Ribera, D. Kirkby et al., *Baryon acoustic oscillations in the Ly*α *forest of BOSS quasars*, Astron. Astrophys. **552** (2013) A96 [`1211.2616`].

[20] N. Busca and C. Balland, *QuasarNET: Human-level spectral classification and redshifting with Deep Neural Networks*, *arXiv e-prints* (2018) arXiv:1808.09955 [`1808.09955`].

[21] F. Calura, E. Tescari, V. D'Odorico, M. Viel, S. Cristiani, T. S. Kim et al., *The Lyman* α *forest flux probability distribution at z¿3*, Mon. Not. Roy. Astron. Soc. **422** (2012) 3019 [`1201.5121`].

[22] S. Chabanier, M. Millea and N. Palanque-Delabrouille, *Matter power spectrum: from Ly* α *forest to CMB scales*, Mon. Not. Roy. Astron. Soc. **489** (2019) 2247 [`1905.08103`].

[23] E. Chaussidon, C. Yèche, N. Palanque-Delabrouille, D. M. Alexander, J. Yang, S. Ahlen et al., *Target Selection and Validation of DESI Quasars*, *ApJ* **944** (2023) 107 [`2208.08511`].

[24] S. Cole, W. J. Percival, J. A. Peacock, P. Norberg, C. M. Baugh, C. S. Frenk et al., *The 2dF Galaxy Redshift Survey: power-spectrum analysis of the final data set and cosmological implications*, Mon. Not. Roy. Astron. Soc. **362** (2005) 505 [`astro-ph/0501174`].

[25] A. Cuceu, A. Font-Ribera, S. Nadathur, B. Joachimi and P. Martini, *Constraints on the Cosmic Expansion Rate at Redshift 2.3 from the Lyman-α Forest*, Phys. Rev. Lett. **130** (2023) 191003 [`2209.13942`].

[26] G. de Vaucouleurs and G. Bollinger, *The extragalactic distance scale. VII. The velocity-distance relations in different directions and the Hubble ratio within and without the local supercluster.*, *ApJ* **233** (1979) 433.

[27] T. Delubac, J. E. Bautista, N. G. Busca, J. Rich, D. Kirkby, S. Bailey et al., *Baryon acoustic oscillations in the Lyα forest of BOSS DR11 quasars*, Astron. Astrophys. **574** (2015) A59 [`1404.1801`].

[28] DESI Collaboration, "DESI Collaboration, private communication, 2024."

[29] DESI Collaboration, *DESI 2024 I: Data Release 1 of the Dark Energy Spectroscopic Instrument*, *in preparation* (2025) .

[30] DESI Collaboration, B. Abareshi, J. Aguilar, S. Ahlen, S. Alam, D. M. Alexander et al., *Overview of the Instrumentation for the Dark Energy Spectroscopic Instrument*, *AJ* **164** (2022) 207 [`2205.10939`].

[31] DESI Collaboration, A. G. Adame, J. Aguilar, S. Ahlen, S. Alam, G. Aldering et al., *Validation of the Scientific Program for the Dark Energy Spectroscopic Instrument*, *AJ* **167** (2024) 62 [`2306.06307`].

[32] DESI Collaboration, A. G. Adame, J. Aguilar, S. Ahlen, S. Alam, G. Aldering et al., *The Early Data Release of the Dark Energy Spectroscopic Instrument*, *arXiv e-prints* (2023) arXiv:2306.06308 [`2306.06308`].

[33] DESI Collaboration, A. G. Adame, J. Aguilar, S. Ahlen, S. Alam, D. M. Alexander et al., *DESI 2024 VI: Cosmological Constraints from the Measurements of Baryon Acoustic Oscillations*, *arXiv e-prints* (2024) arXiv:2404.03002 [`2404.03002`].

[34] DESI Collaboration, A. G. Adame, J. Aguilar, S. Ahlen, S. Alam, D. M. Alexander et al., *DESI 2024 IV: Baryon Acoustic Oscillations from the Lyman Alpha Forest*, *arXiv e-prints* (2024) arXiv:2404.03001 [`2404.03001`].

[35] DESI Collaboration, A. G. Adame, J. Aguilar, S. Ahlen, S. Alam, D. M. Alexander et al., *DESI 2024 III: Baryon Acoustic Oscillations from Galaxies and Quasars*, *arXiv e-prints* (2024) arXiv:2404.03000 [`2404.03000`].

[36] DESI Collaboration, A. Aghamousa, J. Aguilar, S. Ahlen, S. Alam, L. E. Allen et al., *The DESI Experiment Part I: Science,Targeting, and Survey Design*, *arXiv e-prints* (2016) arXiv:1611.00036 [`1611.00036`].

[37] DESI Collaboration, A. Aghamousa, J. Aguilar, S. Ahlen, S. Alam, L. E. Allen et al., *The DESI Experiment Part II: Instrument Design*, *arXiv e-prints* (2016) arXiv:1611.00037 [`1611.00037`].

[38] A. Dey and F. Valdes, *The Delivered Image Quality with the MOSAIC Cameras at the Kitt Peak 4 m Mayall and Cerro Tololo 4 m Blanco Telescopes*, *PASP* **126** (2014) 296.

[39] S. Dodelson and F. Schmidt, *1 - the concordance model of cosmology*, in *Modern Cosmology (Second Edition)* (S. Dodelson and F. Schmidt, eds.), pp. 1–19. Academic Press, second edition ed., 2021. DOI.

[40] S. Dodelson and F. Schmidt, *2 - the expanding universe*, in *Modern Cosmology (Second Edition)* (S. Dodelson and F. Schmidt, eds.), pp. 21–55. Academic Press, second edition ed., 2021. DOI.

[41] H. du Mas des Bourboux, K. S. Dawson, N. G. Busca, M. Blomqvist, V. de Sainte Agathe, C. Balland et al., *The Extended Baryon Oscillation Spectroscopic Survey: Measuring the Cross-correlation between the Mg II Flux Transmission Field and Quasars and Galaxies at z = 0.59*, *ApJ* **878** (2019) 47 [`1901.01950`].

[42] H. du Mas des Bourboux, J.-M. Le Goff, M. Blomqvist, N. G. Busca, J. Guy, J. Rich et al., *Baryon acoustic oscillations from the complete SDSS-III Lyα-quasar cross-correlation function at z = 2.4*, Astron. Astrophys. **608** (2017) A130 [`1708.02225`].

[43] H. du Mas des Bourboux, J. Rich, A. Font-Ribera, V. de Sainte Agathe, J. Farr, T. Etourneau et al., *The Completed SDSS-IV Extended Baryon Oscillation Spectroscopic Survey: Baryon Acoustic Oscillations with Lyα Forests*, *ApJ* **901** (2020) 153 [`2007.08995`].

[44] D. J. Eisenstein, H.-J. Seo and M. White, *On the Robustness of the Acoustic Scale in the Low-Redshift Clustering of Matter*, *ApJ* **664** (2007) 660 [`astro-ph/0604361`].

[45] D. J. Eisenstein, I. Zehavi, D. W. Hogg, R. Scoccimarro, M. R. Blanton, R. C. Nichol et al., *Detection of the Baryon Acoustic Peak in the Large-Scale Correlation Function of SDSS Luminous Red Galaxies*, *ApJ* **633** (2005) 560 [`astro-ph/0501171`].

[46] D. Eisenstein, *Dark energy and cosmic sound*, *New Astronomy Reviews* **49** (2005) 360.

[47] T. Etourneau, J.-M. Le Goff, J. Rich, T. Tan, A. Cuceu, S. Ahlen et al., *Mock data sets for the Eboss and DESI Lyman-α forest surveys*, *arXiv e-prints* (2023) arXiv:2310.18996 [`2310.18996`].

[48] J. Farr, A. Font-Ribera and A. Pontzen, *Optimal strategies for identifying quasars in DESI*, *JCAP* **2020** (2020) 015 [`2007.10348`].

[49] S. Filbert, P. Martini, K. Seebaluck, L. Ennesser, D. M. Alexander, A. Bault et al., *Broad Absorption Line Quasars in the Dark Energy Spectroscopic Instrument Early Data Release*, *arXiv e-prints* (2023) arXiv:2309.03434 [`2309.03434`].

[50] A. Font-Ribera, E. Arnau, J. Miralda-Escudé, E. Rollinde, J. Brinkmann, J. R. Brownstein et al., *The large-scale quasar-Lyman α forest cross-correlation from BOSS*, *JCAP* **2013** (2013) 018 [`1303.1937`].

[51] A. Font-Ribera and J. Miralda-Escudé, *The effect of high column density systems on the measurement of the Lyman-α forest correlation function*, *JCAP* **2012** (2012) 028 [`1205.2018`].

[52] A. Font-Ribera, J. Miralda-Escudé, E. Arnau, B. Carithers, K.-G. Lee, P. Noterdaeme et al., *The large-scale cross-correlation of Damped Lyman alpha systems with the Lyman alpha forest: first measurements from BOSS*, *JCAP* **2012** (2012) 059 [`1209.4596`].

[53] W. L. Freedman, B. F. Madore, B. K. Gibson, L. Ferrarese, D. D. Kelson, S. Sakai et al., *Final Results from the Hubble Space Telescope Key Project to Measure the Hubble Constant*, *ApJ* **553** (2001) 47 [`astro-ph/0012376`].

[54] L. Á. García, P. Martini, A. X. Gonzalez-Morales, A. Font-Ribera, H. K. Herrera-Alcantar, J. N. Aguilar et al., *Analysis of the impact of broad absorption lines on quasar redshift measurements with synthetic observations*, Mon. Not. Roy. Astron. Soc. **526** (2023) 4848 [`2304.05855`].

[55] C. M. Gaskell, *A redshift difference between high and low ionization emission-line regions in QSO's-evidence for radial motions.*, *ApJ* **263** (1982) 79.

[56] C. Gordon, A. Cuceu, J. Chaves-Montero, A. Font-Ribera, A. X. González-Morales, J. Aguilar et al., *3D correlations in the Lyman-α forest from early DESI data*, *JCAP* **2023** (2023) 045 [`2308.10950`].

[57] D. Green et al., *Using active learning to improve quasar identification for the desi spectra processing pipeline*, *in preperation* (2025) .

[58] Z. Guo and P. Martini, *Classification of Broad Absorption Line Quasars with a Convolutional Neural Network*, *ApJ* **879** (2019) 72 [`1901.04506`].

[59] J. Guy, S. Bailey, A. Kremin, S. Alam, D. M. Alexander, C. Allende Prieto et al., *The Spectroscopic Data Processing Pipeline for the Dark Energy Spectroscopic Instrument*, *AJ* **165** (2023) 144 [`2209.14482`].

[60] H. K. Herrera-Alcantar, A. Muñoz-Gutiérrez, T. Tan, A. X. González-Morales, A. Font-Ribera, J. Guy et al., *Synthetic spectra for Lyman-α forest analysis in the Dark Energy Spectroscopic Instrument*, *arXiv e-prints* (2023) arXiv:2401.00303 [`2401.00303`].

[61] P. C. Hewett and V. Wild, *Improved redshifts for SDSS quasar spectra*, Mon. Not. Roy. Astron. Soc. **405** (2010) 2302 [`1003.3017`].

[62] G. Hinshaw, D. Larson, E. Komatsu, D. N. Spergel, C. L. Bennett, J. Dunkley et al., *Nine-year Wilkinson Microwave Anisotropy Probe (WMAP) Observations: Cosmological Parameter Results*, *ApJS* **208** (2013) 19 [`1212.5226`].

[63] D. W. Hogg, *Distance measures in cosmology*, *arXiv e-prints* (1999) astro [`astro-ph/9905116`].

[64] J. Hou, A. G. Sánchez, A. J. Ross, A. Smith, R. Neveux, J. Bautista et al., *The completed SDSS-IV extended Baryon Oscillation Spectroscopic Survey: BAO and RSD measurements from anisotropic clustering analysis of the quasar sample in configuration space between redshift 0.8 and 2.2*, Mon. Not. Roy. Astron. Soc. **500** (2021) 1201 [`2007.08998`].

[65] E. Hubble, *A Relation between Distance and Radial Velocity among Extra-Galactic Nebulae*, *Proceedings of the National Academy of Science* **15** (1929) 168.

[66] D. Huterer, D. Kirkby, R. Bean, A. Connolly, K. Dawson, S. Dodelson et al., *Growth of cosmic structure: Probing dark energy beyond expansion*, *Astroparticle Physics* **63** (2015) 23 [`1309.5385`].

[67] A. Jenkins, C. S. Frenk, F. R. Pearce, P. A. Thomas, J. M. Colberg, S. D. M. White et al., *Evolution of Structure in Cold Dark Matter Universes*, *ApJ* **499** (1998) 20 [`astro-ph/9709010`].

[68] N. Kaiser, *Clustering in real space and in redshift space*, Mon. Not. Roy. Astron. Soc. **227** (1987) 1.

[69] V. Kamble, K. Dawson, H. du Mas des Bourboux, J. Bautista and D. P. Scheinder, *Measurements of Effective Optical Depth in the Lyα Forest from the BOSS DR12 Quasar Sample*, *ApJ* **892** (2020) 70 [`1904.01110`].

[70] N. G. Karaçaylı, P. Martini, J. Guy, C. Ravoux, M. L. Abdul Karim, E. Armengaud et al., *Optimal 1D Ly α forest power spectrum estimation - III. DESI early data*, Mon. Not. Roy. Astron. Soc. **528** (2024) 3941 [`2306.06316`].

[71] N. G. Karaçaylı, P. Martini, D. H. Weinberg, V. Iršič, J. Aguilar, S. Ahlen et al., *A framework to measure the properties of intergalactic metal systems with two-point flux statistics*, Mon. Not. Roy. Astron. Soc. **522** (2023) 5980 [`2302.06936`].

[72] T. S. Kim, J. S. Bolton, M. Viel, M. G. Haehnelt and R. F. Carswell, *An improved measurement of the flux distribution of the Lyα forest in QSO absorption spectra: the effect of continuum fitting, metal contamination and noise properties*, Mon. Not. Roy. Astron. Soc. **382** (2007) 1657 [`0711.1862`].

[73] D. Kirkby, "David Kirkby, private communication, 2020."

[74] D. Kirkby, D. Margala, A. Slosar, S. Bailey, N. G. Busca, T. Delubac et al., *Fitting methods for baryon acoustic oscillations in the Lyman-α forest fluctuations in BOSS data release 9*, *JCAP* **2013** (2013) 024 [`1301.3456`].

[75] F. Lepori, V. Iršič, E. Di Dio and M. Viel, *The impact of relativistic effects on the 3D Quasar-Lyman-α cross-correlation*, *JCAP* **2020** (2020) 006 [`1910.06305`].

[76] M. Levi, C. Bebek, T. Beers, R. Blum, R. Cahn, D. Eisenstein et al., *The DESI Experiment, a whitepaper for Snowmass 2013*, *arXiv e-prints* (2013) arXiv:1308.0847 [`1308.0847`].

[77] A. Lewis, A. Challinor and A. Lasenby, *Efficient Computation of Cosmic Microwave Background Anisotropies in Closed Friedmann-Robertson-Walker Models*, *ApJ* **538** (2000) 473 [`astro-ph/9911177`].

[78] LSST Science Collaboration, P. A. Abell, J. Allison, S. F. Anderson, J. R. Andrew, J. R. P. Angel et al., *LSST Science Book, Version 2.0*, *arXiv e-prints* (2009) arXiv:0912.0201 [`0912.0201`].

[79] P. McDonald, U. Seljak, S. Burles, D. J. Schlegel, D. H. Weinberg, R. Cen et al., *The Lyα Forest Power Spectrum from the Sloan Digital Sky Survey*, *ApJS* **163** (2006) 80 [`astro-ph/0405013`].

[80] A. D. Myers, J. Moustakas, S. Bailey, B. A. Weaver, A. P. Cooper, J. E. Forero-Romero et al., *The Target-selection Pipeline for the Dark Energy Spectroscopic Instrument*, *AJ* **165** (2023) 50 [`2208.08518`].

[81] R. Neveux, E. Burtin, A. de Mattia, A. Smith, A. J. Ross, J. Hou et al., *The completed SDSS-IV extended Baryon Oscillation Spectroscopic Survey: BAO and RSD measurements from the anisotropic power spectrum of the quasar sample between redshift 0.8 and 2.2*, Mon. Not. Roy. Astron. Soc. **499** (2020) 210 [`2007.08999`].

[82] W. J. Percival and M. White, *Testing cosmological structure formation using redshift-space distortions*, Mon. Not. Roy. Astron. Soc. **393** (2009) 297 [`0808.0003`].

[83] S. Perlmutter, G. Aldering, G. Goldhaber, R. A. Knop, P. Nugent, P. G. Castro et al., *Measurements of Ω and Λ from 42 High-Redshift Supernovae*, *ApJ* **517** (1999) 565 [`astro-ph/9812133`].

[84] D. W. Pesce, J. A. Braatz, M. J. Reid, A. G. Riess, D. Scolnic, J. J. Condon et al., *The Megamaser Cosmology Project. XIII. Combined Hubble Constant Constraints*, Astrophys. J. Let. **891** (2020) L1 [`2001.09213`].

[85] Planck Collaboration, N. Aghanim, Y. Akrami, M. Ashdown, J. Aumont, C. Baccigalupi et al., *Planck 2018 results. VI. Cosmological parameters*, Astron. Astrophys. **641** (2020) A6 [`1807.06209`].

[86] C. Ramírez-Pérez, I. Pérez-Ràfols, A. Font-Ribera, M. A. Karim, E. Armengaud, J. Bautista et al., *The Lyman-α forest catalog from the Dark Energy Spectroscopic Instrument Early Data Release*, Mon. Not. Roy. Astron. Soc. (2023) [`2306.06312`].

[87] C. Ravoux, M. L. Abdul Karim, E. Armengaud, M. Walther, N. G. Karaçaylı, P. Martini et al., *The Dark Energy Spectroscopic Instrument: one-dimensional power spectrum from first Ly α forest samples with Fast Fourier Transform*, Mon. Not. Roy. Astron. Soc. **526** (2023) 5118 [`2306.06311`].

[88] G. T. Richards, D. E. Vanden Berk, T. A. Reichard, P. B. Hall, D. P. Schneider, M. SubbaRao et al., *Broad Emission-Line Shifts in Quasars: An Orientation Measure for Radio-Quiet Quasars?*, *AJ* **124** (2002) 1 [`astro-ph/0204162`].

[89] A. G. Riess, S. Casertano, W. Yuan, L. Macri, J. Anderson, J. W. MacKenty et al., *New Parallaxes of Galactic Cepheids from Spatially Scanning the Hubble Space Telescope: Implications for the Hubble Constant*, *ApJ* **855** (2018) 136 [`1801.01120`].

[90] A. G. Riess, A. V. Filippenko, P. Challis, A. Clocchiatti, A. Diercks, P. M. Garnavich et al., *Observational Evidence from Supernovae for an Accelerating Universe and a Cosmological Constant*, *AJ* **116** (1998) 1009 [`astro-ph/9805201`].

[91] A. G. Riess, L. M. Macri, S. L. Hoffmann, D. Scolnic, S. Casertano, A. V. Filippenko et al., *A 2.4% Determination of the Local Value of the Hubble Constant*, *ApJ* **826** (2016) 56 [`1604.01424`].

[92] A. G. Riess, W. Yuan, L. M. Macri, D. Scolnic, D. Brout, S. Casertano et al., *A Comprehensive Measurement of the Local Value of the Hubble Constant with 1 km* s^{-1} *Mpc*$^{-1}$ *Uncertainty from the Hubble Space Telescope and the SH0ES Team*, Astrophys. J. Let. **934** (2022) L7 [`2112.04510`].

[93] K. K. Rogers, S. Bird, H. V. Peiris, A. Pontzen, A. Font-Ribera and B. Leistedt, *Correlations in the three-dimensional Lyman-alpha forest contaminated by high column density absorbers*, Mon. Not. Roy. Astron. Soc. **476** (2018) 3716 [`1711.06275`].

[94] G. C. Rudie, C. C. Steidel, A. E. Shapley and M. Pettini, *The Column Density Distribution and Continuum Opacity of the Intergalactic and Circumgalactic Medium at Redshift langzrang = 2.4*, *ApJ* **769** (2013) 146 [`1304.6719`].

[95] A. Sandage and G. A. Tammann, *Steps toward the Hubble constant. VIII - The global value*, *ApJ* **256** (1982) 339.

[96] E. F. Schlafly, D. Kirkby, D. J. Schlegel, A. D. Myers, A. Raichoor, K. Dawson et al., *Survey Operations for the Dark Energy Spectroscopic Instrument*, *AJ* **166** (2023) 259 [`2306.06309`].

[97] D. J. Schlegel, J. A. Kollmeier, G. Aldering, S. Bailey, C. Baltay, C. Bebek et al., *The MegaMapper: A Stage-5 Spectroscopic Instrument Concept for the Study of Inflation and Dark Energy*, *arXiv e-prints* (2022) arXiv:2209.04322 [`2209.04322`].

[98] H.-J. Seo and D. J. Eisenstein, *Probing Dark Energy with Baryonic Acoustic Oscillations from Future Large Galaxy Redshift Surveys*, *ApJ* **598** (2003) 720 [`astro-ph/0307460`].

[99] Y. Shen, W. N. Brandt, G. T. Richards, K. D. Denney, J. E. Greene, C. J. Grier et al., *The Sloan Digital Sky Survey Reverberation Mapping Project: Velocity Shifts of Quasar Emission Lines*, *ApJ* **831** (2016) 7 [`1602.03894`].

[100] J. H. Silber, D. J. Schlegel, R. Araujo, C. Baltay, R. W. Besuner, E. Farr et al., *25,000 optical fiber positioning robots for next-generation cosmology*, *arXiv e-prints* (2022) arXiv:2212.07908 [`2212.07908`].

[101] J. H. Silber, P. Fagrelius, K. Fanning, M. Schubnell, J. N. Aguilar, S. Ahlen et al., *The Robotic Multiobject Focal Plane System of the Dark Energy Spectroscopic Instrument (DESI)*, *AJ* **165** (2023) 9 [`2205.09014`].

[102] A. Slosar, A. Font-Ribera, M. M. Pieri, J. Rich, J.-M. Le Goff, É. Aubourg et al., *The Lyman-α forest in three dimensions: measurements of large scale flux correlations from BOSS 1st-year data*, *JCAP* **2011** (2011) 001 [`1104.5244`].

[103] A. Slosar, V. Iršič, D. Kirkby, S. Bailey, N. G. Busca, T. Delubac et al., *Measurement of baryon acoustic oscillations in the Lyman-α forest fluctuations in BOSS data release 9*, *JCAP* **2013** (2013) 026 [`1301.3459`].

[104] S. A. Smee, J. E. Gunn, A. Uomoto, N. Roe, D. Schlegel, C. M. Rockosi et al., *The Multi-object, Fiber-fed Spectrographs for the Sloan Digital Sky Survey and the Baryon Oscillation Spectroscopic Survey*, *AJ* **146** (2013) 32 [`1208.2233`].

[105] Spec-S5 Collaboration, "Spec-S5 Reference Design and Site Seletion." `https://drive.google.com/file/d/1r0pIYXCuc1zN-NJlhESFtYCTDfsdn7CC/view?pli=1`, February, 2024.

[106] D. H. Weinberg, M. J. Mortonson, D. J. Eisenstein, C. Hirata, A. G. Riess and E. Rozo, *Observational probes of cosmic acceleration*, Phys. Rept. **530** (2013) 87 [`1201.2434`].

[107] D. G. York, J. Adelman, J. Anderson, John E., S. F. Anderson, J. Annis, N. A. Bahcall et al., *The Sloan Digital Sky Survey: Technical Summary*, *AJ* **120** (2000) 1579 [`astro-ph/0006396`].

[108] S. Youles, J. E. Bautista, A. Font-Ribera, D. Bacon, J. Rich, D. Brooks et al., *The effect of quasar redshift errors on Lyman-α forest correlation functions*, Mon. Not. Roy. Astron. Soc. **516** (2022) 421 [`2205.06648`].

[109] J. Zou et al., *The DESI Damped Lyα System Survey: Data Release 1*, *in preparation* (2025) .